

**A Basic Study of Electrical Impedance Spectroscopy for Intravascular  
Diagnosis and Therapy Monitoring of Atherosclerosis**

Dissertation  
zur Erlangung des Grades  
des Doktors der Ingenieurwissenschaften  
der Naturwissenschaftlich-Technischen Fakultät II  
- Physik und Mechatronik -  
der Universität des Saarlandes

von

M. Eng. Sungbo Cho

Saarbrücken

2008

Tag des Kolloquiums:	22.09.2008
Dekanin/Dekan:	Prof. Dr. A. Schütze
Mitglieder des Prüfungsausschusses:	Prof. Dr. G. Fuhr Prof. Dr. H. Seidel Prof. Dr. H. Janocha Dr. I. Knittel

## **Kurze Zusammenfassung**

Das Ziel dieser Arbeit war die Konzeption, Entwicklung und Evaluierung einer Methode auf Basis der elektrischen Impedanz für die Diagnose und das Therapiemonitoring von Artherosklerose. Um grundsätzlich zu verstehen, wie die Änderung der Gewebeparameter auf Zellebene mit Hilfe der elektrischen Impedanzspektroskopie charakterisiert werden kann – erfolgten theoretische und experimentelle Untersuchungen auf Basis eines Einzelzell/Mikroloch-Modells. Die Ergebnisse zeigten, dass Änderungen der Gewebeparameter auf Zellebene (wie z. B. Zellform und Membranintegrität) die messbaren elektrischen Eigenschaften der Gewebe beeinflussten und dass die Impedanzspektroskopie zur Charakterisierung von entsprechenden Atherosklerose-bedingten Änderungen von Zellparameter verwendet werden kann. *in vitro* Experimente, die auf der adipogenen Stammzelldifferenzierung und der Virusinfektion basierten, zeigten, dass sich Änderungen in Zellverbänden, die in Zusammenhang mit der Arteriosklerose stehen (Auflösen von Zellen, Anreicherung von Fettzellen) in Impedanzdaten widerspiegeln. Ein Ballonimpedanzkatheter mit integrierten flexiblen Mikroelektroden wurde entwickelt und in *in vitro*- und *in situ*-Experimenten verwendet. Theoretische Untersuchungen basierten ebenfalls auf dem Ballonkatheter-Ansatz. Erstmals wurde erfolgreich demonstriert, dass sich unter *in situ* Bedingungen Aortenbereiche mit fetthaltigen Plaques von den normalen Bereichen unterscheiden lassen.

## Abstract

The goal of this thesis is the conception, development and evaluation of an electrical impedance-based method for the diagnosis and therapy monitoring of atherosclerosis. To understand basically how the change of tissue parameters on the cellular level can be characterized electrically by impedance spectroscopy, theoretical and experimental investigations based on a single cell/micro hole model were performed. The results indicate that changes in the tissue parameters on the cellular level like cellular shape and membrane integrity affect the electrical characteristics of tissues, and that impedance spectroscopy can be used to characterize electrically the effects of atherosclerosis related to these parameters. *In vitro* experiments based on adipogenic stem cell differentiation and virus infection showed that the cellular alterations in cell assemblies on atherosclerotic pathology (e.g. disruption of cell layer by virus infection, accumulation of fat cells) are well reflected in the measured impedance data. A balloon impedance catheter with integrated flexible microelectrodes was developed and used for experimental investigation *in vitro* and *in situ* and considered for theoretical investigations respectively. For the first time, it was successfully demonstrated that the aortas containing fatty plaques can be distinguished from normal aortas by intravascular impedance measurement with the developed balloon impedance catheter system.

**Parts of this Thesis are published in the following articles of scientific journals**

- I. **Cho, S.**, Castellarnau, M., Samitier, J., Thielecke, H.: "Dependence of impedance of embedded single cells on cellular behaviour". *Sensors* **8**, 1198-1211 (2008).
- II. **Cho, S.**, Thielecke, H.: "Micro hole based cell chip with impedance spectroscopy". *Biosensors and Bioelectronics* **22**, 1764-1768 (2007).
- III. **Cho, S.**, Becker, S., Briesen, H., Thielecke, H.: "Impedance monitoring of herpes simplex virus-induced cytopathic effect in Vero cells". *Sensors and Actuators B: Chemical* **123**, 978-982 (2007).
- IV. **Cho, S.**, Thielecke, H.: "Influence of the electrode position on the characterisation of artery stenotic plaques by using impedance catheter". *IEEE Trans. Biomed. Eng.* **53**, 2401-2404 (2006).
- V. **Cho, S.**, Thielecke, H.: "Design of electrode array for impedance measurement of lesions in arteries". *Physiological Measurement* **26**, S19-S26 (2005).
- VI. Süselbeck, T., Thielecke, H., Koechlin, J., **Cho, S.**, Weinschenk, I., Metz, J., Borggrefe, M., Hasse, K. K.: "Intravascular electric impedance spectroscopy of atherosclerotic lesions using a new impedance catheter system". *Basic Research in Cardiology* **100**(5), 446-452 (2005).

## Acknowledgements

I would like to thank Prof. Dr. Günter R. Fuhr, the director of Fraunhofer Institute for Biomedical Engineering (Fraunhofer IBMT), for affording me the opportunity to work at Biohybrid Systems, Fraunhofer IBMT. I remember his kind encouragement even late at night.

Prof. Helmut Seidel, Chair of Micromechanics, Microfluidics / Microactuators, University of Saarland, I appreciate for agreeing to review my thesis and his meaningful discussion and advice on the thesis.

Dr. Hagen Thielecke, head of Department of Biohybrid Systems in Fraunhofer IBMT, I would like to thank for his help to study here. He has supported and encouraged me as a mentor and friend. I also would like to thank PD Dr. Hagen von Briesen, head of Department of Cell Biology & Applied Virology in Fraunhofer IBMT for his thoughtful support about Virology. With his help, I was able to develop the impedance diagnosis of virus infection using electrode-based chip.

I wish to thank PD Dr. Tim Süsselbeck and Dr. Innes Streitner, Department of Medicine, University Hospital of Mannheim, for the cooperation on the research of cardiology. Due to their support, I was able to valuate the impedance catheter to diagnose atherosclerosis. Thanks to Dr. Paul Genever, Biomedical Tissue Research Group, University of York, for providing the protocols for adipogenic differentiation of stem cells. I wish to appreciate to Dipl.-Ing. (FH) Thomas Dörge, Neuroprosthetics Group in Fraunhofer IBMT, for his dedicated effort to fabricate the MEMS devices.

To all members in the Departments of Biohybrid Systems and Cell Biology & Applied Virology of Fraunhofer IBMT, I am appreciative of their careful concern and help. They gave me lots of and wordless help to learn and enjoy the culture and life in our institute and city St. Ingbert as well.

To my parents, Haeyeon Cho and Hyesuk Mun, to my parents-in-law, Youngman Lim and Kyunghee Park, and to my brother Sungmoon Cho, I am grateful for their thoughtful encouragement. To my wife Areum Lim, I am deeply grateful for her support and patient. And to my first daughter Han Hee.

## Table of Contents

<b>1</b>	<b>Introduction</b>	<b>1</b>
1.1	Atherosclerosis	3
1.2	Electrical Properties of Cells and Tissues	6
1.3	Impedance Spectroscopy (IS)	9
1.4	Micro Electro Mechanical System (MEMS) Technology	12
1.5	Finite Element Method Simulation	14
1.6	Biomedical Applications of MEMS with IS	17
<b>2</b>	<b>Objectives of Study and Appropriate Solutions</b>	<b>21</b>
<b>3</b>	<b>Electrical Characterization of Single Cells</b>	<b>23</b>
3.1	Methodology	23
3.1.1	Single Cell Model for Theoretical and Experimental Investigations	23
3.1.2	Simulation of Electrical Characteristics of a Single Cell/Micro Hole Model	24
3.1.3	Fabrication of Micro Hole Structure for Experimental Investigations	26
3.1.4	Experimental Investigation by Using the Single Cell/Micro Hole Model	27
3.2	Results	30
3.2.1	Simulated Electrical Characteristics of Micro Hole/Cell Model	30
3.2.2	Measured Impedance of Micro Hole/Cell Model	33
3.3	Discussion	36
3.3.1	Simulated Electrical Characteristics of the Cell/Micro Hole Model	36
3.3.2	Experimental Setup and Experimental Results	37
3.4	Conclusions	39
<b>4</b>	<b>Monitoring of Cellular Alteration in Cell Assemblies</b>	<b>40</b>
4.1	Methodology	40
4.1.1	Electrode-based Chip and Monitoring System	40
4.1.2	Electrical Properties of Cell Layer on Electrodes	44
4.1.3	Monitoring of Disintegration of Cell Layers Caused by an Infection Model with Herpes Simplex Viruses	45
4.1.4	Characterization of the Accumulation of Fat Cells in Cell Assemblies Using an Adipogenic Stem Cell Differentiation Model	46
4.2	Results	48

4.2.1	Simulated Electrical Characteristics of Cells on Electrodes	48
4.2.2	Measured Impedance of Cell layer during HSV Infection	51
4.2.3	Measured Impedance of Differentiated hMSCs	55
4.3	Discussion	61
4.3.1	Monitoring of Disruption of Cell Layers	61
4.3.2	Characterization of Accumulation of Fat Cells	62
4.4	Conclusions	64
<b>5</b>	<b>Intravascular Impedance Measurement of Vessels</b>	<b>65</b>
5.1	Methodology	65
5.1.1	Concept for Intravascular Impedance Measurement with BIC	65
5.1.2	Fabrication and Characterisation of Microelectrodes	66
5.1.3	Investigation of Effect of Vessel Thickness on Intravascular Impedance Measurement	69
5.1.4	Investigation of Effect of Relative Plaque Position to Electrodes on Intravascular Impedance Measurement	72
5.1.5	Experiment of Atherosclerotic Animal <i>in situ</i>	75
5.2	Results	78
5.2.1	Electrical Characteristics of Electrode Array	78
5.2.2	Dependence of Intravascular Impedance Measurement on Thickness of Vessel	81
5.2.3	Dependence of Intravascular Impedance Measurement on Relative Position of Plaque to Electrodes	84
5.2.4	Measured Impedance <i>in situ</i> and Analysis	89
5.3	Discussion	94
5.3.1	Impedance Characteristics of Microfabricated Electrodes	94
5.3.2	Influence of Vessel Thickness on Intravascular Impedance Measurement	95
5.3.3	Influence of Relative Plaque Position to Electrodes on Intravascular Impedance Measurement	95
5.3.4	Intravascular Electrical Characterization of Atherosclerotic Plaque in Vessel Walls	97
5.4	Conclusions	98
<b>6</b>	<b>General Discussion</b>	<b>99</b>
<b>7</b>	<b>Summary</b>	<b>101</b>

<b>8</b>	<b>Zusammenfassung</b>	<b>103</b>
<b>9</b>	<b>Publications related with Thesis</b>	<b>105</b>
<b>10</b>	<b>References</b>	<b>107</b>
	<b>Appendix: Programming Codes for FEM Simulation</b>	<b>115</b>
	A. Single Cell on Micro Hole Model in 3.1.2	115
	B. Cells on Electrode Model in 4.1.2	118
	C. Two-Layer Model in 5.1.3	120
	D. Atheromatous Vessel with BIC Model in 5.1.4	123

## Figure Captions

- Fig. 1.1: Changes in endothelial dysfunction during progression of atherosclerosis (Stary *et al.* 1995). 3
- Fig. 1.2: Photomicrograph of atheroma in coronary artery. A: adventitia, M: media, core: extracellular lipid with cholesterol crystals, fc: macrophage foam cells, arrow: macrophages that are not foam cells, pgc: proteoglycan layer, e: endothelium, magnification about x220 (Stary *et al.* 1995). 4
- Fig. 1.3: Schematic of bi-layer lipid membrane with embedded proteins and sodium channels (Grimnes and Martinsen 2000). 6
- Fig. 1.4: Membrane conductance during cell excitation (Hodgkin and Huxley 1952),  $G_{Na^+}$ ,  $G_{K^+}$ : specific membrane conductance caused by  $Na^+$  and  $K^+$  ions, respectively. 7
- Fig. 1.5: A voltage response when the alternating current is applied in a dielectric material. 9
- Fig. 1.6: Configuration and measured impedance with two- (a) and four-electrode method (b),  $I_{source}$ : alternating current source,  $I_m$ : current measured by amperemeter (A),  $V_m$ : measured voltage by voltagemeter (V),  $Z_{en}$ : nth electrode impedance,  $Z_{Vmeter}$ : impedance of voltagemeter,  $Z_m$ : measured impedance,  $Z_x$ : impedance of object. 10
- Fig. 1.7: Classification of the most common deposition processes, CVD: Chemical vapour deposition, MOCVD: Metal organic CVD, PECVD: Plasma enhanced CVD, MBE: Molecular beam epitaxy, RF: Radio frequency, dc: Direct current (Elshabini and Barlow 1998). 12
- Fig. 1.8: Schematic of simulation process with FEM for solving the physical problems (Carlos 2004). 14
- Fig. 1.9: Two-dimensional domain discretized into a number of triangular shaped elements,  $\phi_1$ ,  $\phi_2$ , and  $\phi_3$  are unknown nodal values. 15
- Fig. 1.10: Schematic of micro fluidic channel with a sample cell passing between the pairs of electrode (AC and BC) (upper), impedance difference monitored as the cell passes through the channel (below),  $C_{dl}$ : double layer capacitance on the electrode surface,  $G_m$  and  $C_m$ : conductance and capacitance of membrane,  $R_{sol1}$  and  $R_{sol2}$ : solution resistance,  $R_c$ : resistance of cytoplasm (Cheung *et al.* 2005). 17
- Fig. 1.11: Schematic of microelectrode-based cell chip, below: impedance recorded at the frequency of 4 kHz during the cell growth on the electrode (Giaever and Keese 1993). 18
- Fig. 1.12: Schematic of needle shaped microelectrode array implanted in the tissue, C1, C2: current applying electrodes, V1, V2: voltage measurement electrodes, below: impedance monitored during the ischemia and reperfusion (Ivorra *et al.* 2003). 19

- Fig. 3.1: Used single cell model to investigate the influence of cellular parameter on the measured tissue impedance, Upper panel: Schematic of tissue/electrode interface, Lower panel: Single cell model to investigate basically the influence of cellular alteration on the electrical characteristics of tissues on electrodes. 24
- Fig. 3.2: Schematic model of micro hole-based cell chip for FEM simulation. 25
- Fig. 3.3: Schematic of procedure for the fabrication of micro hole-based structure by using semiconductor process technology. 27
- Fig. 3.4: Experimental setup for investigation of the cell/micro hole model (a), micro hole-based chip with 44 wells and chip adapter mounted with microscope and four-electrode arrangement (b), and enlarged photo of one well with a micro hole (radius of 3  $\mu\text{m}$ ) at the center of membrane, scale bar: 30  $\mu\text{m}$ . 28
- Fig. 3.5: Schematic of impedance measurement on the cell/micro hole model. 29
- Fig. 3.6: Simulated log-scaled current densities near the single cell on one hole (equatorial radius of cell: 5  $\mu\text{m}$ , cell/substrate gap: 150 nm) at 1 kHz (a) and 1 MHz (b) by FEM. 31
- Fig. 3.7: Simulated impedance magnitude with different cell/substrate gap (equatorial radius of cell: 5  $\mu\text{m}$ ) (a) and equatorial radius of cell (cell/substrate gap: 150 nm) (b) vs. log-scaled frequency by FEM. 32
- Fig. 3.8: Micrograph after positioning a L929 single cell on the hole (a) and after the cell cultivation for 1 day (b), measured impedance magnitude of the cell culture medium (No Cell), after positioning a single L929 cell on a hole (0), and after the cell cultivation for two (2 days) or four days (4 days) vs. the log-scaled frequency from 1 Hz to 1 MHz (c), potential level: 10 mV, averages and standard errors of each group were indicated as symbols and plus bars, respectively (n for each group = 3). 34
- Fig. 3.9: Influence of 5 nl of culture medium including 5% DMSO on L929 cells, impedance monitoring of culture medium (No Cell) and after the cultivation of L929 cell for two days (2 days), impedance magnitude (a) and phase (b) were measured at 1 kHz, DMSO was applied at 200 s. 35
- Fig. 4.1: Schematic of procedure for the fabrication of planar electrode-based structure by using semiconductor process technology. 41
- Fig. 4.2: Schematic of electric connection between the electrode substrate with 4 by 4 electrode array (center) and the ceramic chip carrier chip, numbers in painted circles indicate the connected electrode and pin. 42
- Fig. 4.3: Fabricated 4 by 4 planar electrode array with ceramic chip carrier (a) and the electrode-based chip integrated with a glass dish for the cell cultivation (b). 43
- Fig. 4.4: Impedance analyzer with multiplexer for computer controlled impedance measurement of cell layer during the cultivation in an incubator (a), cell chips combined with chip adapter in the incubator (b), simplified schematic of the impedance monitoring system with electrode-based cell chip (c). 43
- Fig. 4.5: Schematic model of cell monolayer on electrode for FEM simulation (not scaled),  $\sigma$ ,  $\epsilon_r$ : conductivity and dielectric constant, respectively. 44

- Fig. 4.6: Schematic model of cell monolayer on electrode designed by Giaever and Keese (1991), cells are cylindrical shape with equal radius ( $r_c$ ) and with equal cell/substrate gap ( $h$ ),  $R_b$  and  $\alpha$ : parameters involved with cell/cell and cell/substrate gap, respectively. 45
- Fig. 4.7: An equivalent circuit for cell on electrodes,  $R_{cl}$  and  $C_{cl}$  are the resistance and the capacitance of cell layer (Wegener *et al.* 1996), respectively,  $CPE_{el}$ : the constant phase element for electrode impedance (Boer and Osterom 1978),  $R_s$ : the resistance of medium. 47
- Fig. 4.8: Simulated potential distribution near a cylindrically shaped cell on electrode in the model of Fig. 4.5 with cell/substrate gap ( $h$ ) of 500 nm and cell/cell gap ( $g$ ) of 2  $\mu\text{m}$  at 1 kHz (a) or 1 MHz (b). 49
- Fig. 4.9: Nyquist plot of simulated impedance (FEM) of cell mono layer on an electrode with radius of 500  $\mu\text{m}$  in the model of Fig. 4.5 with respect to different cell/substrate gap ( $h$ ) (a) or cell/cell gap ( $g$ ) (b). 50
- Fig. 4.10: Vero cells adhered onto the culture dish (a) and the detachment of cells infected with HSV (b), scale bar: 200  $\mu\text{m}$ . 51
- Fig. 4.11: Vero cells not infected (a) and infected with HSV for 102 h at the MOI of 0.0006 (b), 0.006 (c), or 0.06 (d) on the platinum electrode with a radius of 500  $\mu\text{m}$ , arrows indicate the partially exposed electrode area caused by the detachment of infected cells, scale bar: 100  $\mu\text{m}$ . 52
- Fig. 4.12: Measured and fitted impedance spectra without cells (No Cell) and with Vero cells cultured for 68 h, in 'Vero cultured for 68 h', the fitted parameters  $R_b$  and  $\alpha$  of (eq. 4.1) were 13.55  $\Omega\text{ cm}^2$  and 7.24  $\Omega^{0.5}\text{cm}$ , respectively. 53
- Fig. 4.13: Monitoring of  $R_b$  (a) and  $\alpha$  (b) of Vero cells during the cultivation or infection with HSV at the MOI of 0.0006, 0.006, or 0.06. 54
- Fig. 4.14: Micrograph of human mesenchymal stem cells adhered on the fabricated circular electrode-based chip during the cultivation, scale bar: 60  $\mu\text{m}$ . 55
- Fig. 4.15: Average and standard deviation of measured impedance magnitude (measure) over the frequency for electrodes without or with hMSCs cultured for 460 h ( $n$  for each group = 3) and fitted graph (fit): for fitting, the equivalent circuit of Fig. 4.7 was used (a), monitoring of model parameter  $R_{cl}$  during the growth of hMSCs on planar electrodes (b). 56
- Fig. 4.16: Micrograph of hMSCs at day 13 of adipogenic differentiation showing lipid vacuoles, triglyceride in the fat storages was coloured redly through oil red O staining, scale bar: 50  $\mu\text{m}$ . 57
- Fig. 4.17: Averages and standard errors of  $R_{cl}$  and  $C_{cl}$  ( $n$  for each group = 6) of hMSCs cultivated in the control medium for 39 days or in the differentiation medium for 29 days and for 39 days (a), micrographs of hMSCs on the electrode at day 39 of cultivation with (b) and without the adipogenic differentiation factor (c), respectively (scale bar: 100  $\mu\text{m}$ ). 58
- Fig. 4.18: Micrographs of hMSCs on a platinum electrode at day 9 of adipogenic differentiation cultivated without (a) and with 10  $\mu\text{M}$  chlorpyrifos (b) (scale bar: 200  $\mu\text{m}$ ), monitoring of normalized  $R_{cl}$  of hMSCs during the adipogenic differentiation without and with 10  $\mu\text{M}$  chlorpyrifos (c). 59

- Fig. 4.19: Micrographs of hMSCs partially differentiated to adipocytes (at day 30 of differentiation) before (a) and after applying 10  $\mu\text{M}$  chlorpyrifos (at day 35 of differentiation or at day 5 after adding chlorpyrifos) (b) (scale bar: 200  $\mu\text{m}$ ), influence of 10  $\mu\text{M}$  chlorpyrifos on the average and standard error of normalized  $R_{cl}$  ( $n = 6$ ) of hMSCs differentiated to adipocytes (c). 60
- Fig. 5.1: Schematic of balloon impedance catheter (BIC) with microelectrode structure for intravascular IS of atheromatous vessel walls. 66
- Fig. 5.2: Fabricated flexible polyimide-based electrode array with four electrodes, exposed area of rectangular electrode: 100  $\mu\text{m}$  x 100  $\mu\text{m}$ , separation distance between electrode centers: 333  $\mu\text{m}$  (scale bar: 1 mm). 67
- Fig. 5.3: An equivalent circuit of electrolyte impedance measured by using electrodes in,  $\text{CPE}_e$ : constant phase element for interfacial electrode impedance,  $R_s$ : electrolyte resistance,  $C_s$ : stray capacitance. 68
- Fig. 5.4: Schematic of a quasi-vessel model with electrode array of Wenner alpha type (area and separation of rectangular electrodes: 100  $\mu\text{m}$  x 100  $\mu\text{m}$  and 333  $\mu\text{m}$ ), C1, C2 and V1, V2: electrode pairs on intravascular wall for current injecting and voltage measurement, respectively. 69
- Fig. 5.5: Schematic of a two-layer model with electrode array of Wenner alpha type (area and separation of rectangular electrodes: 100  $\mu\text{m}$  x 100  $\mu\text{m}$  and 333  $\mu\text{m}$ ), C1, C2 and V1, V2: electrode pairs on the bottom of layer 1 for current injecting and voltage measurement, respectively (a), experimental set-up for two-layer model with electrode array, layer 1: 0.9% NaCl electrolyte, layer 2: an insulated glass plate with air (b). 71
- Fig. 5.6: Quasi-atheromatous vessel model with BIC for 3D FEM simulation on the cross (a) and longitudinal section (b) at the middle of electrode array, O: middle axis of catheter,  $\theta_e$ : separation angle between the electrode array and x axis,  $r_1$ : depth of lipid from the endothelium,  $z_1$ : longitudinal separation between the middles of electrode array and lipid. 73
- Fig. 5.7: Schematic of a set of five electrode arrangements positioned concentrically on the balloon catheter and separated each other with equal distance (arc length), the middle electrode arrangement (active) is located under the middle of lipid in the model of Fig. 5.6 ( $\theta_e = 0$ ,  $r_1 = 0.4$  mm,  $z_1 = 0$ ). 75
- Fig. 5.8: Expanded balloon of BIC (upper) and schematic of intravascular impedance measurement of vessel walls with BIC,  $I$ : current with the amplitude of  $I_o$  and phase of  $\phi_I$ ,  $V$ : potential with the amplitude of  $V_o$  and phase of  $\phi_V$ . 77
- Fig. 5.9: Impedance spectra of 0.9% NaCl electrolyte at 25°C measured by two-electrode and four-electrode method with fabricated electrode array, log-scaled impedance magnitude (a) and phase (b) vs. log-scaled frequency, spectrum measured by two-electrode method was fitted by the equivalent circuit in Fig. 5.3. 79
- Fig. 5.10: Impedance magnitude over the frequency (a) and resistance (b) measured at different concentration of NaCl in the electrolyte (at 25°C) by four-electrode method with fabricated electrode array. 80

- Fig. 5.11: Log of simulated sensitivities (at 10 kHz) at the middle of the electrode array on the transverse plane in the quasi-vessel model with vessel thickness of 333  $\mu\text{m}$  and with inner vessel radius of 0.5 (a), 1 (b), 1.5 (c), or 2 mm (d). 81
- Fig. 5.12: Ratio of impedance magnitude at 10 kHz simulated at different thickness of vessel to one when the thickness of vessel is 1 cm ( $|Z|_{\text{app}}/|Z|_{\text{inf}}$ ) in the quasi-vessel model with the inner vessel radius of 0.5, 1, 1.5, or 2 mm vs. the ratio of vessel thickness to the separation distance between the outer electrodes for applying current of 1 mm. 82
- Fig. 5.13: Log of sensitivities simulated at 10 kHz in the two-layer model with the level of 333  $\mu\text{m}$  (a and b) and semi-infinite (c and d) along the longitudinal (a and c) and transverse axis (b and d) at the middle of the electrode array. C1, C2 and V1, V2: electrode pairs for current applying and voltage measurement, respectively. 83
- Fig. 5.14: Ratio of impedance magnitude at 10 kHz at different level of electrolyte to one when the level of electrolyte is 1 cm ( $|Z|_{\text{app}}/|Z|_{\text{inf}}$ ) in the two-layer model with respect to the ratio of the electrolyte level to the separation distance between the outer electrodes for applying current of 1 mm. 84
- Fig. 5.15: Simulated impedance magnitude at 1 kHz or 10 kHz with atheromatous vessel model with respect to the separation angle between the electrode array and the lipid,  $\theta_e$  (a), the depth of lipid from the endothelium,  $r_1$  (b), and the longitudinal separation between the lipid with length of 2.4 mm and the electrode array,  $z_1$  (c). 86
- Fig. 5.16: Log-scaled magnitude of current density at 10kHz along the cross section of artery at the middle of electrode array with respect to the separation angle between the electrode array and the lipid,  $\theta_e$  (a = 0°, b = 20°, c = 45°, and d = 90°) in the atheromatous vessel model. 87
- Fig. 5.17: Log-scaled magnitude of current density at 10 kHz along the longitudinal section of artery at the middle of electrode array with respect to the longitudinal separation between the lipid and the electrode array,  $z_1$  (a = 0 mm, b = 0.8 mm, c = 1.6 mm, and d = 2.4 mm) in the atheromatous vessel model. 88
- Fig. 5.18: Simulated impedance magnitude at 10 kHz for the setup in Fig. 5.7 in dependency of the distance (arc length) between the neighbored electrode arrangements. 89
- Fig. 5.19: Example of aortic angiogram (a) and intravascular ultrasound cross section image (b) of a rabbit, micrograph of an aortic segment with plaque indicated by arrow, scale bar: 2 mm (c) and an enlarged micrograph of marked vessel (left-bottom arrow) with plaque (right-top arrow), scale bar: 500  $\mu\text{m}$  (d). 90
- Fig. 5.20: Impedance magnitude of all aortic segments of 5 rabbits (Aorta 1 to Aorta 5) after 17 weeks of high cholesterol diet measured intravascularly at 1 kHz (■) and 10 kHz (○) recorded by using the developed balloon impedance catheter. 92

- Fig. 5.21: Averages and standard deviations of measured impedance magnitudes in Fig. 5.20, classified by the thickness of plaque, P0: no plaque (n = 44), P1: plaque thinner than media (n = 12), P2: plaque thicker than media (n = 36). 93
- Fig. 5.22: Averages and standard errors of ICF (impedance magnitude at 1 kHz – impedance magnitude at 10 kHz) calculated from the data of Fig. 5.20 and result of hypothesis t-test, P0: no plaque (n = 44), P1: plaque thinner than media (n = 12), P2: plaque thicker than media (n = 36). 93
- Fig. 5.23: Schematic of balloon catheter with multi-electrode arrays for controlling the distribution of electric fields intravascularly. 96

### Table Captions

- Tab. 1.1: Electrical properties of  $\text{SiO}_2$ ,  $\text{Si}_3\text{N}_4$ , and polyimide at room temperature (Srivastava *et al.* 1985, Elshabini and Barlow 1998, Awan and Gould 2003, Deligöz *et al.* 2006). 13
- Tab. 3.1: Conductivity and relative permittivity of materials used for FEM simulation with model of a single cell on a micro hole of Fig. 3.2 (Asami *et al.* 1990, Malmivuo and Plonsey 1995, Elshabini and Barlow 1998, Grimnes and Martinsen 2000). 26
- Tab. 5.1: Concentration of NaCl in liquid (NaCl conc.) and corresponding conductivity of NaCl electrolyte at 25°C (Sawyer *et al.* 1995). 68
- Tab. 5.2: Conductivity and relative permittivity of materials used for FEM simulation with atheromatous vessel model of Fig. 5.6 (Slager *et al.* 1992, Gabriel *et al.* 1996). 72
- Tab. 5.3: Value set of parameters used for FEM simulation with atheromatous vessel model of Fig. 5.6. 74

## Symbols

Symbols	Meaning	Units (abbreviation)
$\alpha$	Square root of specific resistance	$\Omega^{0.5}\text{cm}$
C	Capacitance	F
$\epsilon_r$	Relative permittivity (dielectric constant)	
$\epsilon_0$	Vacuum permittivity	$8.854 \times 10^{-12} \text{ Fm}^{-1}$
$\mathbb{E}$	Electric fields intensity	V/m
$\phi, V$	Potential (voltage)	V
$f$	Electric frequency	Hz
$\varphi$	Phase	°
$\Gamma_l$	Reflection coefficient	
G	Conductance	S
$\theta$	Angle	°
$h, l, r, w, x, y, z$	Distance	m
$I$	Current	A
$\vec{J}$	Current density	$\text{A/m}^2$
n	Number	
R	Resistance	$\Omega$
S	Sensitivity	$\text{m}^{-4}$
$\rho$	Resistivity	$\Omega \text{ m}$
$\rho_q$	Charge density	$\text{Cm}^{-3}$
t	Time	s
$\sigma$	Conductivity	$\text{Sm}^{-1}$
$\omega$	Angular frequency ( $= 2\pi f$ )	$\text{s}^{-1}$
Z	Impedance	$\Omega$

## Abbreviations

ACS	Acute coronary syndromes
BIC	Balloon impedance catheter
CPE	Constant phase element
CVD	Chemical vapour deposition
dc	Direct current
D-MEM	Dulbecco's modified eagle media
DMSO	Dimethylsulfoxide
FACS	Fluorescence-activated cell sorting
FCS	Fetal calf serum
FEM	Finite element method
hMSCs	Human mesenchymal stem cells
HSV	Herpes simplex viruses
ICF	Impedance change versus frequencies
IS	Impedance spectroscopy
IVUS	Intravascular ultrasound
MBE	Molecular beam epitaxy
MEM	Modified eagle medium
MEMS	Micro electro mechanical system
MOCVD	Metal organic chemical vapour deposition
MOI	Multiplicity of infection
PECVD	Plasma-enhanced chemical vapour deposition
RBCs	Red blood cells
RF	Radio frequency

## 1 Introduction

Chronic diseases led by cardiovascular disease are the largest cause of death in the world since more than 17 million people a year die mainly from heart disease and stroke (Yach *et al.* 2004). According to the World Health Organization (WHO), the number of people dying from heart disease and stroke is increasing and the situation is particularly bad in low and middle-income countries, where 80 percent of deaths from these diseases occur. The main cause of heart attack or stroke is atherosclerosis, a chronic disease affecting the arterial blood vessel and forming multiple plaques within the arteries (Stary *et al.* 1995). The plaque rupture of a blood vessel with the subsequent thrombus formation frequently causes the acute coronary syndromes (ACS). However, most of ACS are triggered by the rupture showing non-critical stenoses in typical X-ray angiography or intravascular ultrasound (IVUS) (Ambrose *et al.* 1988, Fuster *et al.* 1992). Hence, new methods are required to characterize the plaques in vessels for more precise diagnosis of atherosclerosis and for proper therapy monitoring. Recently, thermometry and advanced IVUS technique using elastography or radiofrequency have been developed to characterize the plaque components (Korte *et al.* 2000, Nair *et al.* 2002, Verheye *et al.* 2002). As promising treatments against atherosclerosis, gene therapy (Maekinen *et al.* 2002) and human stem cell therapy (Fazel *et al.* 2006) have been investigated. Especially, the stem cell therapy is increasingly spotlighted as an Epoch treatment for the regeneration of tissue due to avoiding the transplant rejection. To improve the *in vivo* diagnosis and therapy monitoring of atherosclerosis, it is necessary to characterize plaques in vessels sensitively and exactly.

Electrical characterization of tissues has a potential to characterize the plaques in vessels non-destructively and quantitatively. Impedance spectroscopy (IS), one of electrochemical analysis, has been used to measure bioelectric properties of tissue, organs, or human body (Grimnes and Martinsen 2000). Since Waller (1887) and Einthoven *et al.* (1913) recorded bioelectric signal from the heart, the scientists in the field of biomedical engineering have measured the frequency dependent electrical properties, conductivity and permittivity, of different tissues or organs by using IS (Gabriel *et al.* 1996). Slager *et al.* (1992) have measured *in vitro* the resistivity of the normal intima, fibro connective tissue, and fibro-fatty of dissected human aorta by using a spot electrode (area  $\approx 0.1 \text{ mm}^2$ ) in conjunction with a large plate electrode (area  $\approx 4 \text{ cm}^2$ ). Konings *et al.* (1997) have developed an intravascular impedance catheter with the array of 5 annular voxels and have constructed the impedance distribution of a human iliac artery, which includes three black disk-shaped plastic droplets representing fatty lesions of  $8 \text{ mm}^2$ . To maximize the sensitivity on the impedance characterization of plaques in vessels, the use of balloon impedance catheters (BIC) which consists of microelectrodes integrated with typical balloon catheter was considered theoretically (Stiles and Oakley 2003). Since the microelectrodes contact with intima according to the inflation of balloon, the impedance measurement of vessels can avoid the disturbance of intravascular condition (e.g. velocity or viscosity of blood component) and therefore can be more sensitive and stable. Stiles and Oakley (2003) have deigned a BIC with quasi-atheromatous vessel models and simulated the intravascular impedance of aortas containing different plaque types by using finite element method (FEM). However, so far, the utilization of BIC for the intravascular impedance measurement of vessels has been limited due to the difficulty in fabrication of microelectrodes durable to in- and deflation of balloon, and the lack of

knowledge for the interpretation of IS data measured on such a thin and small vessel walls.

The goal of this thesis is to investigate the feasibility of IS based on micro electro mechanical system (MEMS) technology for the intravascular electrical diagnosis and therapy monitoring of atherosclerosis. For the intravascular impedance measurement of vessels by using BIC, it is required to fabricate MEMS-based transducers for BIC used under the spatial conditions *in vivo*. Together, it needs to investigate whether MEMS-based IS can be used to characterize the alterations of cells/tissues related to atherosclerotic plaques and pathologies with such sensitivity and reproducibility that relevant medical parameters are determinable. Before describing the research in detail, the theoretical backgrounds are briefly introduced as follows.

### 1.1 Atherosclerosis

Atherosclerosis causes a hardening of an artery due to an atheromatous plaque. Fig. 1.1 shows changes in endothelial dysfunction as the progression of atherosclerosis (Stary *et al.* 1995). Atherosclerosis typically begins in early adolescence, and the plaque

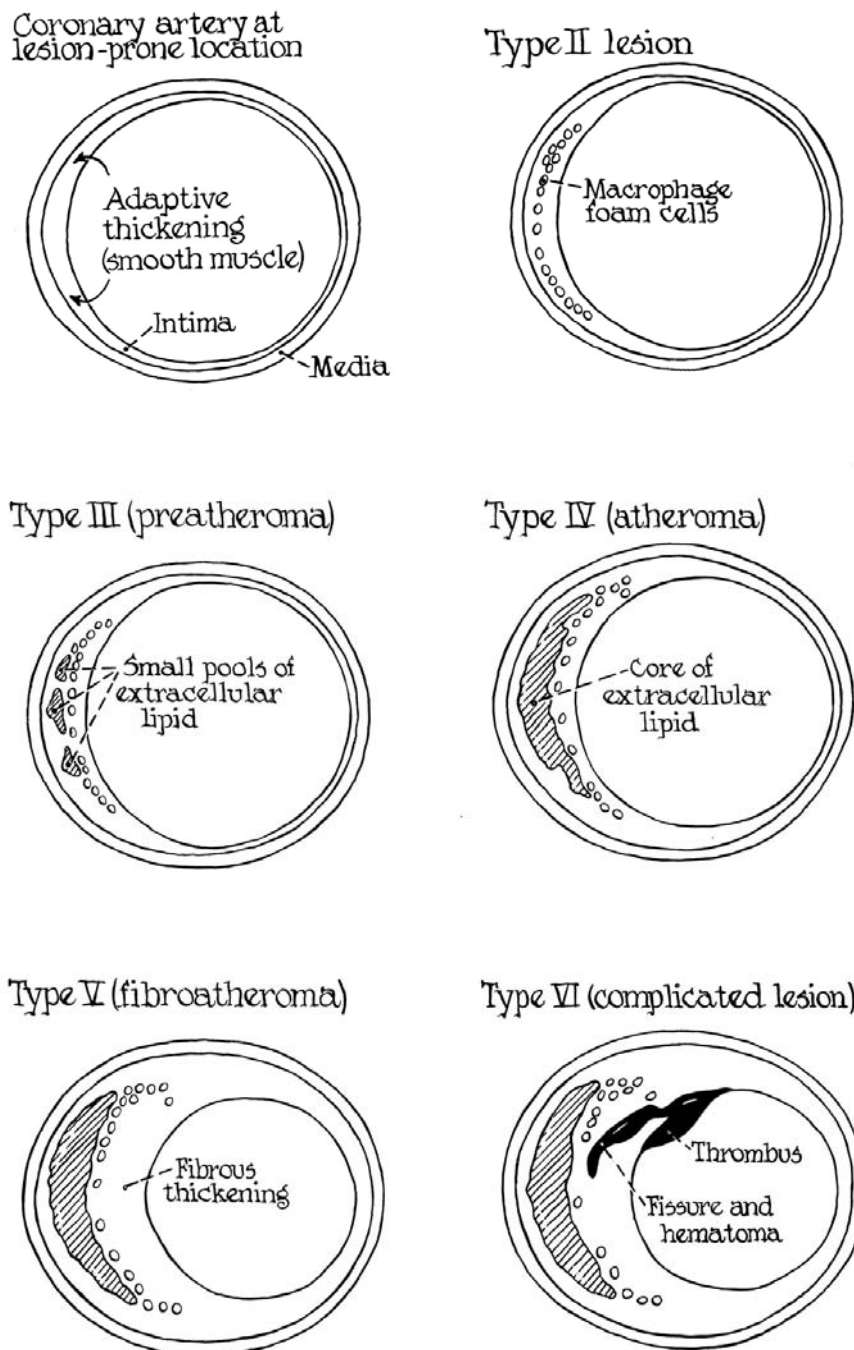


Fig. 1.1: Changes in endothelial dysfunction during progression of atherosclerosis (Stary *et al.* 1995).

initially grows without showing any stenosis of the lumen. In the advance on disease, the fatty streaks or small subendothelial deposits of lipid are developed and formed into atheromatous plaques. The atheromatous plaques are defined as the nodular accumulation of lipid material with possibly cholesterol crystals and calcification at near the lumen in the artery. Fig. 1.2 shows a photomicrograph of atheroma in coronary artery with extracellular lipid core and cholesterol crystals. These atheromatous plaques eventually lead to plaque ruptures, thickening the artery wall, and the stenosis of the artery. However, most commonly, a vulnerable plaque causing the formation of a thrombus is particularly prone to produce sudden major event called infarction, such as a heart attack or stroke (Stary *et al.* 1995). The thrombus rapidly slows or stops blood flow and leads to damage or death of the tissues fed by the artery in several minutes. The majority of events occur due to atheromatous plaque rupture at areas showing non-critical stenoses although the stenotic area is detectable by typical angiography and IVUS (Ambrose *et al.* 1988, Fuster *et al.* 1992).

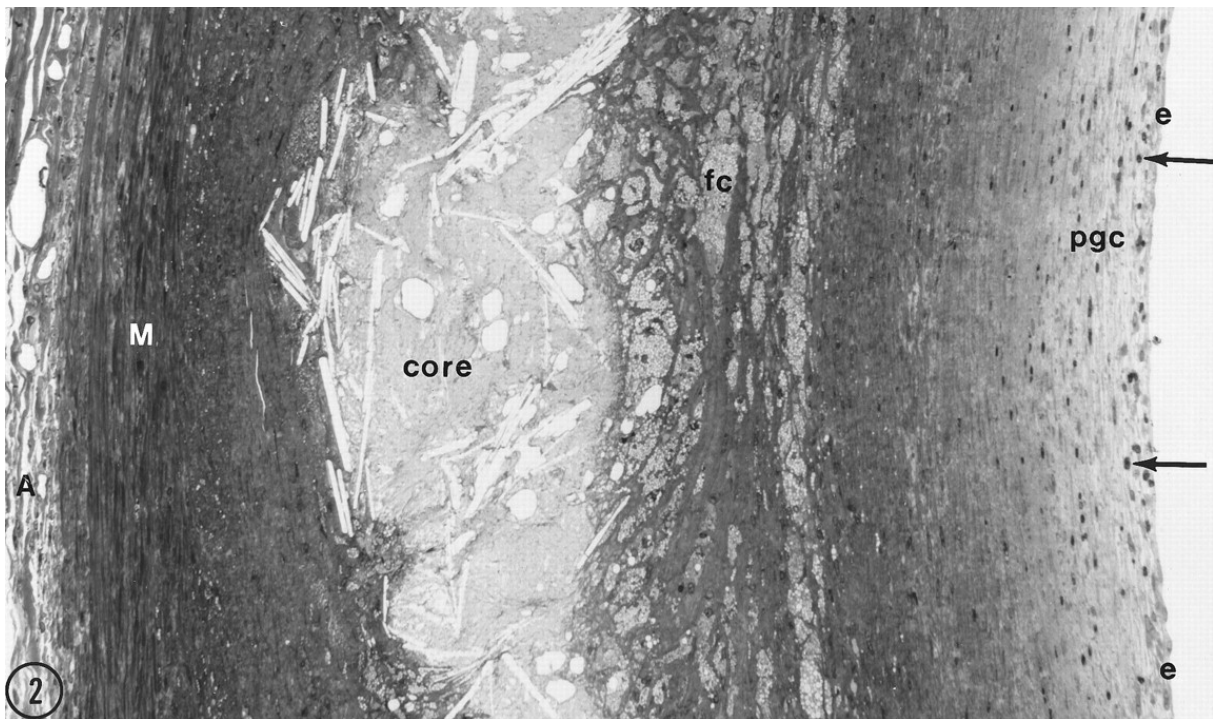


Fig. 1.2: Photomicrograph of atheroma in coronary artery. A: adventitia, M: media, core: extracellular lipid with cholesterol crystals, fc: macrophage foam cells, arrow: macrophages that are not foam cells, pgc: proteoglycan layer, e: endothelium, magnification about x220 (Stary *et al.* 1995).

For the treatment against atherosclerosis, cardiologists and vascular surgeons use angioplasty, stent placement, vascular graft surgery, endarterectomy, and prosthesis operations. However, since these procedures can cause thrombosis, it is necessary to find new therapies avoiding the side effect and curing the cause of atherosclerosis. To understand the cause of disease and to develop the effective treatment against atherosclerosis, various physiological and pathological studies have been performed. It has

been suggested that alterations in lipid metabolism, arterial injury, or the effects of chemical or viral mutagens on vascular smooth muscle cells may cause atherosclerosis (Ross and Glomset 1976, Minick 1976, Benditt 1976). It was found that the infection with Marek's disease herpes virus leads to occlusive atherosclerosis of large muscular arteries of chickens (Fabricant *et al.* 1978) and that latent infection of vascular cells with herpes simplex viruses (HSV) is related with the development of human atherosclerosis (Key *et al.* 1990). For new therapies against atherosclerosis, Maekinen *et al.* (2002) have reported that atherosclerosis is not worse in human body after local vascular endothelial growth factor gene therapy. Fazel *et al.* (2006) have tried clinically bone-marrow stem cell therapy for myocardial infarction and suggested the potential therapeutic effect of specific paracrine pathways for angiogenesis in improving cardiac function in the injured heart.

## 1.2 Electrical Properties of Cells and Tissues

The cell is the basic component of tissues. Cells have a membrane, ultra-thin layer surrounding the intra cellular fluid, the cytoplasm (Curtis and Barnes 1990). The cell membrane is composed of bi-layer lipids, membrane proteins, transport organelles, and ionic channels for the electrogenic pumps (Fig. 1.3). By the sodium/potassium pumps of the active ionic channel, the interior potentials of excitable and non-excitable cells are about  $-70$  mV and  $-10$  mV to  $-20$  mV with respect to the extra cellular liquid, respectively (Grimnes and Martinsen 2000). If the difference of direct current (dc) potential over the cell membranes is above than  $150$  mV, the membrane of cell breaks down. Hodgkin and Huxley (1952) have measured the membrane conductance during a nerve cell excitation. Fig. 1.4 shows that the membrane conductance for certain ions increases abruptly within  $1$  ms and the ionic channels open up for several hundreds of  $\mu$ s when a muscle or nerve cell is excited. Cole (1972) and Takashima and Yantorno (1977) have studied the voltage

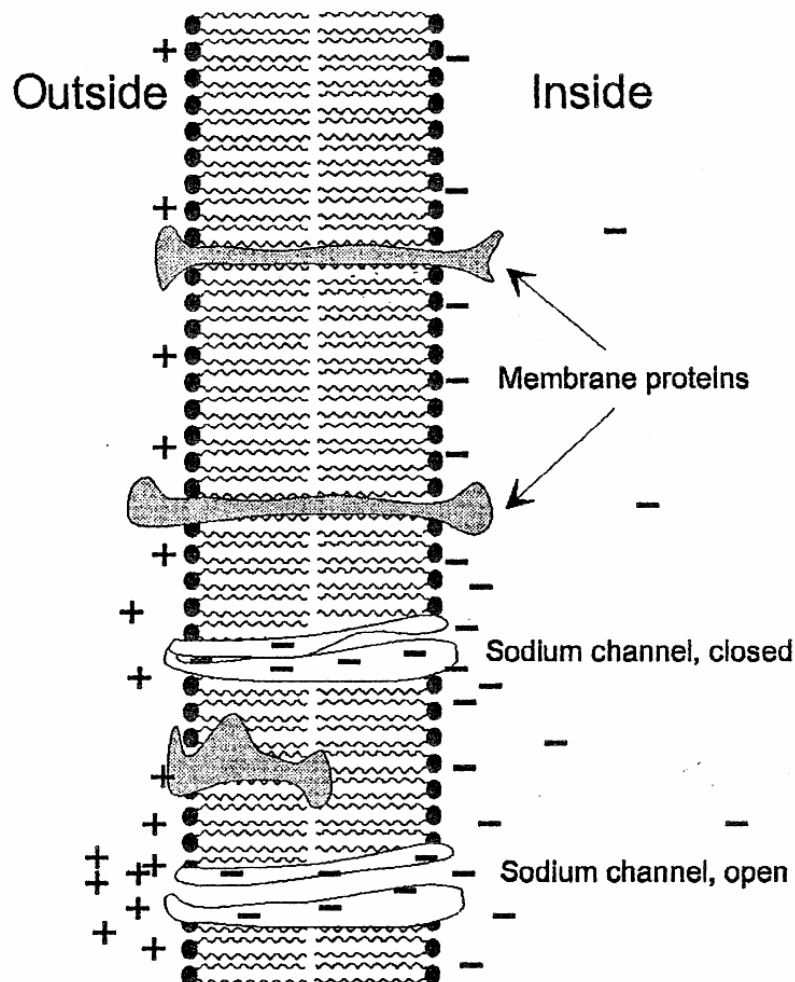


Fig. 1.3: Schematic of bi-layer lipid membrane with embedded proteins and sodium channels (Grimnes and Martinsen 2000).

dependence of the cell membrane capacitance. Takashima and Schwan (1974) have investigated the passive electrical properties of the excitable membrane of squid axon and have shown that when the frequency increases from 1 kHz to 50 kHz the membrane capacitance decreases from  $1 \mu\text{F}/\text{cm}^2$  to about  $0.6 \mu\text{F}/\text{cm}^2$  but the membrane conductivity increases from  $1.2 \text{ mS}/\text{cm}^2$  to  $40 \text{ mS}/\text{cm}^2$ . Asami *et al.* (1990) have measured the impedance spectra of membrane of HeLa and Myeloma by using the micropipette technique, and have found that the conductance and capacitance of the membrane are about  $100 \mu\text{S}/\text{cm}^2$  and  $1.0 \mu\text{F}/\text{cm}^2$  to  $1.9 \mu\text{F}/\text{cm}^2$  in the frequency range of 1 Hz to 1 kHz.

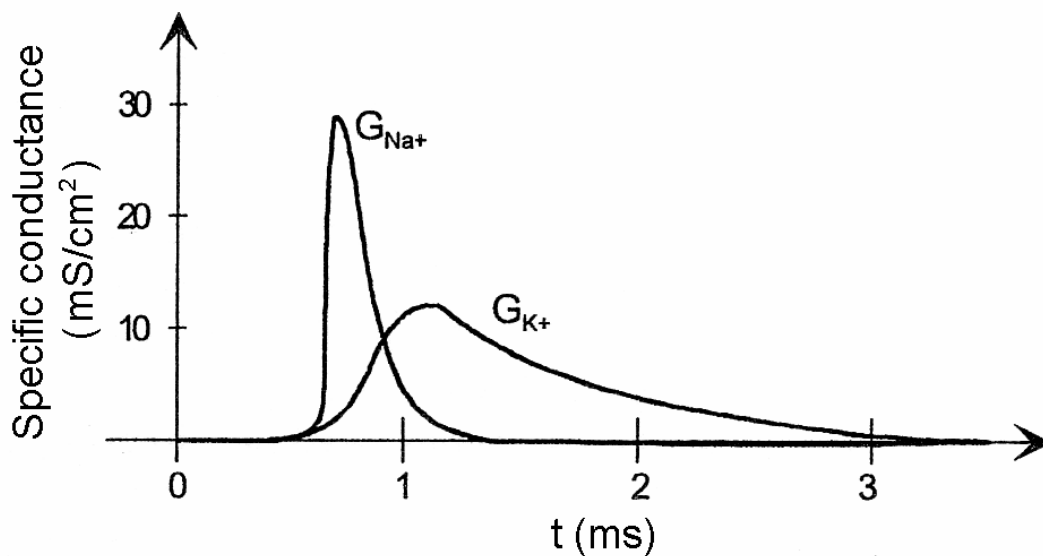


Fig. 1.4: Membrane conductance during cell excitation (Hodgkin and Huxley 1952),  $G_{\text{Na}^+}$ ,  $G_{\text{K}^+}$ : specific membrane conductance caused by  $\text{Na}^+$  and  $\text{K}^+$  ions, respectively.

The cell assemblies or tissues containing the different cellular size and orientation can be regarded as an inhomogeneous and anisotropic dielectric material. The electrical impedance of cell assemblies/tissues is dependent on the cellular structure and the frequency of electric fields as well. When electric fields are applied externally to tissue, the dipoles are formed with bound ions, and the tissue is polarized (Malmivuo and Plonsey 1995). Polarization is the disturbance of the charge distribution in a region caused by the electric fields (Grimnes and Martinsen 2000). If the frequency of electric fields is low enough to allow all charges in the tissue to change their position, the polarization of tissue is maximal. The time dependence of polarization was characterized by the relaxation process. Debye (1929) used the relaxation theory to explain the time required for dipolar molecules to orient themselves. The frequency domain concept of relaxation is dispersion. Schwan (1957) have found the frequency dependence of permittivity of typical soft tissues and classified the dispersion regions, where the permittivity changes, into three groups ( $\alpha$ ,  $\beta$ , and  $\gamma$ ). On the region of the first dispersion ( $\alpha$ ), about 10 Hz and 10 kHz, the variance of permittivity is caused by ionic diffusion and surface ionic conduction at the boundaries of cell membrane. In this frequency range, the current flows through the extra

cellular space, and therefore the impedance of tissues is strongly determined by the extra cellular conditions (e.g. volume or conductivity  $\sigma$ ). The second dispersion ( $\beta$ ) is observed in the frequency range of about 100 kHz to 10 MHz and caused by the capacitance of cell membrane. In this frequency range, the current flows through the extra and intra cellular space. The third dispersion ( $\gamma$ ) is appeared in the frequency range of about 1 GHz to 100 GHz and caused by the relaxation of the water molecules. The electrical properties of tissues vary from the liquid tissue flowing through the vessel to fat or bone. The conductivity and relative permittivity of various tissues measured at different temperatures and frequencies were arranged and reviewed by Foster and Schwan (1989) and Gabriel *et al.* (1996).

### 1.3 Impedance Spectroscopy (IS)

Using impedance spectroscopy (IS), the electrical properties of biological materials according to the physiological and morphological change can be measured. Under linear conditions, when an alternating current ( $I$ ) source with certain frequency is applied to materials, the response can be an alternating voltage ( $V$ ). Fig. 1.5 shows these alternating signals, the applied current and measured potential, in a dielectric material. Due to the dielectric properties of materials, the differences of phase and amplitude between the source and response signal are observed. When the alternating current is applied with the amplitude of  $I_o$  and phase of  $\phi_I$  as

$$I = I_o e^{i(\omega t + \phi_I)} \quad (\text{eq. 1.1})$$

then the measured potential with the amplitude of  $V_o$  and phase of  $\phi_V$  is

$$V = V_o e^{i(\omega t + \phi_V)} \quad (\text{eq. 1.2})$$

where  $i = (-1)^{1/2}$ ,  $\omega$  is the angular frequency ( $= 2\pi f$  with the frequency of  $f$ ), and  $t$  is time.

The electrical impedance ( $Z$ ) is the ratio of  $V$  to  $I$  and have the amplitude of  $Z_o$  and phase of  $\theta$ .

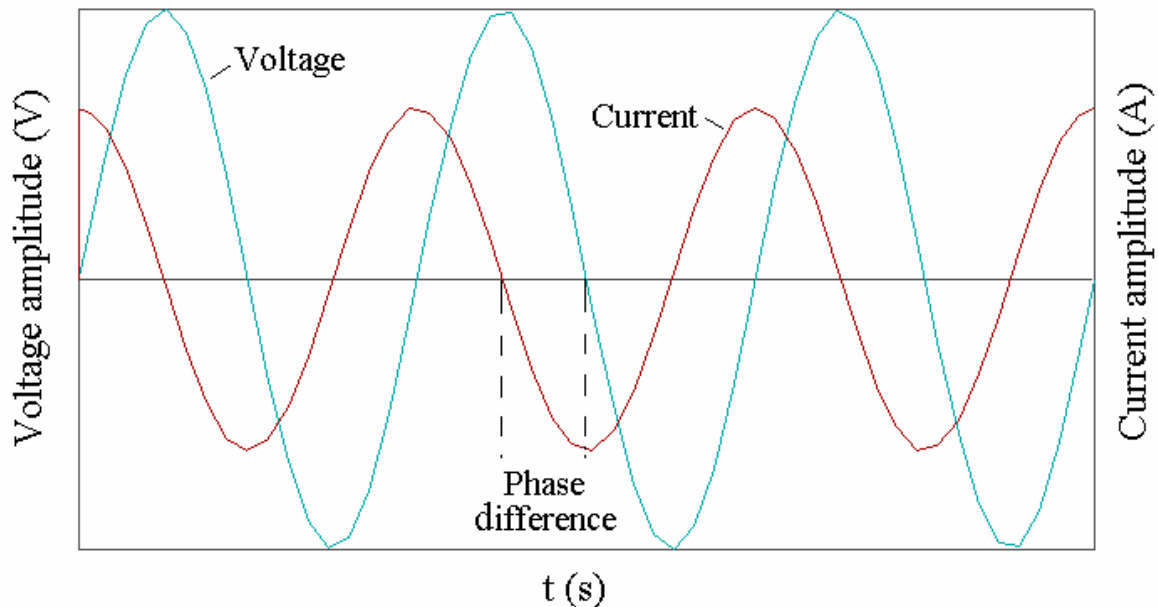
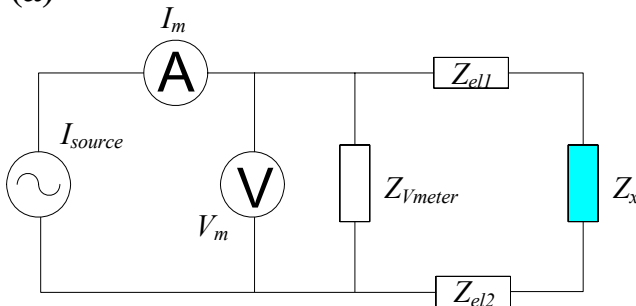


Fig. 1.5: A voltage response when the alternating current is applied in a dielectric material.

$$Z = \frac{V}{I} = \frac{V_o e^{i(\omega t + \phi_V)}}{I_o e^{i(\omega t + \phi_I)}} = \frac{V_o}{I_o} e^{i(\phi_V - \phi_I)} = Z_o e^{i\theta} \quad (\text{eq. 1.3})$$

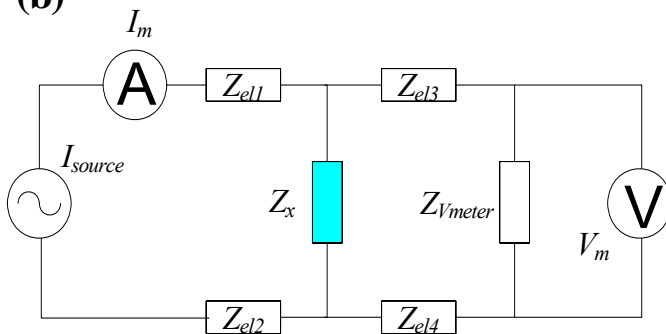
To measure the impedance, the electrodes for applying the source and measuring the response are needed. According to the number and configuration of used electrodes, the measurement can be called two- or four-electrode method. Fig. 1.6 shows the configuration of two- and four-electrode method and the impedances measured by each method. When an alternating current is the source flowing through the amperemeter, the potential response is recorded by voltagemeter. The input impedance of voltagemeter is so high that no current flows through it. In two-electrode method of Fig. 1.6 (a), when the current flows through the electrodes and object, the recorded total potential is the sum of potentials generated over the electrodes and object. The configuration of two-electrode method seems simpler than the four-electrode; however, the electrode impedance is included in the total impedance measured by the two-electrode method. The electrode impedance is characterized by electrical double layers and diffusion on the electrode (Bard and Faulkner 2001). When the electrodes are contacted to electrolyte, an electrostatic

(a)



$$Z_m = \frac{V_m}{I_m} = Z_x + Z_{el1} + Z_{el2} \quad \left| \quad Z_{Vmeter} \gg Z_{eln} \right.$$

(b)



$$Z_m = \frac{V_m}{I_m} = Z_x \quad \left| \quad Z_{Vmeter} \gg Z_{eln} \right.$$

Fig. 1.6: Configuration and measured impedance with two- (a) and four-electrode method (b),  $I_{source}$ : alternating current source,  $I_m$ : current measured by amperemeter (A),  $V_m$ : measured voltage by voltagemeter (V),  $Z_{eln}$ : nth electrode impedance,  $Z_{Vmeter}$ : impedance of voltagemeter,  $Z_m$ : measured impedance,  $Z_x$ : impedance of object.

interaction occurs between the ions in the electrolyte and electrode surface (Langmuir 1929). The attracted ions make a charged layer on the electrode surface for neutralization, and therefore the electrical double layer is formed on the electrode. In addition, the ions concentrating at the electrode result in the diffusion of ions near the electrode. As the electrode area or the frequency decreases, the electrode impedance more contributes to the total impedance. If the electrode impedance is too high, the impedance of objects on electrodes may not be distinguished from the impedance measurement. However, the four-electrode method can avoid the electrode impedance theoretically. As shown in Fig. 1.6 (b), the potential over object is only recorded by a pair of electrode while the current flows through the object with another pair of electrode. If the impedance of voltagemeter is high enough that the electrode impedance is ignorable, the potential generated over the object is equal to the potential measured by the voltagemeter.

## 1.4 Micro Electro Mechanical System (MEMS) Technology

Micro electro mechanical system (MEMS) technology is a technique to make the electro mechanical system on a micro scale. To facilitate impedance measurements *in vivo* and to increase the measurement resolution on the cellular scale, the dimension of electrode system should be adapted to the sample. Normally, thin film technology is used to fabricate MEMS devices due to its high precision. The process of thin film technology consists of the film deposition and the pattern generation. Fig. 1.7 illustrates the classification of the different deposition processes. Sputtering, a physical vapour deposition process, accomplished by bombarding the source material on a solid cathode with positive ions emitted from a rare gas discharge. Chemical vapour deposition (CVD) uses reactive carrier gases to decompose the desired material and to deposit the reaction products to the substrate surface.

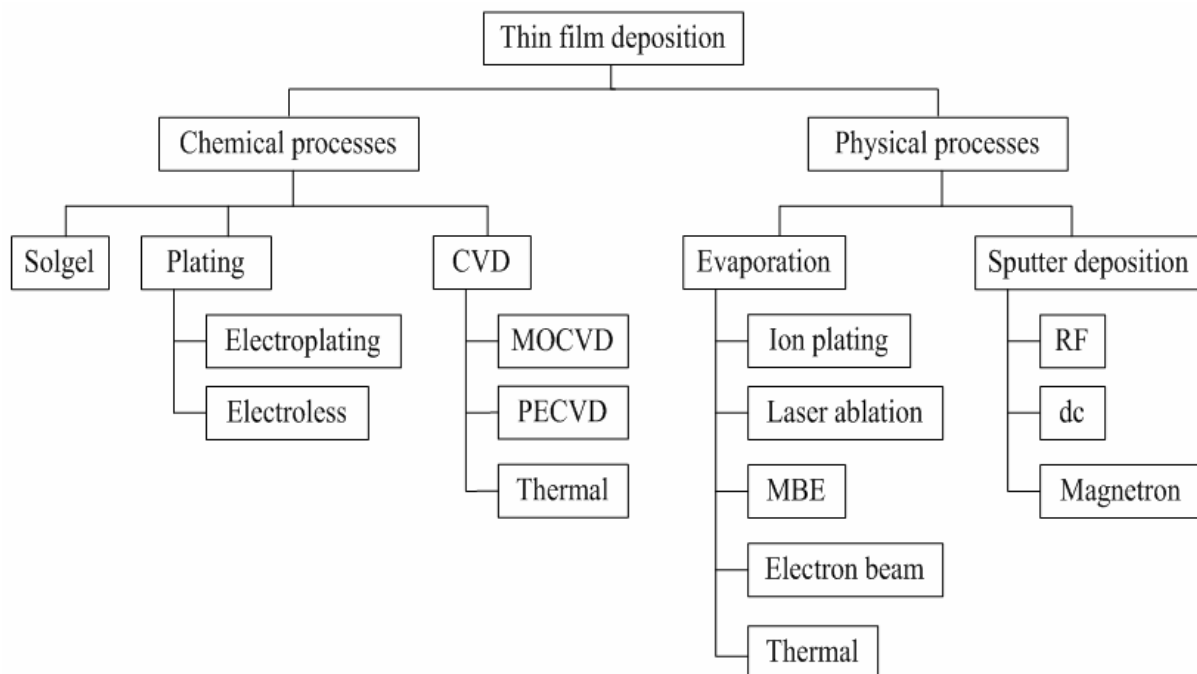


Fig. 1.7: Classification of the most common deposition processes, CVD: Chemical vapour deposition, MOCVD: Metal organic CVD, PECVD: Plasma enhanced CVD, MBE: Molecular beam epitaxy, RF: Radio frequency, dc: Direct current (Elshabini and Barlow 1998).

For the pattern generation, lithographic technique is used. Lithographic processes determine substrate regions for subsequent etching removal or materials addition (Elliott 1986). There are wet and dry etching methods often used. In wet etching, usually a strong acid or base solution is used to etch the substrate immersed in a liquid etch bath. Wet etching is isotropic meaning that the etch rate is the same in all directions for most substrates. In dry etching, the substrate is exposed to gases in an excited state (plasma). These ions of plasma can etch the exposed substrate surface anisotropically.

Using this thin film technology, the integration of the conductor and insulated materials is fabricated for micro sensors using IS. Gold (Au) and platinum (Pt) are good materials for the electrode or conductive films due to their high electrical conductivity. At 20°C, the conductivity of Au and Pt are  $4.5 \times 10^5$  S/cm and  $9.5 \times 10^4$  S/cm, respectively (Elshabini and Barlow 1998). These materials have excellent corrosion resistance and are compatible with wire-bonding attachment techniques. Further, Au and Pt electrodes are biocompatible and electrochemically stable (Sawyer *et al.* 1995, Thanawala *et al.* 2007). For the insulated or dielectric materials, silica ( $\text{SiO}_2$ ), silicon nitride ( $\text{Si}_3\text{N}_4$ ), or polyimide is often used due to their high electrical resistivity. The dielectric constant and electrical resistivity of  $\text{SiO}_2$ ,  $\text{Si}_3\text{N}_4$ , and polyimide at room temperature are shown in Tab. 1.1.

Tab. 1.1: Electrical properties of  $\text{SiO}_2$ ,  $\text{Si}_3\text{N}_4$ , and polyimide at room temperature (Srivastava *et al.* 1985, Elshabini and Barlow 1998, Awan and Gould 2003, Deligöz *et al.* 2006).

Material	Dielectric constant	Electrical resistivity ( $\Omega\text{cm}$ )
$\text{SiO}_2$	3 – 4	$10^9 - 10^{14}$
$\text{Si}_3\text{N}_4$ (100 Hz – 20 kHz)	5 – 6	$2 \times 10^8 - 5 \times 10^{11}$
Polyimide (10 kHz – 6 MHz)	2 – 4	$3 \times 10^6 - 6 \times 10^9$

## 1.5 Finite Element Method Simulation

Finite element method (FEM) is a numerical analysis technique to get solutions to the differential equations describing various problems. To predict or to demonstrate the electrical characterization of a system, a simulation using FEM is often used due to its high precision even in the complicated geometries. Using this FEM, the electrical characteristics of object (e.g. distribution of electric fields, impedance) can be estimated. The schematic of simulation process with FEM to solve physical problems is shown in Fig. 1.8. To use FEM for model-based physical simulation, it is premised that the complicated whole domain can be sub-divided into a series of small regions in which the differential equations are approximately solved (*discretization*). The small regions called element are connected at specific points called nodes. In each element, the solution to the governing equation is replaced by a continuous approximating function. From assembling the set of equations for each element, the behaviour over the entire domain can be estimated (*solution*). For the assembling process, it is required that the solution be continuous along common boundaries of adjacent elements.

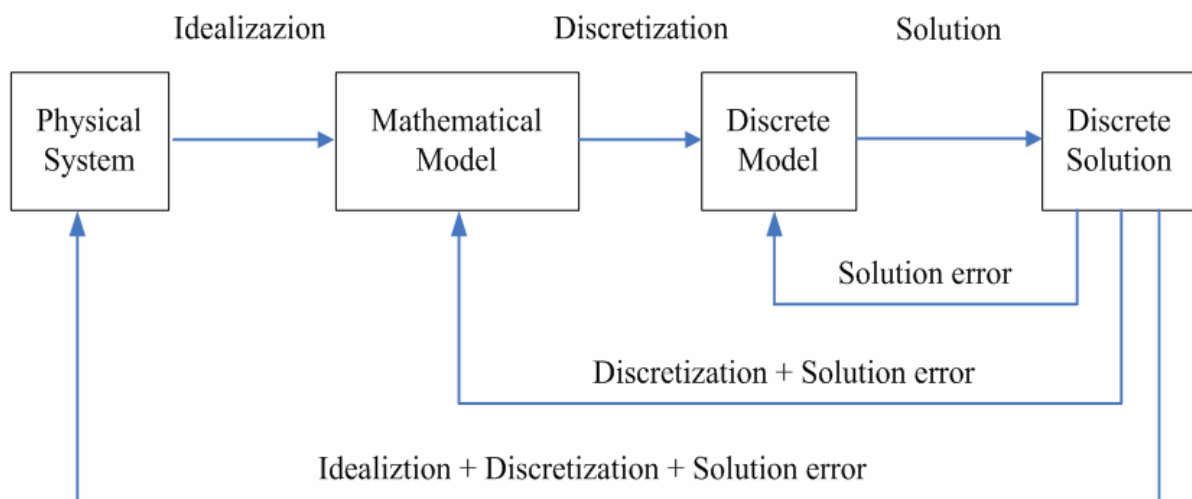


Fig. 1.8: Schematic of simulation process with FEM for solving the physical problems (Carlos 2004).

A FEM theorem for electrostatics is shown here. The electric fields are idealized by Maxwell's equations (Maxwell 1873). When the inductive influences of time-varying currents can be neglected, the governing equation in the homogeneous region can be the Poisson's equation.

$$\nabla^2 V = -\frac{\rho_q}{\epsilon_0} \quad (\text{eq. 1.4})$$

where,  $V$  is the potential, and  $\rho_q$  the charge density and  $\epsilon_0$  the permittivity of vacuum.

When an approximating function  $\phi$  substitute for  $V$  for in (eq. 1.4), a residual occurs. The residual is multiplied by a weighting function  $N_i$  (shape function), integrated in an element domain  $\Omega_e$ , and set to zero for the best approximation (Galerkin approach with method of weighted residuals).

$$\int \left( \nabla^2 \phi + \frac{\rho_q}{\epsilon_0} \right) N_i d\Omega_e = 0, \quad \phi = \sum_{i=1}^m N_i \phi_i \tag{eq. 1.5}$$

where,  $m$  is the number of element nodes and  $\phi_i$  element nodal unknowns.

If a two-dimensional domain is discretized into a number of triangular shaped elements as Fig. 1.9, each element has boundaries and nodes with unknown nodal values ( $\phi_1, \phi_2,$  and  $\phi_3$ ).

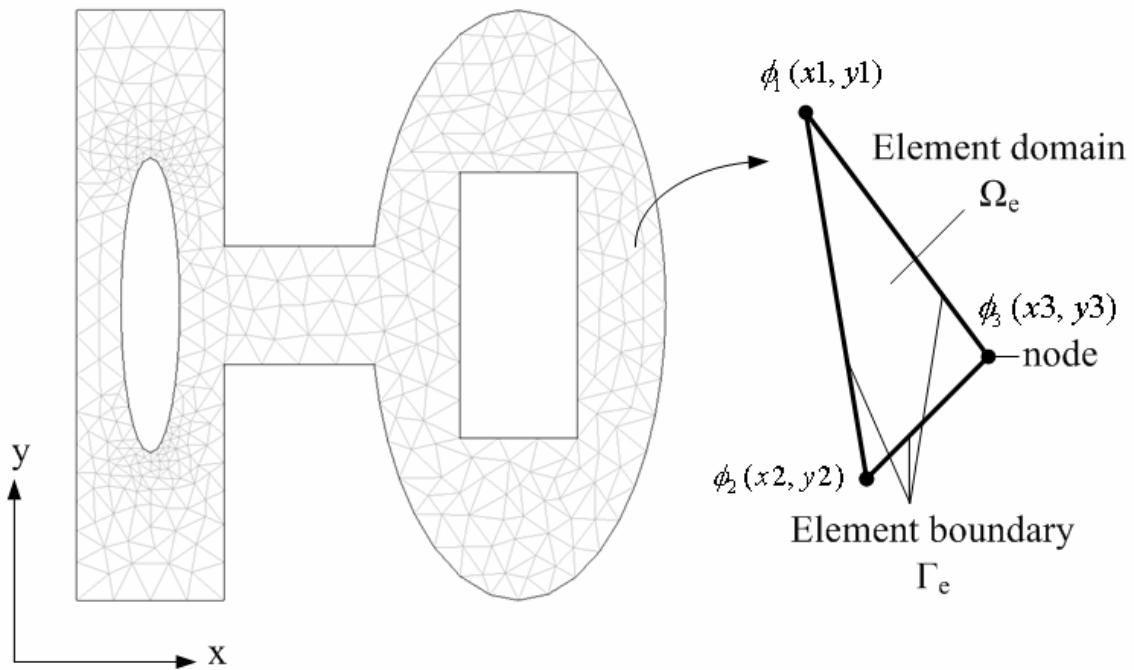


Fig. 1.9: Two-dimensional domain discretized into a number of triangular shaped elements,  $\phi_1, \phi_2,$  and  $\phi_3$  are unknown nodal values.

From the integration by parts, (eq. 1.5) is developed as follows.

$$\begin{aligned} & \int \int_{\Omega_e} \sum_{j=1}^3 \left( \frac{\partial N_i}{\partial x} \frac{\partial N_j}{\partial x} + \frac{\partial N_i}{\partial y} \frac{\partial N_j}{\partial y} \right) \phi_j dx dy \\ & = \int \int_{\Omega_e} \frac{\rho_q}{\epsilon_0} N_i dx dy + \int \frac{\partial \phi}{\partial x} N_i dy + \int \frac{\partial \phi}{\partial y} N_i dx \end{aligned} \tag{eq. 1.6}$$

The element equation (eq. 1.6) is an element matrix which can be calculated by e.g. Gauss-Elimination. Finally, the whole system matrix is setup by assembling the element equations.

## 1.6 Biomedical Applications of MEMS with IS

For the characterization of cell subsets, flow cytometry using IS has been developed. In conventional flow cytometry, such as fluorescence-activated cell sorting (FACS), cells are labeled. However, the use of cell markers may inherently modify the cells. The micro fabricated flow cytometer with IS permits a rapid and label-free dielectric characterization of cell populations in micro fluidic channels. At the low frequencies, the cell volume or size can be analyzed. The properties of plasma membrane and cell interior can be measured at higher frequencies. Using a micro fluidic chip as Fig. 1.10, Cheung *et al.* (2005) measured impedance of three cell models: red blood cells (RBCs), ghost cells, and RBCs fixed in glutaraldehyde in the frequency range of 350 kHz to 20 MHz. Ghost cells have similar membrane properties of RBCs, but different cytoplasmic properties. RBCs fixed in glutaraldehyde have different dielectric properties from the membrane and cytoplasm of normal RBCs. In this chip, face-to-face strip electrodes are patterned onto the top and

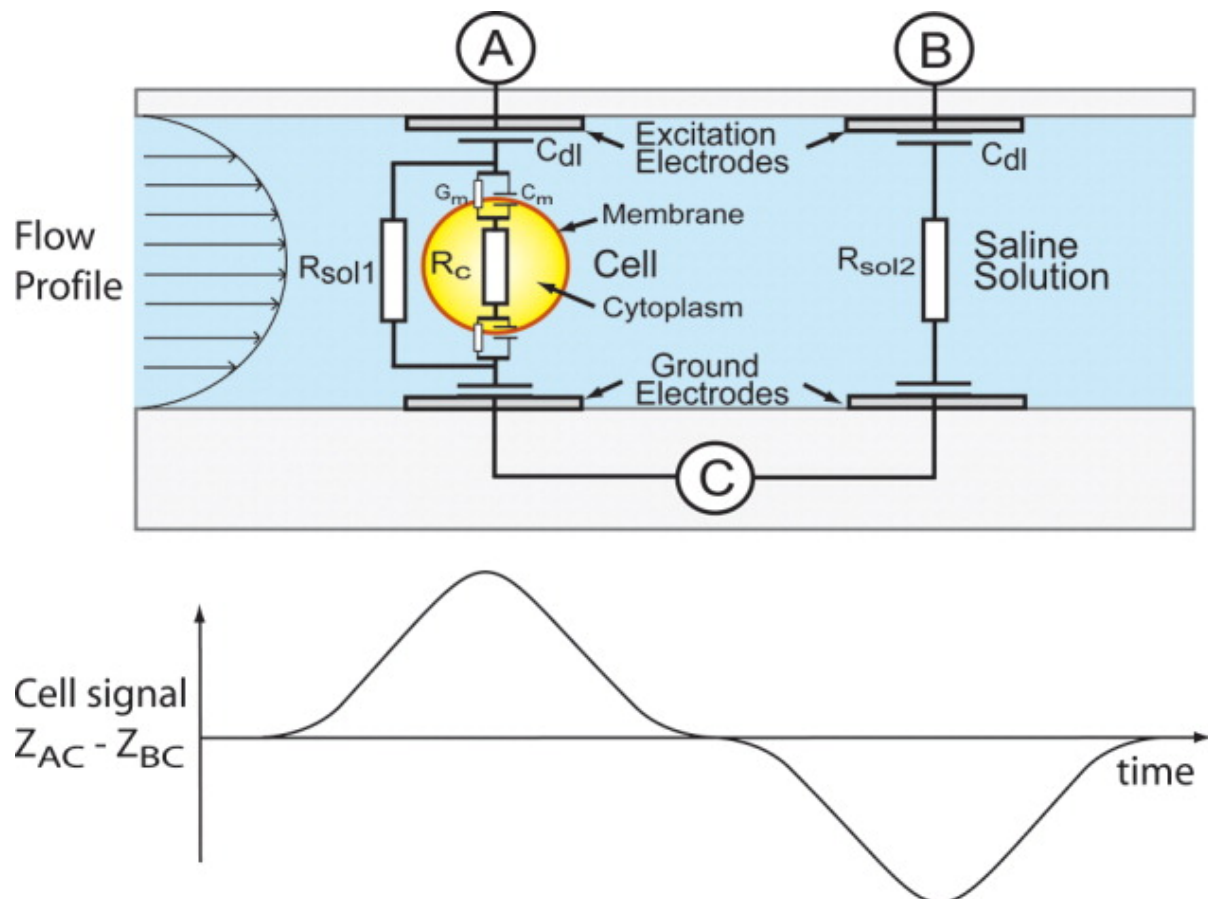


Fig. 1.10: Schematic of micro fluidic channel with a sample cell passing between the pairs of electrode (AC and BC) (upper), impedance difference monitored as the cell passes through the channel (below),  $C_{dl}$ : double layer capacitance on the electrode surface,  $G_m$  and  $C_m$ : conductance and capacitance of membrane,  $R_{sol1}$  and  $R_{sol2}$ : solution resistance,  $R_c$ : resistance of cytoplasm (Cheung *et al.* 2005).

bottom surfaces of the micro channel. The channel height is 20  $\mu\text{m}$  and channel width is 40  $\mu\text{m}$  at the measurement electrodes which are 30  $\mu\text{m}$  wide. By negative dielectrophoresis, the cells flow along the centerline of the channel. During the cell flowing, the impedance difference ( $Z_{AC} - Z_{BC}$ ) is measured by the electrodes A, B, and C arranged in Fig. 1.10.

For *in vitro* monitoring of cells or tissues during the cultivation under specific environments, a microelectrode-based chip using IS can be used as Fig. 1.11. For the impedance measurement of cells related with those behaviours *in vitro*, the planar electrode-based chip has been pioneered by Giaever and Keese (1991, 1993). Giaever and Keese have measured the impedance of cells on electrodes at the frequency of 4 kHz and found that the measured impedance magnitude or resistance is increased as the increase of cell densities on the electrode during the cultivation (Fig. 1.11). The adhesion and spreading of different cells onto electrodes were characterized electrically during the cultivation (Mitra *et al.* 1991, Lo *et al.* 1995, Wegener *et al.* 1996, Ehret *et al.* 1997, Luong *et al.* 2001). For the cytotoxicity tests, the impedance of cells on the electrode was measured in real time while applying test substances (Xiao *et al.* 2002, Xiao and Luong 2005). The morphological changes as the responses of cells to chemical and physical stimulations were investigated by using the electrical method (Smith *et al.* 1994, Ochoa *et al.* 1997, Noiri *et al.* 2001). During the apoptosis or chemotaxis, the impedance changes

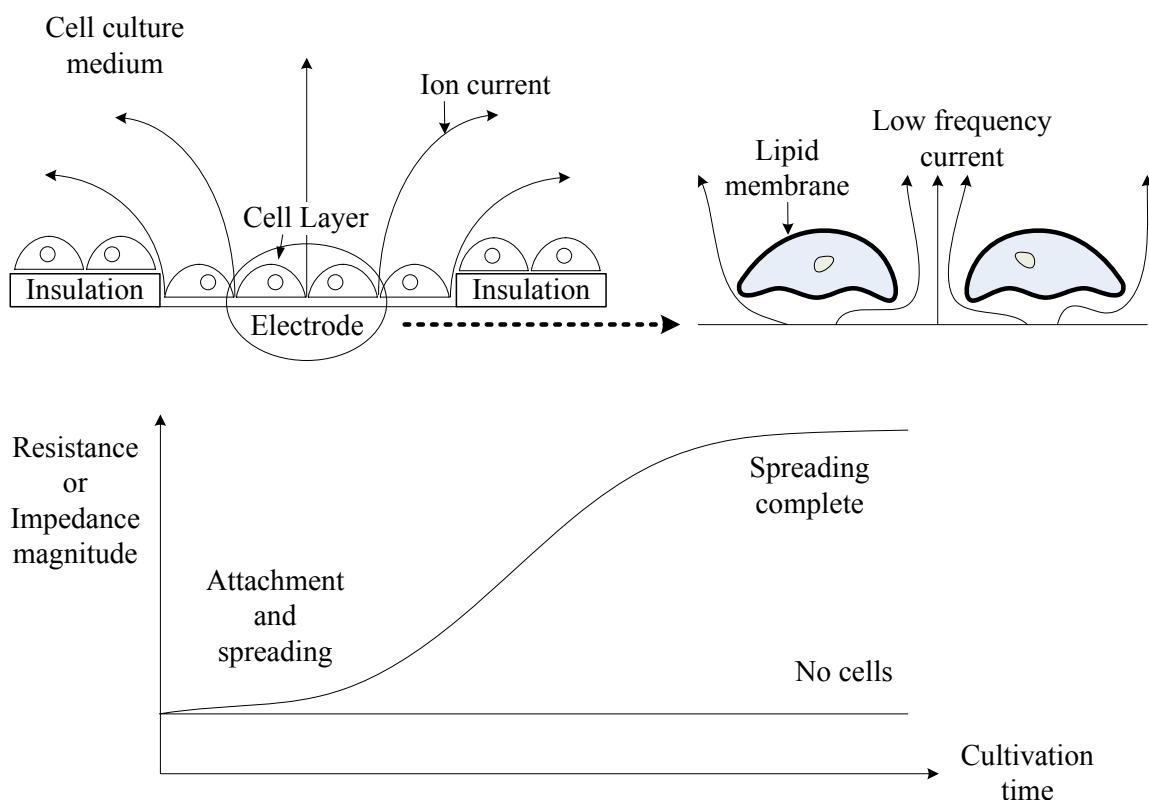


Fig. 1.11: Schematic of microelectrode-based cell chip, below: impedance recorded at the frequency of 4 kHz during the cell growth on the electrode (Giaever and Keese 1993).

related with cell shape and migration were monitored (English *et al.* 1999, Hadjout *et al.* 2001, Arndt *et al.* 2004). The cell pathology was investigated by the electrode-based cell chip with impedance spectroscopy for the development of therapies or drugs (Sharma *et al.* 2001, Lundien *et al.* 2002). By using the FEM simulation, the distribution of electric fields and the impedance of cells/electrode interface have been investigated with respect to the cell coverage and adhesion on electrodes (Rutten *et al.* 2001, Huang *et al.* 2004). This label-free cell chip and IS can replace or supplement the traditional monitoring of cells by using microscopy with fluorescent or radioactive labels.

Another application of MEMS for IS is micro probes for measurement *in vivo*. For *in vivo* diagnoses, endoscopy or ultrasound method is often used. As a supplemental diagnosis for the conventional methods, the micro structure with IS can provide the quantitative information about physiological changes in tissues e.g. ischemia, viable state, water content. Ivorra *et al.* (2003) fabricated a needle shaped probe with four-terminal electrode arrangement and measured impedance in the rat kidney during the ischemia and reperfusion (Fig. 1.12). The occlusion of renal vascular induces the gradual increase of

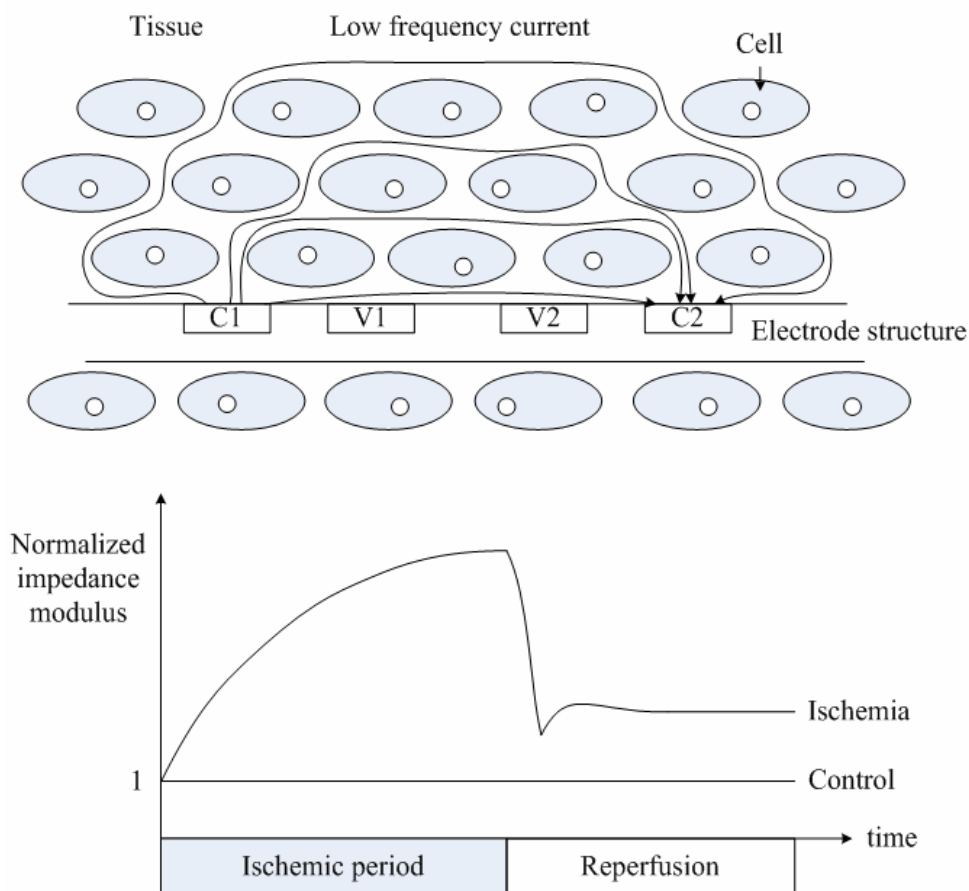


Fig. 1.12: Schematic of needle shaped microelectrode array implanted in the tissue, C1, C2: current applying electrodes, V1, V2: voltage measurement electrodes, below: impedance monitored during the ischemia and reperfusion (Ivorra *et al.* 2003).

impedance at low frequencies, because the cells in rat kidney are swelled and the extra cellular space is decreased during the ischemia. By the reperfusion, the impedance is rapidly decreased, but not returned to its original value. It is expected that the ischemia causes some kind of permanent damage to the tissue.

In the department of Biohybrid Systems, Fraunhofer IBMT, MEMS-based IS has been used to characterize the cells and tissues for the drug development and pharmacological screening. For the impedance characterization of tissues on cellular level, Thielecke has developed a microelectrode-based chip which has a single hole at the center of electrode (Thielecke *et al.* 1999). By controlling the micro fluidics through the hole, a single cell was quickly positioned on a circular electrode. Afterwards, the impedance of positioned single cell was measured by using the bottom circular electrode and a large reference electrode over the cell. From the experiment, it was found that the coverage of single cells over the electrode determines the measured impedance. For a drug and biomedical screening of tissues *in vitro* 3D, a micro capillary-based impedance measurement system was developed (Reininger-Mack *et al.* 2001, Thielecke *et al.* 2001a, Thielecke *et al.* 2001b). The 3D tumor spheroid models were positioned in the capillary and then the impedance of tissues were measured. From the experiment, it was shown that the cellular alteration in the tumor by a DNA transfection can be reflected in the impedance measurement.

## 2 Objectives of Study and Appropriate Solutions

As described in chapter 1, impedance spectroscopy (IS) allows to draw conclusions about the state of cells and structures of tissues non-invasively. Up to now IS has been often used in the biomedical field for the characterization of larger samples like the human body, whole organs, or cell suspensions. Only a minor number of papers were published about fluidic cell impedance analysis (e.g. Fuhr *et al.* 1992, 1994). So far, IS has almost not been used for an intravascular characterization of plaque due to the difficult spatial condition in vessels and the lack of knowledge for the interpretation of IS data measured on such small biological samples. Recently, the advance in micro electro mechanical system (MEMS) technique enabled the fabrication of microelectrode structures as an important precondition for the use of IS under difficult spatial conditions. For the intravascular impedance diagnosis of atherosclerotic plaques, an impedance catheter with the array of 5 annular voxels has been developed and used to detect the impedance of disk-shaped plastic droplets representing fatty lesions in a human iliac artery *in vitro* (Konings *et al.* 1997). For more sensitive electrical characterization of atherosclerotic plaques in vessels, it was considered to use a balloon impedance catheter (BIC) which consists of electrodes integrated with typical balloon catheter (Stiles and Oakley 2003). According to the inflation of balloon catheter, the electrodes contact with intima. Therefore, the impedance measurement of vessels with BIC can avoid the disturbance of intravascular conditions and therefore can be more sensitive and stable. Stiles and Oakley (2003) have designed a BIC with four-point electrode on the surface of balloon and simulated the intravascular impedance of aortas containing different plaque types by using finite element method (FEM). However, the feasibility of BIC for the intravascular impedance measurement of vessels should be validated through the real intravascular experiments which have not been investigated so far. The objective of this thesis is to develop an electrical impedance-based method suitable for the intravascular diagnosis and therapy monitoring of atherosclerosis.

### Goal

Goal of this thesis is to the conception, development, and evaluation of an electrical impedance-based method for the diagnosis and therapy monitoring of atherosclerosis. Therefore, it should be investigated

1. how changes of tissue parameter on the cellular level can affect the measured impedance,
2. whether cellular alteration related to atherosclerosis can be characterized by IS,
3. which side conditions are necessary for a sensitive impedance measurement on vessels walls,
4. whether reproducible impedance measurements can be performed in vessels under *in situ* conditions.

### Working Plan

- To use IS for the diagnosis and therapy monitoring of atherosclerosis, it is required to understand how the changes of tissue parameter on cellular level can be characterized electrically by IS. To investigate basically the influence of cellular alteration on the electrical characteristics of tissues, a single cell model will be used. For the investigation, a micro hole-based system will be used to measure the impedance of cells without the disturbance of electrode polarization resulting in the electrode impedance.
- Adipocytes (fat cells) and disruptions of cell layers are characteristic for atherosclerotic plaques. A precondition to use IS for the diagnosis of plaques and therapy monitoring is that an accumulation of fat cells in tissue and the disruption of cell layer are reflected in the measurable impedance. The effect of an accumulation of fat cells on measured impedance will be investigated by using an adipogenic differentiation model *in vitro*. To investigate how sensitively pathologic disruption processes in cell assemblies can be determined by IS, a virus infection model will be used.
- For a correct interpretation of the impedance data recorded inside a vessel, the various vessel thickness and extra vessel conditions should not influence the measurement results. The influence of the thickness of vessel on the impedance measurement of vessel wall will be investigated by using FEM simulation and a quasi-vessel model. Further, the influence of relative positions of atherosclerotic lipid plaque to electrode array on the measurable impedance will be studied.
- To investigate the feasibility of intravascular characterization of plaques in vessels by IS, a BIC will be manufactured by using a flexible microelectrode array which is integrated with the surface of typical balloon catheter. Using the fabricated BIC, the intravascular impedance of vessels will be measured *in situ* in an atherosclerotic animal model which enables the impedance analysis of vessels in parallel to histological investigation.

### **3 Electrical Characterization of Single Cells**

The electrical impedance of a biological tissue is determined by its structure, cellular composition as well as the structure of its cells. In this chapter, it is investigated how changes on the single cell level are reflected in the measurable electrical impedance. To understand basically how the changes of tissue parameter on cellular level can be characterized by electrical IS, the influence of cellular alteration on the electrical characteristics of tissues is theoretically and experimentally investigated by using a single cell model. A single cell model is used initially to keep the level of complexity as low as possible. For the investigation, a micro hole-based structure is used to measure the impedance on the single cell scale without the disturbance of electrode polarization resulting in the electrode impedance. The cell/micro hole system is also used to investigate whether biological relevant changes can be determined over time by IS with a spatial resolution down to the single cell level.

#### **3.1 Methodology**

##### **3.1.1 Single Cell Model for Theoretical and Experimental Investigations**

For the experimental and theoretical investigations about the influence of tissue parameter on the cellular level on the electrical tissue impedance, a single cell/micro hole arrangement was used (Fig. 3.1). Using this model, the influence of the following parameters on the tissue impedance was investigated:

- cell shape/size,
- cell membrane,
- intra cellular space,
- extra cellular space/tissue transducer interface.

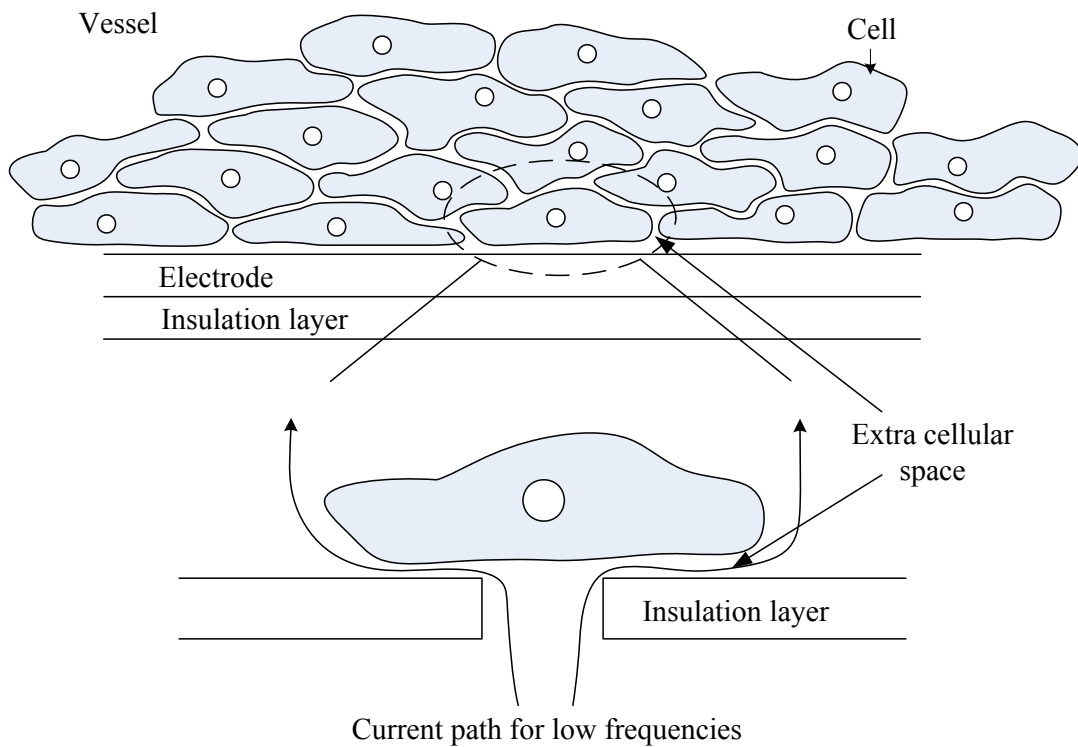


Fig. 3.1: Used single cell model to investigate the influence of cellular parameter on the measured tissue impedance, Upper panel: Schematic of tissue/electrode interface, Lower panel: Single cell model to investigate basically the influence of cellular alteration on the electrical characteristics of tissues on electrodes.

### 3.1.2 Simulation of Electrical Characteristics of a Single Cell/Micro Hole Model

To understand the electrical properties of cell/hole model, FEM simulation was used. From the FEM simulation of single cell on the hole, it was estimated how the behaviour of single cell related to cellular shape and size contributes to the total impedance. For the simulation, the structure of micro hole-based single cell chip was designed as Fig. 3.2. A micro hole with the radius of  $3\ \mu\text{m}$  was positioned in the middle of an insulated layer with the thickness of  $1\ \mu\text{m}$  and the area of  $220\ \mu\text{m} \times 220\ \mu\text{m}$ . In practice, most of animal cells anchor to the surround by using desmosomes and actin filaments. When the cells contact with substrates, they spread and adhere onto the substratum with the gap of several tens to hundreds of nanometers (Giebel *et al.* 1999). The desmosomes, actin filaments, and membrane proteins of cells were not considered. It was assumed that the cell is positioned at the middle of hole, that none part of the cell is inserted into the hole, and that the shape of cell fixed on the hole is a half spheroid. The thickness of cell membrane was  $10\ \text{nm}$ , and the polar radius of half spheroid cell was  $5\ \mu\text{m}$ .

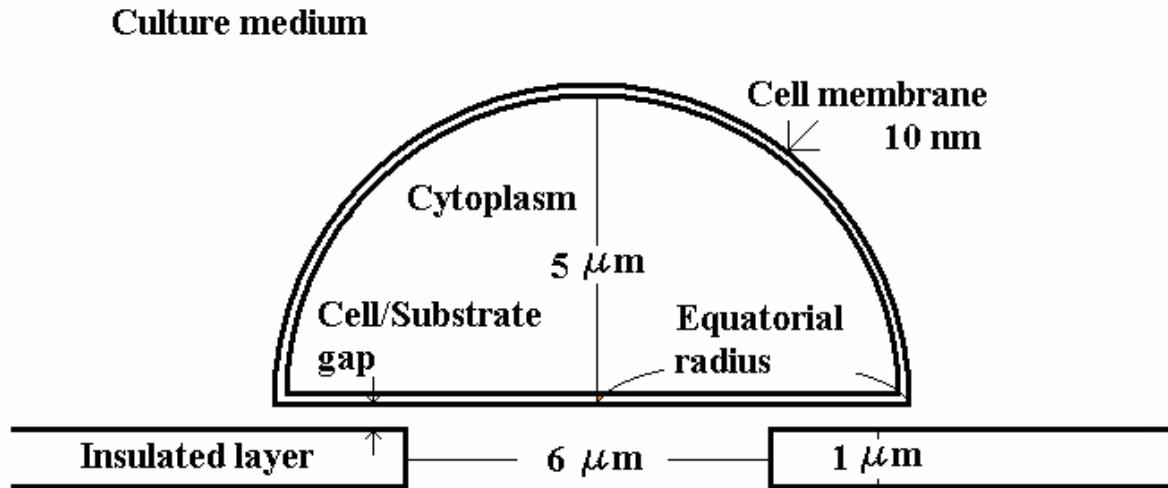


Fig. 3.2: Schematic model of micro hole-based cell chip for FEM simulation (Cho and Thielecke 2007).

The simulation was based on the following assumptions: When electric fields  $\mathbb{E}$  are applied to dielectrics, a current density  $\vec{J}$  is induced as follows (Harrington 1961).

$$\vec{J} = (\sigma + i\omega\epsilon)\mathbb{E} = -(\sigma + i\omega\epsilon)\nabla\phi \quad (\text{eq. 3.1})$$

where  $\sigma$  and  $\epsilon$  are the conductivity and permittivity, respectively,  $i = (-1)^{1/2}$ ,  $\omega = 2\pi f$  with  $f$  the frequency of the electric fields, potential distribution  $\phi$ .

If the cell and cell culture medium are homogenous, source-free region and linear volume dielectric in the electrical frequency range of 100 Hz to 1 MHz, and if the magnetic fields in them are negligible, then the governing equation is:

$$\nabla \cdot \vec{J} = 0 \quad (\text{eq. 3.2})$$

In this frequency range, it was assumed that  $\sigma$  and  $\epsilon$  of cell, cell culture medium and  $\text{Si}_3\text{N}_4$  membrane are isotropic and constant (Tab. 3.1).

The impedance can be obtained by using volume conductor analysis involving the lead field theory and the reciprocal energization of leads (Malmivuo and Plonsey 1995) as follows:

$$Z = \int_V \frac{\vec{J}_1 \cdot \vec{J}_2}{(\sigma + i\omega\epsilon)I^2} dv \quad (\text{eq. 3.3})$$

where  $\vec{J}_1$  is the current density when a current  $I$  flows between the two current electrodes, and  $\vec{J}_2$  the current density when  $I$  flows between the two voltage electrodes.

Tab. 3.1: Conductivity and relative permittivity of materials used for FEM simulation with model of a single cell on a micro hole of Fig. 3.2 (Asami *et al.* 1990, Malmivuo and Plonsey 1995, Elshabini and Barlow 1998, Grimnes and Martinsen 2000).

	Conductivity (S/m)	Relative permittivity
Cytoplasm	0.5	80
Cell membrane	$10^{-8}$	11.3
Cell culture medium	1.6	80
Insulated membrane	$10^{-12}$	5.5

With different cell/substrate gap and equatorial radius of cell, the current density and impedance were simulated in a cylindrical symmetry model by FEM (used program: FlexPDE, PDE solutions, Antioch, USA). When the cell/substrate gap and equatorial radius of cell were 300 nm and 5  $\mu\text{m}$  respectively, a program code for the simulation was shown in Appendix A.

### 3.1.3 Fabrication of Micro Hole Structure for Experimental Investigations

For enabling the experimental investigations on a cell/micro hole model, a micro hole structure was fabricated by semiconductor process technology. A schematic of fabrication process for micro hole-based chip was shown in Fig. 3.3. A silicon wafer (100) with the thickness of 500  $\mu\text{m}$  was prepared, and the both sides of wafer were cleaned. Onto the one side of silicon wafer, a  $\text{Si}_3\text{N}_4$  layer with the thickness of 800 nm was deposited by plasma enhanced chemical vapour deposition (PECVD). By photolithography and reactive ion etching, a micro hole with the radius of 3  $\mu\text{m}$  was patterned in the insulated  $\text{Si}_3\text{N}_4$  layer. Therefore, it was expected that the cells with radius larger than 3  $\mu\text{m}$  are positioned on the hole but not penetrated through the hole by applying the proper level of microfluidics. On the other side of substrate, a  $\text{SiO}_2$  layer was deposited by PECVD. To make a well for the conservation of cell and culture medium, and to connect the well with the hole, the  $\text{SiO}_2$  layer and Si wafer were etched in sequence. For the insulation of well, a  $\text{SiO}_2$  layer with the thickness of 200 nm was deposited onto the substrate. Then, an insulated well and a thin insulated layer with micro hole were fabricated. The thickness and area of the insulated layer were 1  $\mu\text{m}$  and 220  $\mu\text{m}$  x 220  $\mu\text{m}$ , respectively. The contact area of culture medium on the insulated layer and well was about 0.732  $\text{mm}^2$ .

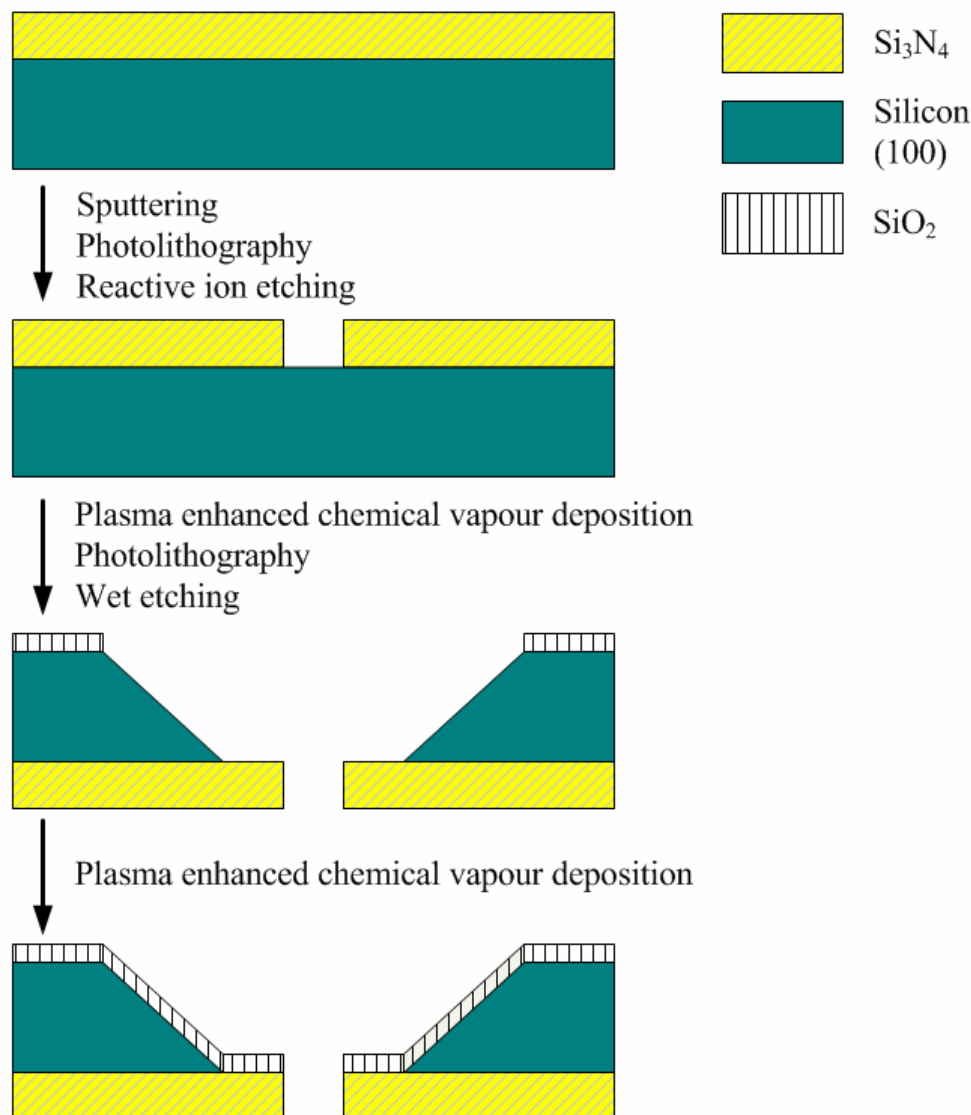


Fig. 3.3: Schematic of procedure for the fabrication of micro hole-based structure by using semiconductor process technology.

### 3.1.4 Experimental Investigation by Using the Single Cell/Micro Hole Model

The experimental setup for impedance measurement of the cell/micro hole model was shown in Fig. 3.4. To avoid the influence of electrode polarization on impedance measurement, the four-electrode arrangement of top and bottom electrode pairs was configured. To control the position of top electrode pair, a micro manipulator was used. The top and bottom electrode pairs were connected to an impedance analyzer Solartron 1260 for impedance measurement (Solartron Analytical, Farnborough, UK). The tips of top electrodes were separated each other about 50  $\mu\text{m}$ , and the bottom electrodes 1 mm. For the positioning of single cell on the micro hole, a micro pump as micro fluidic controller (CellTram, Eppendorf, Wesseling-Berzdorf, Germany) was integrated. For the experiment, L929 cells and a culture medium (RPMI 1640, 10% fetal calf serum (FCS),

0.5% Penicillin/Streptavidin) were prepared. Fig. 3.5 shows the schematic of impedance measurement with micro hole-based cell chip. The radius of L929 cells in the suspension was around 12 to 14  $\mu\text{m}$ . A single L929 cell in the cell culture medium was positioned on the micro hole by using the micro fluidic controller but not sucked into the bottom medium through the hole. After observing the cell state on the hole by microscopy, the impedance was measured by using the impedance analyzer. In the frequency range of 1 Hz to 1 MHz, the current was recorded when the potential for the impedance measurement was kept to 10 mV. Thus, the impedance, the ratio of alternating potential to current, was measured. It was expected that such a low level of potential was required to keep the linear characteristic of voltage to current as a premise of impedance measurement and to avoid the breakdown cell membrane caused by high potential distributed over the membrane. Four groups were divided as follows: when no cells on the hole (No Cell), after the position of a single cell on the hole (0), after the cell cultivation on

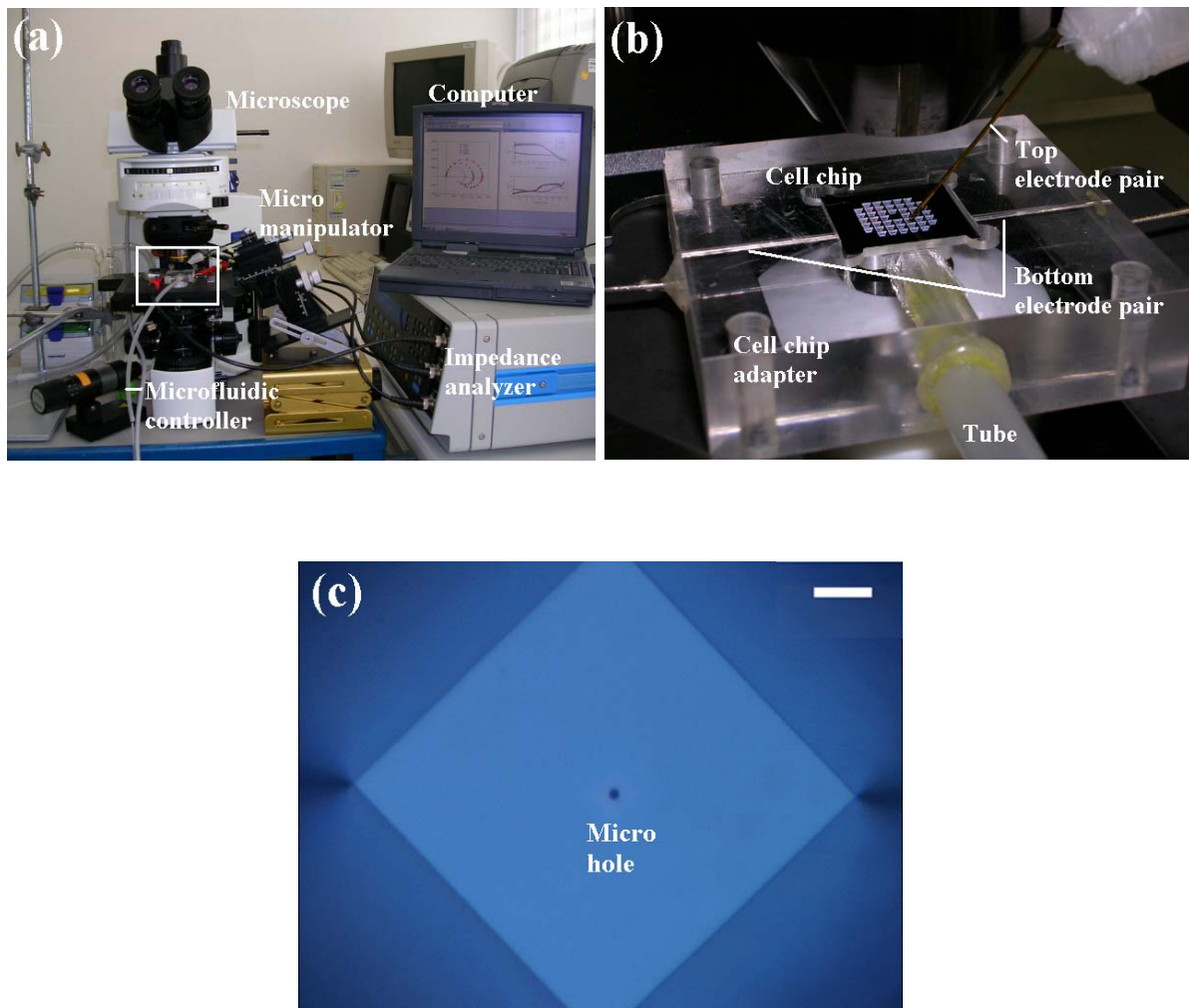


Fig. 3.4: Experimental setup for investigation of the cell/micro hole model (a), micro hole-based chip with 44 wells and chip adapter mounted with microscope and four-electrode arrangement (b), and enlarged photo of one well with a micro hole (radius of 3  $\mu\text{m}$ ) at the center of membrane, scale bar: 30  $\mu\text{m}$ .

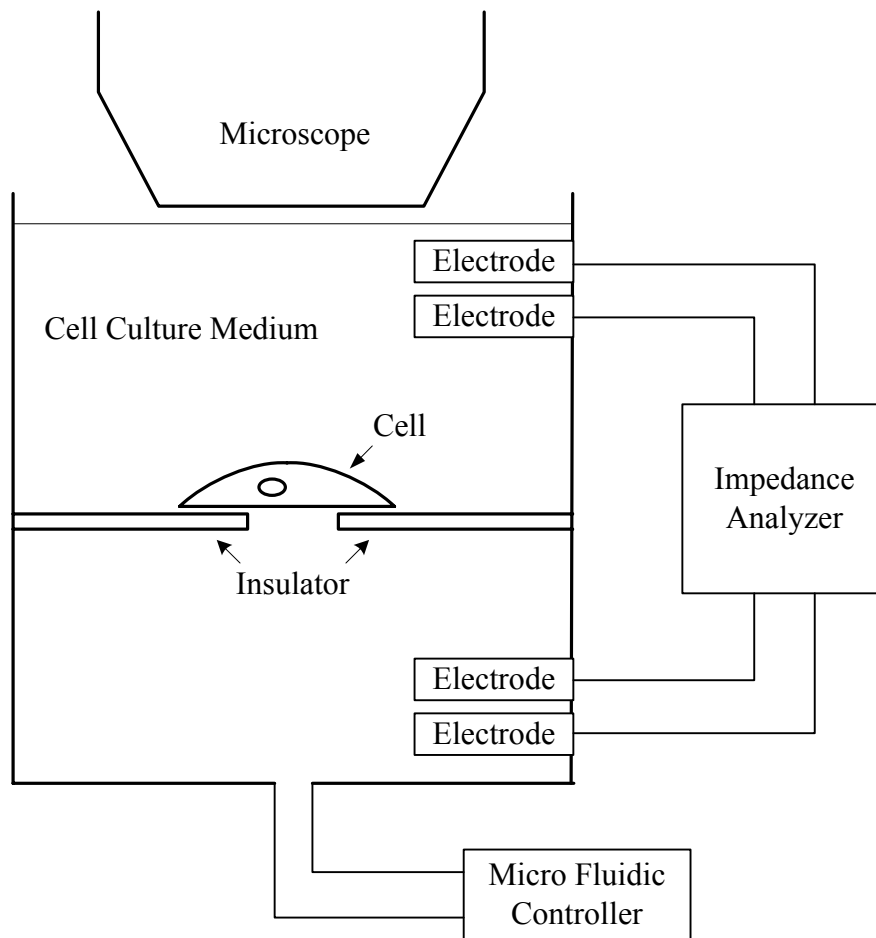


Fig. 3.5: Schematic of impedance measurement on the cell/micro hole model (Cho and Thielecke 2007).

a hole for two days (2 days) or for four days (4 days). Three micro hole-based chips were used in each group. The cell in the micro hole-based chip was cultured in an incubator Heraeus BB6220 (Heraeus-Christ, Hanau, Germany) at 7.5% CO<sub>2</sub> and 37 °C.

To investigate the influence of cell membrane on the impedance behaviour, the cell membrane properties were altered during impedance measurements. To alter the membrane properties, the active substance dimethylsulfoxide (DMSO) which affects the properties of a cell membrane was used (Tokuhiro *et al.* 1974). For the experiments, a cell culture medium containing 5% dimethylsulfoxide (DMSO) was prepared. After the L929 cell on the hole was cultured for two days, the impedance of the cell chip was measured at 1 kHz according to time. During the impedance measurement, only 5 nl of culture medium including 5% DMSO was added in the existed cell culture medium with the total amount of about 243 µl.

## 3.2 Results

### 3.2.1 Simulated Electrical Characteristics of Micro Hole/Cell Model

At the low frequency range ( $< 1$  kHz), the simulated impedance magnitude without cells was  $130 \text{ k}\Omega$ . Fig. 3.6 shows the simulated log-scaled current densities at 1 kHz (Fig. 3.6 (a)) and 1 MHz (Fig. 3.6 (b)) nearby the single cell positioned on one hole (equatorial radius of cell:  $5 \text{ }\mu\text{m}$ , cell/substrate gap:  $150 \text{ nm}$ ). The black and white regions indicate the highest and the lowest value of log-scaled current density, respectively. At the low frequency of 1 kHz, the most of currents were blocked by the  $\text{Si}_3\text{N}_4$  membrane and the cell membrane due to their low conductivity. With increase of frequency, the current penetrating through the intra cellular space and insulated membrane was increased. From the simulation with the model of a single cell on a hole, it was found that the contribution of intra cellular space to the total impedance is  $0.07\%$  at 1 kHz or  $0.3\%$  at 1 MHz.

Fig. 3.7 shows the simulated impedance magnitude of micro hole-based chip with different cell/substrate gap (Fig. 3.7 (a)) or equatorial radius of cell (Fig. 3.7 (b)) versus the log-scaled frequency. The increase of equatorial radius of cell or the decrease of cell/substrate gap caused the increase of impedance magnitude at the low frequency range. However, the decrease of impedance magnitude was appeared when the frequency increases more than several kHz. At frequencies higher than 20 kHz, the impedance was not distinguishable any more for different cell/substrate gaps or diameters of cell. All of the simulated impedance magnitudes were decreased to about  $20 \text{ k}\Omega$  at 100 kHz, and to  $2 \text{ k}\Omega$  at 1 MHz.

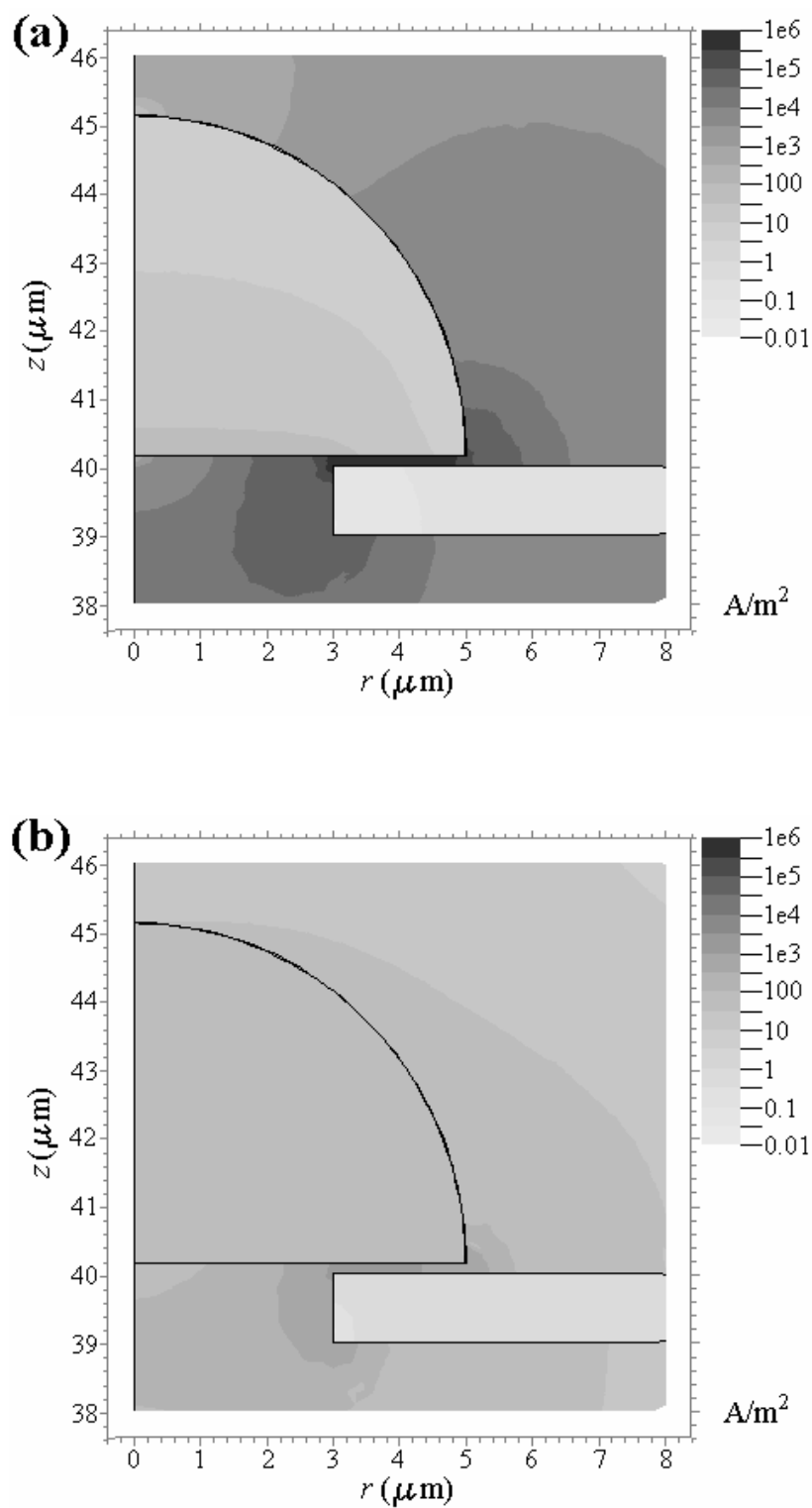


Fig. 3.6: Simulated log-scaled current densities near the single cell on one hole (equatorial radius of cell: 5  $\mu\text{m}$ , cell/substrate gap: 150 nm) at 1 kHz (a) and 1 MHz (b) by FEM.

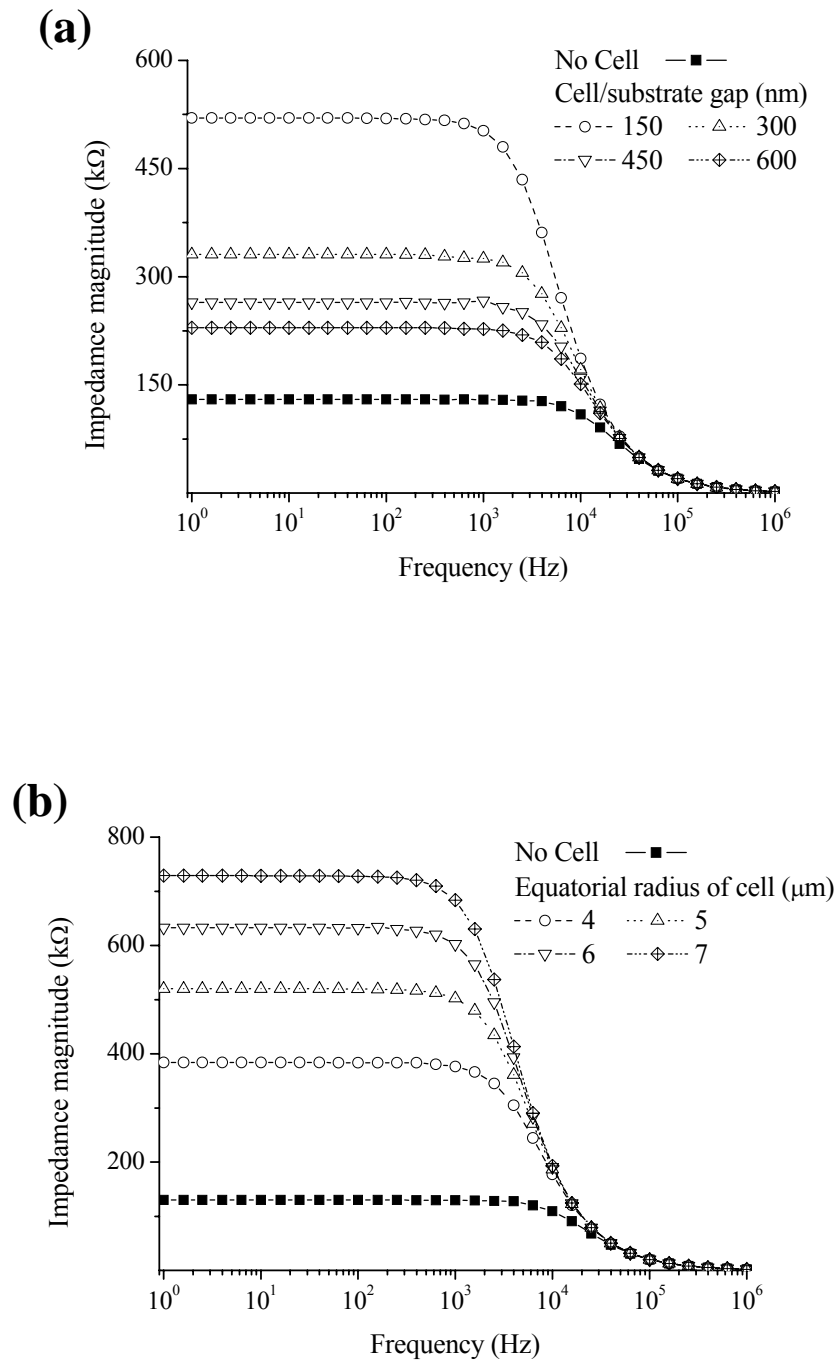


Fig. 3.7: Simulated impedance magnitude with different cell/substrate gap (equatorial radius of cell:  $5 \mu\text{m}$ ) (a) and equatorial radius of cell (cell/substrate gap: 150 nm) (b) vs. log-scaled frequency by FEM (Cho and Thielecke 2007).

### 3.2.2 Measured Impedance of Micro Hole/Cell Model

Measured impedance magnitudes after positioning a single L929 cell ('0') or cultivation of cell ('2 days' or '4 days') were shown in Fig. 3.8 (c). Averages and standard errors of measured impedance magnitudes were indicated as symbols and plus bars, respectively (n for each group = 3). Fig. 3.8 (a) and Fig. 3.8 (b) are pictures after positioning a single L929 cell and after the cell cultivation of 1 day, respectively. The average and standard error of measured impedance magnitudes in case of 'No Cell' were  $135.4 \pm 6.6 \text{ k}\Omega$  at 1 kHz. When the cell was on the hole, the uneven impedance magnitudes were measured in the low frequency range of 1Hz to 10 kHz. In case of '0', '2 days', and '4 days' in Fig. 3.8 (c), the averages and standard errors of impedance magnitudes at 1 kHz were  $207.6 \pm 24.6 \text{ k}\Omega$ ,  $269.0 \pm 66.9 \text{ k}\Omega$  and  $362.5 \pm 37.6 \text{ k}\Omega$ , respectively. The difference of impedance magnitude between the groups could not be measured when the frequency is above about 100 kHz. In case of 'No Cell', '0', '2 days', and '4 days', the averages of measured impedance magnitudes were  $26.1 \text{ k}\Omega$ ,  $26.3 \text{ k}\Omega$ ,  $25.3 \text{ k}\Omega$ , and  $25.4 \text{ k}\Omega$  at 100 kHz, and also  $4.2 \text{ k}\Omega$ ,  $4.4 \text{ k}\Omega$ ,  $4.1 \text{ k}\Omega$ , and  $3.9 \text{ k}\Omega$  at 1 MHz, respectively.

The presents of DMSO in the culture medium affected the impedance of the micro hole/cell model (see Fig. 3.9). Before applying 5 nl of culture medium including 5% DMSO to the cell positioned on a micro hole, the average and standard deviation of impedance magnitude and the phase measured at 1 kHz were  $289.4 \pm 69.3 \text{ k}\Omega$  and  $-9.6 \pm 0.2^\circ$ , respectively. After applying DMSO (5 nl culture medium including 5% DMSO) to the cell chip, the impedance magnitude measured at 1 kHz decreased according to time. On the other hand, the phase measured at 1 kHz increased gradually.

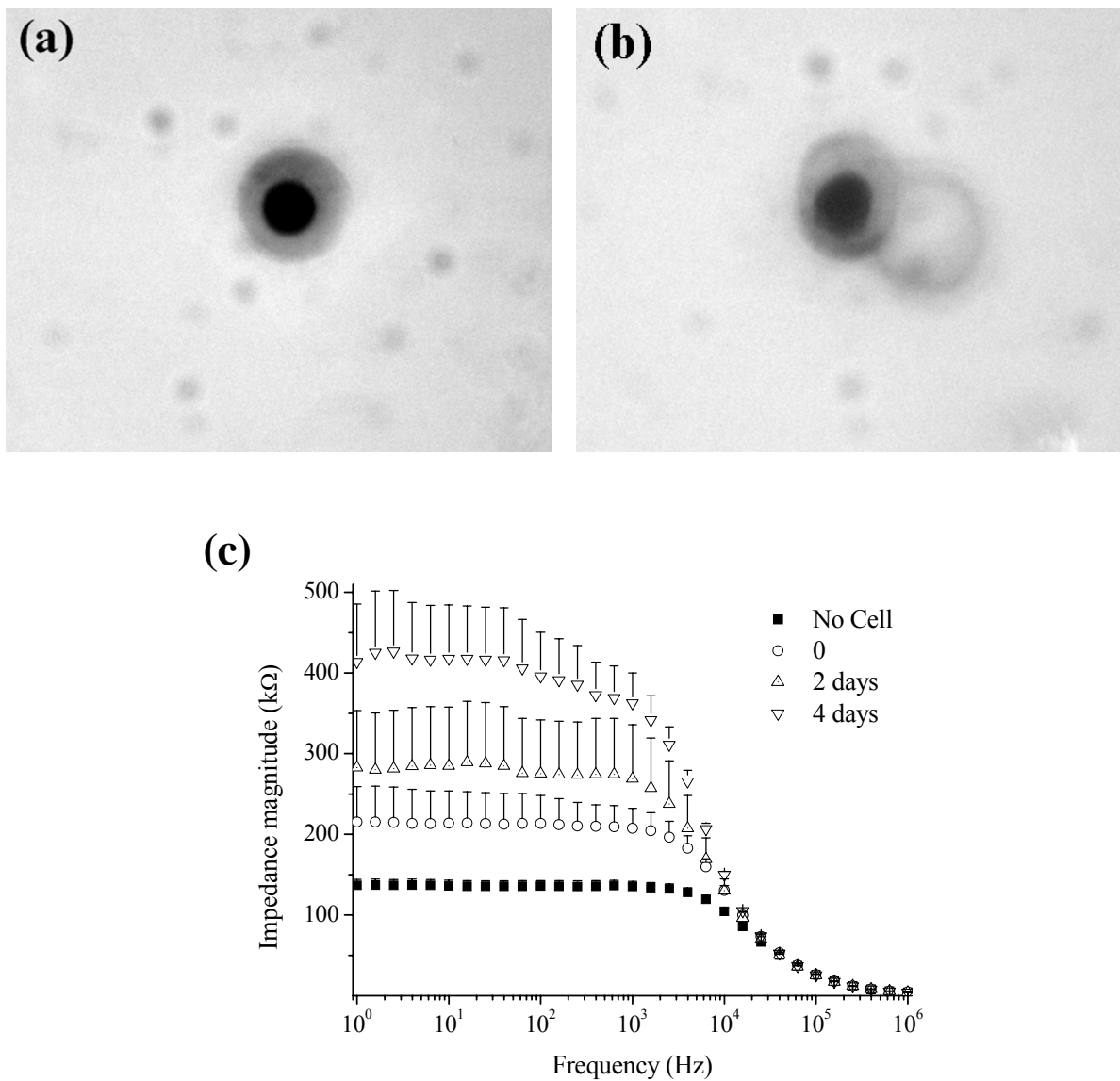


Fig. 3.8: Micrograph after positioning a L929 single cell on the hole (a) and after the cell cultivation for 1 day (b), measured impedance magnitude of the cell culture medium (No Cell), after positioning a single L929 cell on a hole (0), and after the cell cultivation for two (2 days) or four days (4 days) vs. the log-scaled frequency from 1 Hz to 1 MHz (c), potential level: 10 mV, averages and standard errors of each group were indicated as symbols and plus bars, respectively (n for each group = 3) (Cho and Thielecke 2007).

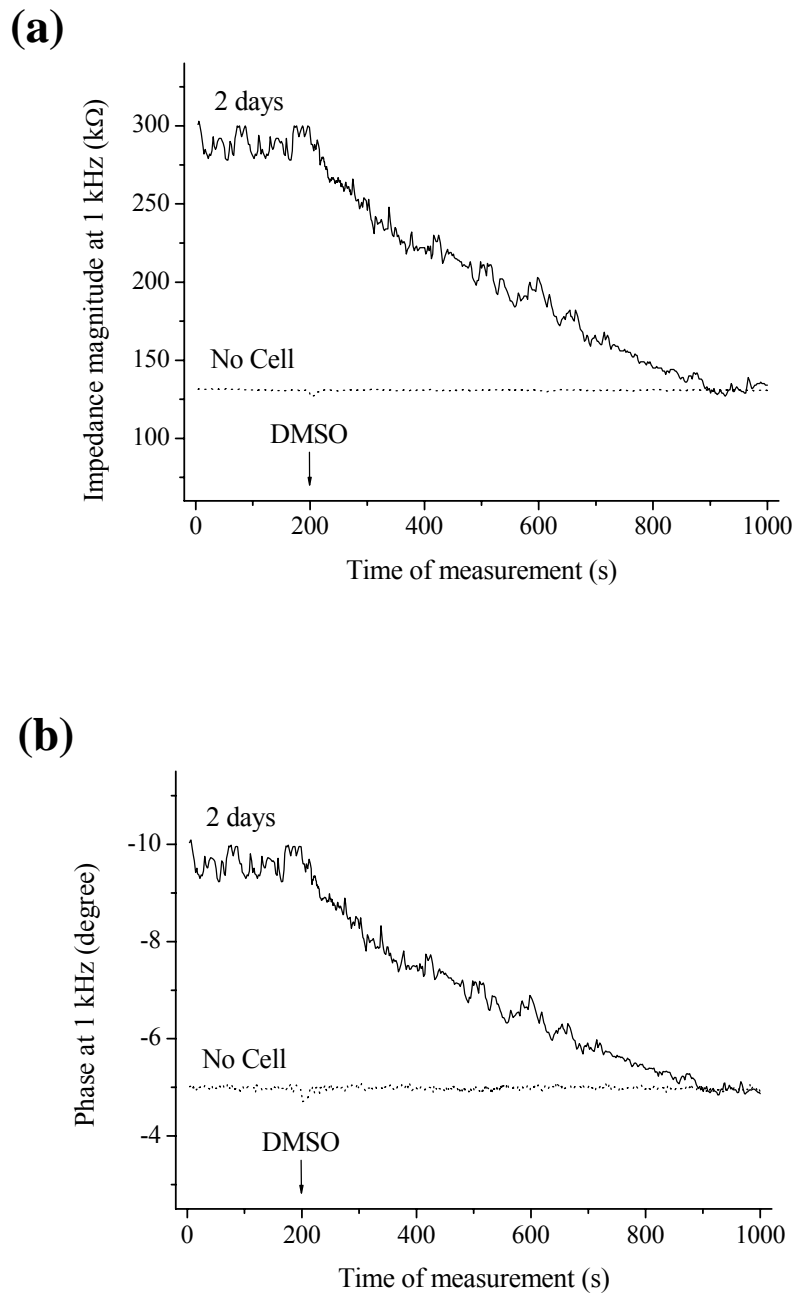


Fig. 3.9: Influence of 5 nl of culture medium including 5% DMSO on L929 cells, impedance monitoring of culture medium (No Cell) and after the cultivation of L929 cell for two days (2 days), impedance magnitude (a) and phase (b) were measured at 1 kHz, DMSO was applied at 200 s (Cho and Thielecke 2007).

### 3.3 Discussion

The theoretical and experimental investigations to understand basically the influence of cellular parameter on the tissue impedance are based on a single cell/micro hole model in this chapter. To investigate the influence of single cell behaviours (e.g. physiological and morphological change of cells, cell/substrate gap) on impedance measurements experimentally, it needs to decrease the size of transducers used for impedance measurement to the size of a cell. Using the single cell/micro hole model, the use of a microelectrode is avoided for impedance measurements on a single cell. The measurement resolution of microelectrode-based impedance measurement is limited by the interfacial electrode impedance increasing with decrease of electrode area (Boer and Osterom 1978). As the interfacial impedance of electrodes increases, the impedance of objects contributes relatively less to the total impedance. Ayliffe *et al.* (1999) have fabricated microelectrodes for the impedance measurement of single cells. However, the microelectrode-based IS was not able to determine the electrical characteristics of single cells accurately due to the complicated electrochemical kinetics of ionic solution and electrical double layer on the surface of microelectrodes. To improve the resolution of impedance measurement of single cells avoiding the disturbance of electrode impedance, a micro hole-based structure is used. When the electric fields are applied over micro holes in an insulated layer, there should be high current density or sensitivity nearby the holes. Further, if the electrodes which have a sufficient large area compared to the area of hole or if four-electrode method is used to apply the electric fields, the total impedance is caused mainly by the hole interface. Thus, the impedance of even single cells contacted on the hole of substratum can be measured without effects of electrode polarization. The mobility of cells on micro holes has been characterized electrically by Hagedorn *et al.* (1995). Although the impedance of single cell/hole has not been exactly analysed on absolute level, Hagedorn *et al.* have shown the possibility of impedance measurement of cells on holes. A single micro hole-based structure has been utilized for quick positioning of a single cell on the hole by using microfluidics (Thielecke *et al.* 1999). Using a micro hole-based chip, the patch clamp and electroporation of single cells has been assessed (Huang and Rubinsky 2001, Huang *et al.* 2003). In this chapter, a micro hole-based chip with the four-electrode method is investigated to characterize the impedance of a single cell on a hole.

#### 3.3.1 Simulated Electrical Characteristics of the Cell/Micro Hole Model

From the simulation with the model of single cell on a hole, it was found that at frequencies below 1 kHz the part of current which flows through the intra-cellular space is small. Due to the low conductivity of cell membrane, the influence of intra-cellular space or organs on the total impedance can be neglected at frequencies below 1 kHz. This means that the impedance measurement of cells/tissues at low frequencies is relatively sensitive to the cellular shape or extra-cellular space in tissues (e.g. conductivity in cell/substrate gap or transducer interface). The simulated impedance spectra of Fig. 3.7 show that the impedance strongly depends on cell/substrate gap and on the equatorial radius of cell on the hole. The cell/substrate gap corresponds in tissues to the extra cellular space and the equatorial radius to the size and shape of cells. When the frequency increased more than several kHz, a high frequency current penetrated through the intra cellular space and also the insulated layer. Since the high frequency current penetrates

through the area of insulated layer not covered by the cell, it is impossible to distinguish the impedance change caused by different cellular shape (equatorial radius of cell) or adhesion (cell/substrate gap) from the total impedance (see Fig. 3.7). The findings about the electrical characteristic of the cell/micro hole model are important for the interpretation of the experimental results.

### 3.3.2 Experimental Setup and Experimental Results

The electrical characteristic of micro hole-based structure was determined by the dimension of hole since the low frequency current was passed through the hole but blocked by the  $\text{Si}_3\text{N}_4$  layer due to its low conductivity. In case of no cells on the micro hole-based chip, the simulated impedance magnitude at 1 kHz (130 k $\Omega$ ) agreed well to the average of measured one without cells (135.4 k $\Omega$ ). When positioning the L929 cell on the micro hole, the suction level was controlled carefully not to damage the cell. A well positioned cell was reflected in an increase of impedance magnitude in the low frequency in comparison to the impedance of a free hole (see Fig. 3.8). The cell positioned onto a micro hole was able to adhere to the surface around hole and the cell could be cultured on the hole over days. During several days of cultivation, the positioned cell proliferated. Impedance measurement on a positioned cell over time showed that the impedance magnitude at low frequencies increased with increase of cultivation period (Fig. 3.8). The increase of impedance over time can be explained by increasing cell adhesion and spreading as well by cell proliferation. Since the conditions regarding cellular shape, adhesion, and arrangement of cell was more similar after positioning the cell than after two or four days of cultivation, the variance of measured impedance was lower after the cell positioning (see Fig. 3.8). If the cellular size and shape are known, the results of FEM simulation for different cell shapes in/on a hole can be used to extrapolate the size of equivalent gap between the cell and substrate from the measured impedance data. In the experiments, however, it is difficult to observe the cell volume or deformability in the hole during the cell positioning. During the aspiration, the spherical shape of suspended cell is deformed and a part of cell is inserted into the hole in dependence on the pressure, surface tension, and viscoelasticity of cell (Cho *et al.* 2008). Therefore, to find exactly the size of equivalent cell/substrate gap, the effect of cell deformation on the impedance measurement should be considered with further optical investigation. Since in tissues the shape of cells can not be determined, it is difficult to distinguish between effects resulting from the cellular shape and effects resulting from the extra-cellular space on the impedance measurement of tissues. The curve of impedance magnitude measured after the cultivation of cell for 4 days decreases from 63 Hz to 1 kHz approximately (see Fig. 3.8). Comparing the measured spectra with the simulated one in Fig. 3.7, it is clear that this unexpected decrease of impedance magnitude from 63 Hz to 1 kHz is not caused by the dielectric  $\text{Si}_3\text{N}_4$  membrane. This phenomenon should be more investigated. At low frequencies, the impedance of cells on the hole was sensitively decreased after applying 5 nl of medium including 5% DMSO (see Fig. 3.9). The used amount of DMSO was too small to affect the environmental condition significantly because the impedance magnitudes measured without cells was almost constant after adding DMSO. However, the change in the properties of cellular membrane caused by such a small amount of DMSO was sensitively reflected in the impedance measurement with micro hole-based cell chip. The results show that the damage of cell membranes can influence the impedance of a tissue.

Furthermore, the results demonstrate that this experimental arrangement has also potential for cell-based biosensors.

By using the fabricated micro hole-based chip, it was possible to measure the impedance on the single cell scale without the disturbance of electrode polarization resulting in the electrode impedance. From the theoretical simulations, it was shown that the passive electrical characteristic of single cells is determined by the cellular shape or cell/substrate gap at the hole interface due to the cell membrane with low conductivity but not by the intra cellular conditions. From the experiments, it was found that the impedance measurement of cells on the hole is strongly determined by the cellular coverage and membrane integrity. Therefore, it is expected that the changes in the corresponding parameters of tissues (e.g. cellular shape, membrane integrity, or extra cellular space) affect the electrical characteristics of tissues and that IS can be used to characterize electrically effects of atherosclerosis related to these parameters. However, real biological tissues are not a distribution of single cells. In biological tissues the cells interact. The interaction of cells can not be represented by a single cell model. To include cell/cell interaction, models based on cell assemblies or tissues are required. In the next chapters, more complex models are used to investigate the suitability of IS for the characterization of cell assemblies and tissues related with atherosclerosis.

### **3.4 Conclusions**

To understand basically how the change of tissue parameter on cellular level can be characterized electrically by IS, the theoretical and experimental investigations of this chapter were based on a single cell/micro hole model. To understand the electrical properties of single cell/micro hole model, the current density and impedance of the micro hole/cell were investigated by FEM simulation. From the simulation, it was found that the impedance of single cell/hole model is dependent on the cellular shape or cell/substrate gap rather than on the intra cellular conditions. The cell/substrate gap of the single cell/hole model corresponds to the extra cellular space of a tissue. For the experiments with a single cell/hole model, a cell was positioned on a hole of a micro fabricated chip. The measured impedance of single cell/micro hole model corresponded to the theoretical investigations. Furthermore, it was investigated by using small concentration of DMSO whether changes of membrane properties are reflected in the measurable impedance. The results indicate that changes in the tissue parameters on the cellular level like cellular shape and membrane integrity affect the electrical characteristics of tissues and that IS can be used to characterize electrically effects of atherosclerosis related to these parameters. However, the interaction of cells can not be modelled with a single cell model. To include cell/cell interaction, models based on cell assemblies or tissues are required. In the next chapters, more complex models are used.

## 4 Monitoring of Cellular Alteration in Cell Assemblies

As described in chapter 3, IS can be used to characterize electrically the tissue parameters on the cellular level such as the cellular shape, membrane integrity, and extra cellular conditions. A precondition to use IS for the diagnosis of plaques and therapy monitoring of atherosclerosis is that an accumulation of fat cells in tissue and the disruption of cell layer which are characteristic for atherosclerotic plaques are reflected in the measurable impedance. In this chapter, the effect of an accumulation of fat cells on measured impedance is investigated basically *in vitro* by using the adipogenic differentiation of stem cells as a model. To investigate how sensitively pathologic degeneration processes in cell assemblies can be determined by IS, a virus infection model is used.

### 4.1 Methodology

#### 4.1.1 Electrode-based Chip and Monitoring System

For the experiments using 2D cell culture models, an experimental setup based on a planar electrode chip was used. Fig. 4.1 shows a schematic of the fabrication procedure of planar electrode-based structure by using semiconductor process technology. First, the insulating silicon nitride layer was deposited on a silicon wafer by plasma enhanced chemical vapour deposition (PECVD). Afterwards, the high conductive platinum electrodes and gold interconnection lines were deposited and patterned on the silicon nitride layer. As an insulation layer, a second silicon nitride layer was deposited on the whole substrate by PECVD. The electrode sites and connecting pads were opened by reactive ion etching. The fabricated electrodes were a 4 x 4 array and separated from each other (distance between the middle of electrodes > 2 mm). All electrodes were circular shape with the radius of 500  $\mu\text{m}$ , and a pair of electrodes in the array was used for the impedance measurement. Therefore, the surface of a pair of electrodes was the active area for the measurement. The electrode substrate was packaged with a ceramic chip carrier. Fig. 4.2 shows the schematic of electric connection between the electrode substrate and the ceramic chip carrier. The terminal pads of electrode substrate were connected with individual conductive lines of chip carrier by wire-bonding. Then, the conductive lines, pads, and wires were insulated by using the silicon resin. A cylindrical glass dish was integrated with the electrode substrate and chip carrier for the conservation of cells and culture medium. The inner diameter and height of the dish was 3 cm and 1 cm, respectively. The fabricated electrode-based chip was shown in Fig. 4.3.

Fig. 4.4 showed the impedance monitoring system with electrode-based chip and the simplified schematic of impedance measurement of cell layer on electrodes. For the impedance measurement of cell layers on electrodes, the fabricated chip were electrically connected to an impedance analyzer Solartron 1260 (Solartron Analytical, Farnborough, UK) by the combination of the chip with chip adapter. By using a multiplexer integrated with the impedance analyzer and by programming of experimental schedules, the impedance monitoring of cell layer on electrodes was controlled during the long-term cultivation. During the cultivation of cell layers on electrodes at 5% CO<sub>2</sub> and 37 °C in an

incubator Heraeus BB 6220 (Heraeus-Christ, Hanau, Germany), the impedance of the cell chip was measured from 100 Hz to 1 MHz by the impedance analyzer. The chosen input potential of 10 mV guaranteed the linear condition premised for IS and avoided the breakdown of cell membrane by over-potential. By recording the responsive current, the impedance, the ratio of alternating potential to current, was measured.

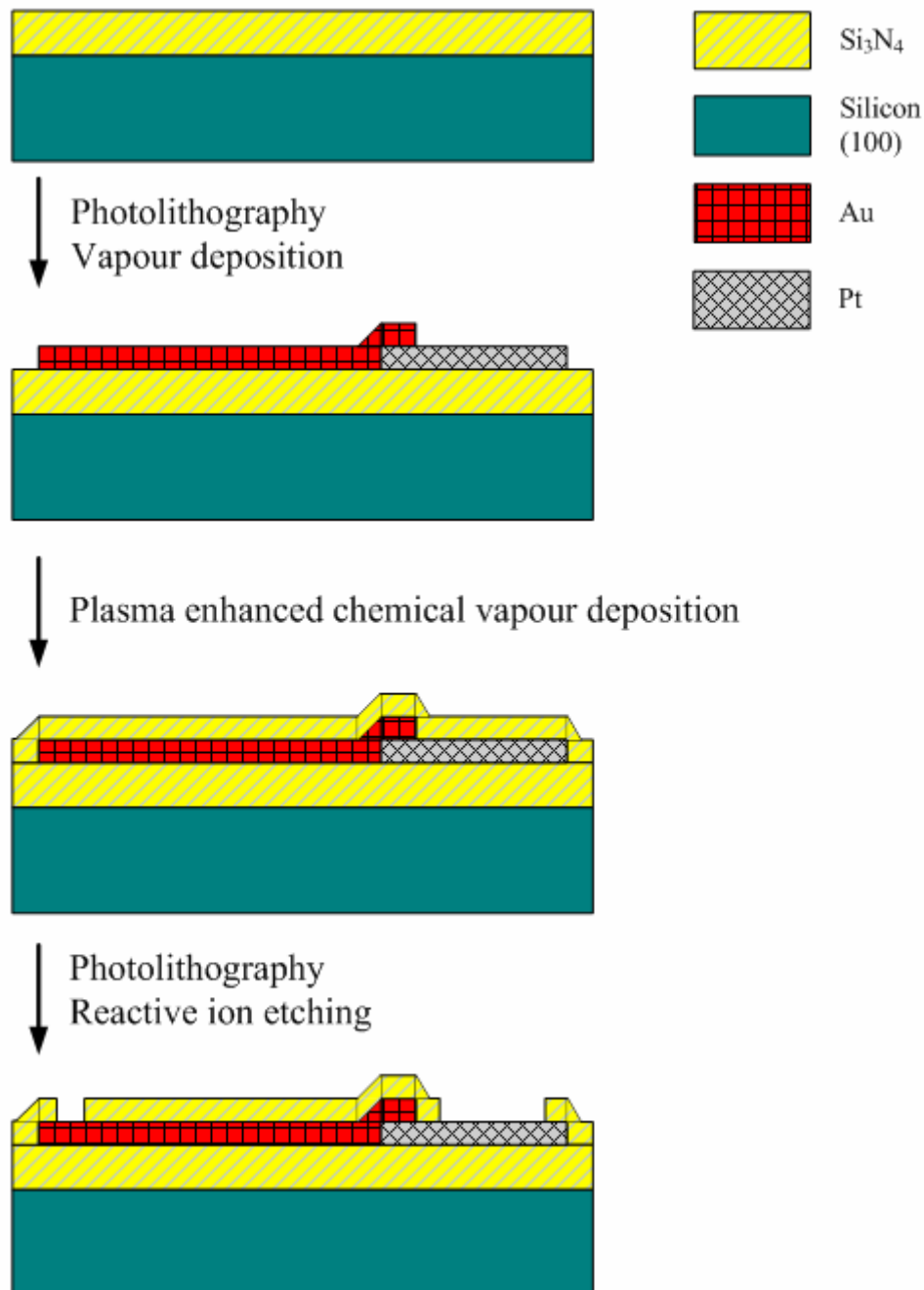


Fig. 4.1: Schematic of procedure for the fabrication of planar electrode-based structure by using semiconductor process technology.

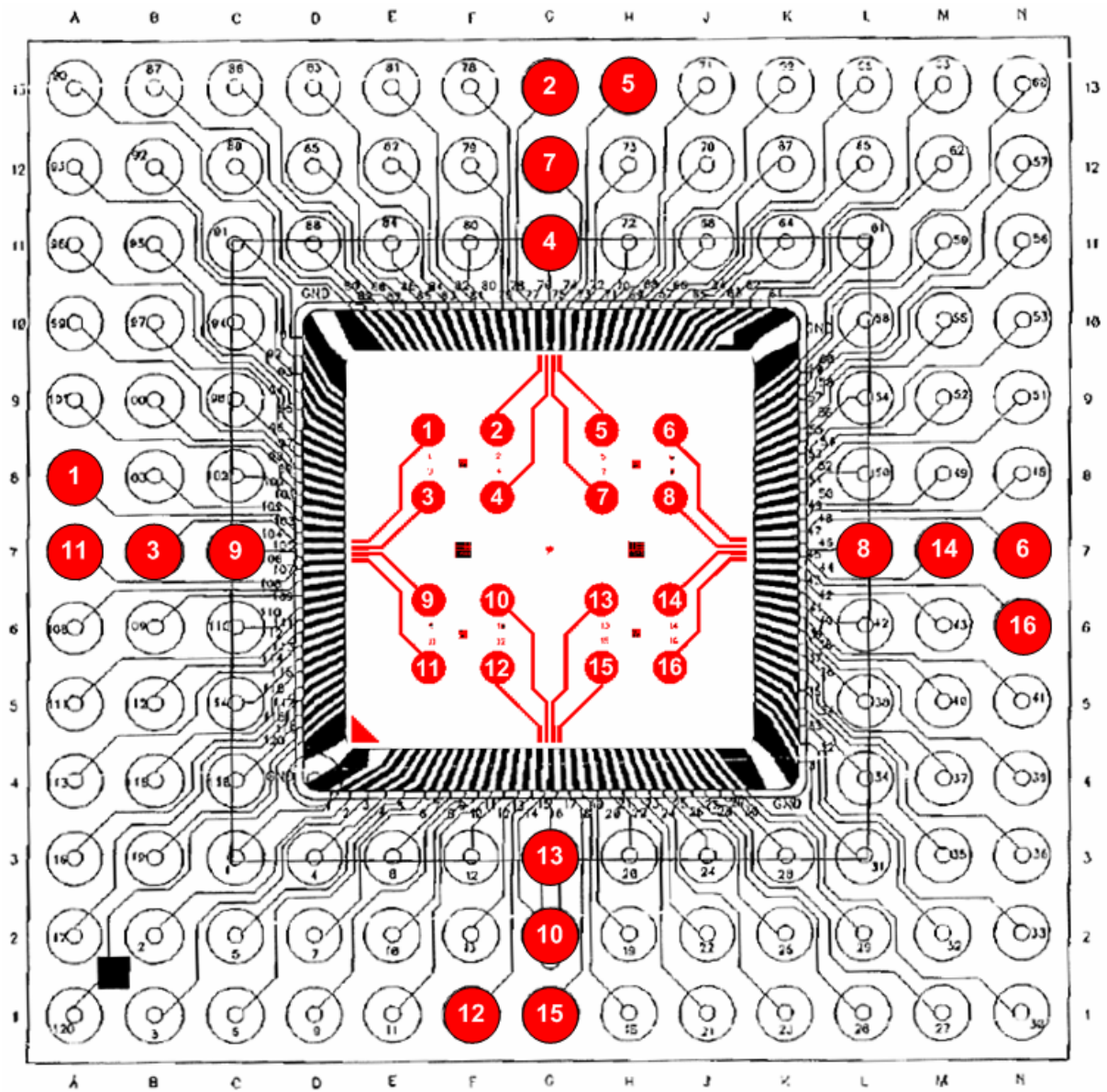


Fig. 4.2: Schematic of electric connection between the electrode substrate with 4 by 4 electrode array (center) and the ceramic chip carrier chip, numbers in painted circles indicate the connected electrode and pin.

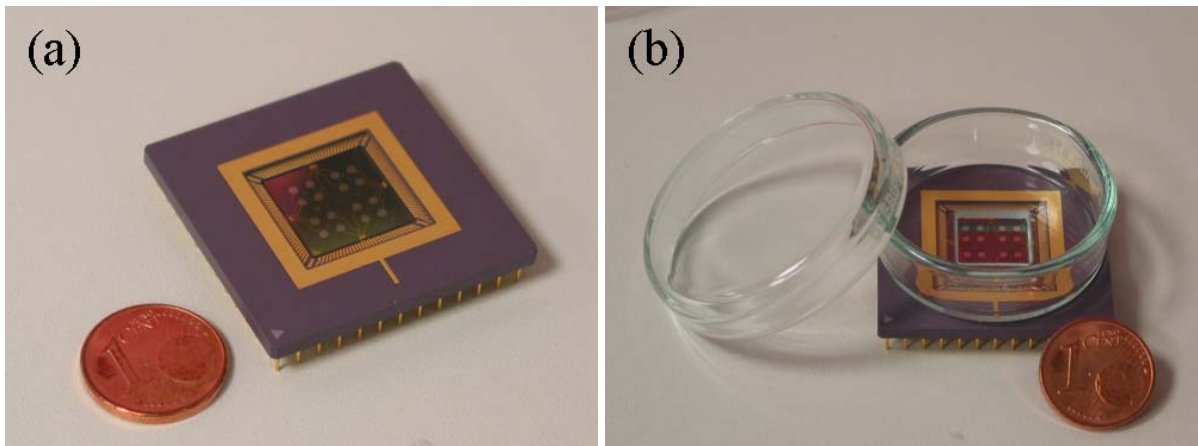


Fig. 4.3: Fabricated 4 by 4 planar electrode array with ceramic chip carrier (a) and the electrode-based chip integrated with a glass dish for the cell cultivation (b).

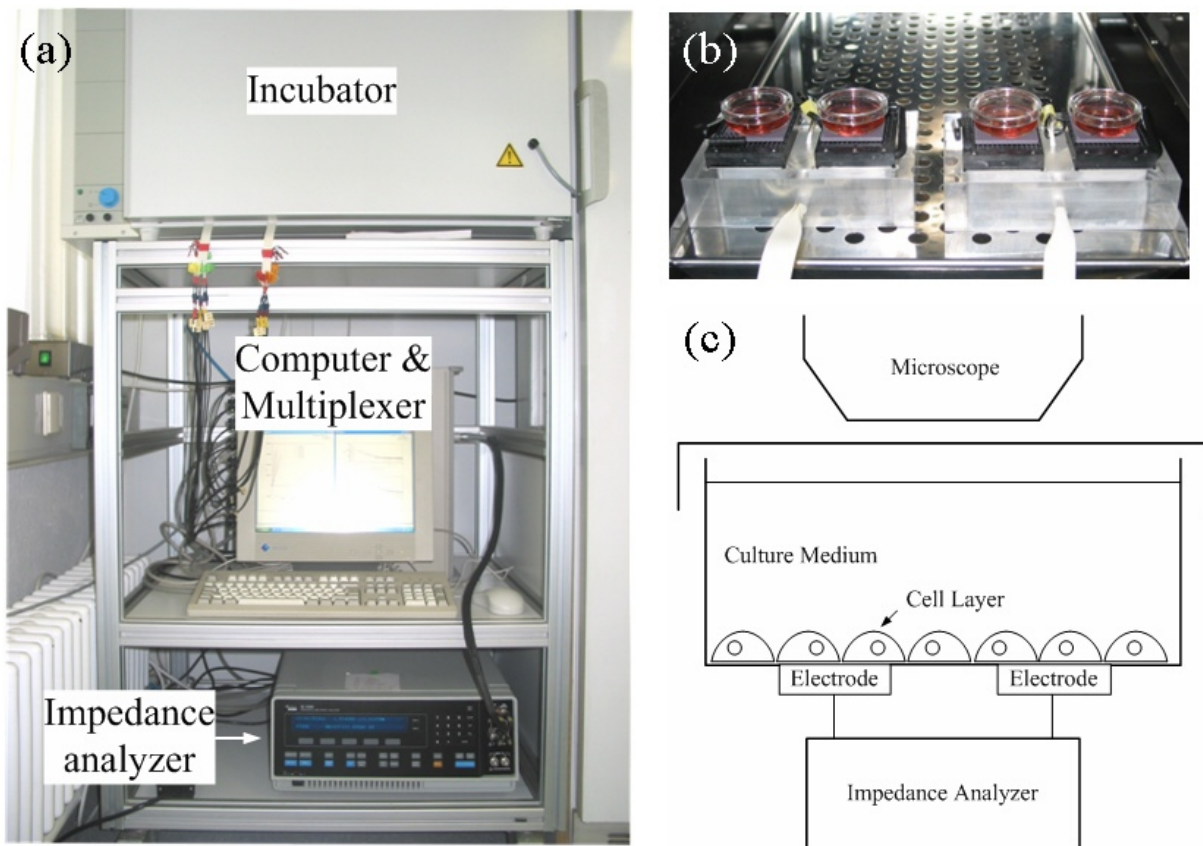


Fig. 4.4: Impedance analyzer with multiplexer for computer controlled impedance measurement of cell layer during the cultivation in an incubator (a), cell chips combined with chip adapter in the incubator (b), simplified schematic of the impedance monitoring system with electrode-based cell chip (c).

#### 4.1.2 Electrical Properties of Cell Layer on Electrodes

To understand how the electrical characteristics of cell layer on electrodes are determined in dependency on the frequency of electric fields, numerical simulation based on FEM was performed. For the design of a cell monolayer model for FEM simulation, it was assumed that the cells shape a cylinder with the radius of  $30\ \mu\text{m}$  and the height of  $5\ \mu\text{m}$  and that the cells with  $10\ \text{nm}$  thickness of membrane are separated with equivalent gaps from the surface ( $h$ ) and neighbored cells ( $g$ ) (Fig. 4.5). The cells spread and adhere onto surroundings with the gap of several tens to hundreds of nanometers (Giebel *et al.* 1999). The electrical properties of cell membrane and cytoplasm were cited from Tab. 3.1. Further, it was assumed that the cell and medium are homogenous, source-free, and linear volume dielectric in the electrical frequency range of  $100\ \text{Hz}$  to  $1\ \text{MHz}$ . If the magnetic fields are negligible, the potential distribution satisfies the generalized Laplace's equation. As described in 3.1.2, the impedance was obtained by (eq. 3.3) derived from volume conductor analysis involving the lead field theory and the reciprocal energization of leads (Malmivuo and Plonsey 1995). The potential distribution and impedance were simulated for equidistant cells on an electrode with radius of  $500\ \mu\text{m}$  in a cylindrical symmetry model by FEM without considering the electrode impedance (used software: FlexPDE, PDE Solutions Inc., Sunol, USA). The parameters  $h$  and  $g$  were varied. When  $h$  and  $g$  were  $100\ \text{nm}$  and  $1\ \mu\text{m}$  respectively, a program code for the simulation was shown in Appendix B.

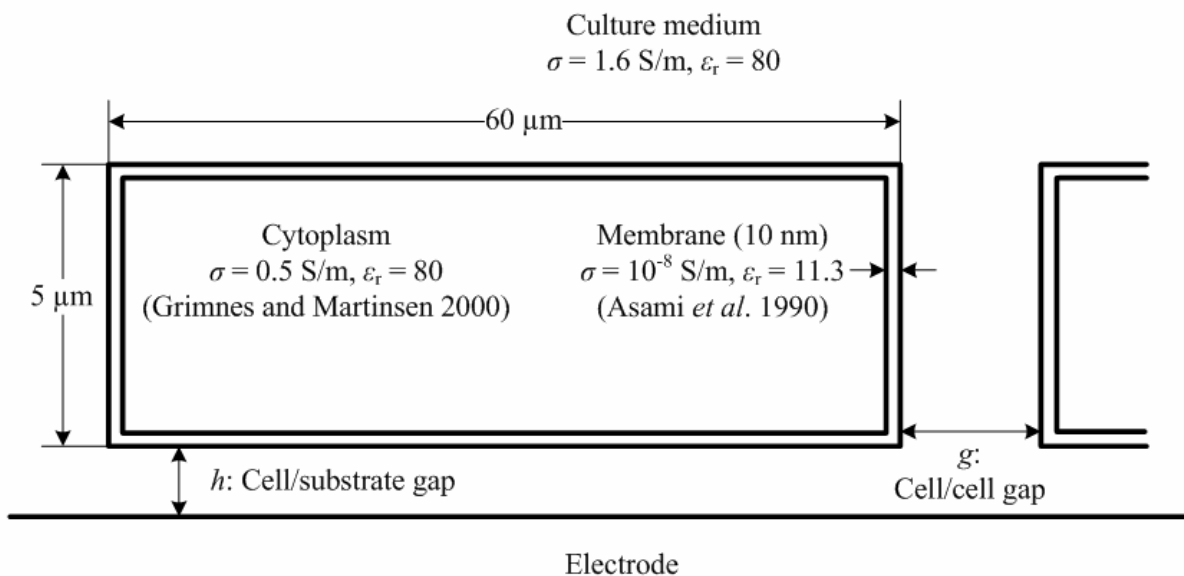


Fig. 4.5: Schematic model of cell monolayer on electrode for FEM simulation (not scaled),  $\sigma$ ,  $\epsilon_r$ : conductivity and dielectric constant, respectively.

### 4.1.3 Monitoring of Disintegration of Cell Layers Caused by an Infection Model with Herpes Simplex Viruses

To investigate whether IS can characterize the disintegration of cell layers, a herpes simplex virus (HSV) infection model in combination with the developed electrode chip-based impedance measurement system (see Fig. 4.4) was used. The HSV infection model was used since HSV is related with the development of atherosclerosis (Key *et al.* 1990). Vero (African green monkey kidney) cells exhibiting a wide spectrum of virus susceptibility were used for the electrical characterization of cell disruption during the infection with HSV. HSV strain was kindly provided by Dr. B. Gärtner, Dept. Virology, University of Saarland. For the experiment,  $8 \times 10^4$  Vero cells with culture medium of 3 ml (Dulbecco's modified eagle medium (D-MEM), 10% foetal bovine serum, 50 units penicillin, 50  $\mu\text{g}/\text{ml}$  streptomycin) were added in the dish of electrode-based chip. Cells were infected with HSV at the different multiplicities of infection (MOI: 0.06, 0.006, or 0.0006). MOI is defined as the average number of viral particles per cell. During HSV infection, the impedance of Vero cells on the electrode was measured as described in 4.1.1.

To interpret the measured impedance of cells by fitting analysis, a mathematical model derived by Giaever and Keese (1991) was used. Giaever and Keese (1991) have derived an analytical solution for the impedance of cell monolayer with an assumption that cells are cylindrical shape with equal radius of  $r_c$  and equal cell/substrate gap  $h$  as Fig. 4.6. For the derivation, it was premised that the low frequency current flows through the cell/substrate or cell/cell gap due to the low conductivity of cell membrane and high frequency current through the cell membrane. Then, Giaever and Keese deduced the

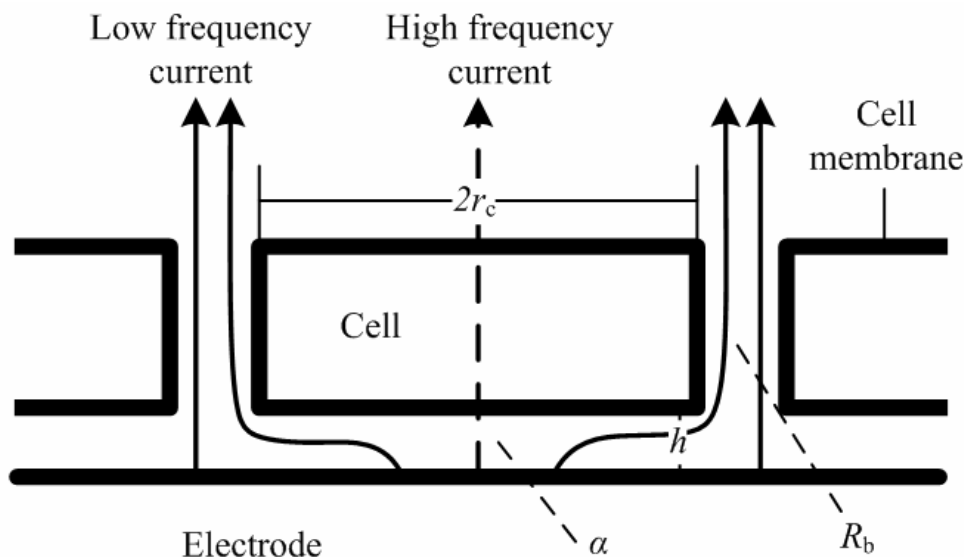


Fig. 4.6: Schematic model of cell monolayer on electrode designed by Giaever and Keese (1991), cells are cylindrical shape with equal radius ( $r_c$ ) and with equal cell/substrate gap ( $h$ ),  $R_b$  and  $\alpha$ : parameters involved with cell/cell and cell/substrate gap, respectively.

whole specific impedance of cells on electrode  $Z_c$  ( $\Omega\text{cm}^2$ ) with parameters involved to the cell/cell ( $R_b$ ) and cell/substrate gap ( $\alpha$ ) as (eq. 4.1). In case of rectangularly shaped cells on electrodes, an analytical solution for whole specific impedance of cell monolayer was derived by Lo and Ferrier (1998). By non-linear curve fitting with the mathematical model of (eq. 4.1), the parameters  $R_b$  with  $\alpha$  in the equation were adjusted to minimize the sum of squared deviations between the model and measured impedance spectra.

$$\frac{1}{Z_c} = \frac{1}{Z_n} \left\{ \frac{Z_n}{Z_m + Z_n} + \frac{\frac{Z_m}{Z_m + Z_n}}{\frac{\gamma r_c}{2} \frac{I_0(\gamma r_c)}{I_1(\gamma r_c)} + R_b \left( \frac{1}{Z_m} + \frac{1}{Z_n} \right)} \right\}, \quad (\text{eq. 4.1})$$

$$\gamma r_c = r_c \sqrt{\frac{\rho}{h} \left( \frac{1}{Z_m} + \frac{1}{Z_n} \right)} = \alpha \sqrt{\frac{1}{Z_m} + \frac{1}{Z_n}}$$

where  $I_0$  and  $I_1$  are modified Bessel function of the first kind of order 0 and 1, respectively,  $Z_n$  and  $Z_m$  the specific impedance of cell-free electrode and cell layer, respectively,  $\rho$  the resistivity of medium,  $R_b$  the junctional specific resistance between adjacent cells over a unit cell area,  $\alpha$  the square root of specific resistance in cell adhesion region.

#### 4.1.4 Characterization of the Accumulation of Fat Cells in Cell Assemblies Using an Adipogenic Stem Cell Differentiation Model

To investigate whether IS can characterize the accumulation of fat cells, which is characteristic for atherosclerotic plaques, an adipogenic differentiation model and the developed electrode chip-based impedance measurement system (see Fig. 4.4) was used. For the experiment, human mesenchymal stem cells (hMSCs) isolated from the bone marrow (femoral head) were used. The hMSCs were cultured with growth medium (84% alpha-modified eagle medium (alpha-MEM), 15% not heat-inactivated FCS, 100 units/ml Penicillin, 100  $\mu\text{g}/\text{ml}$  Streptomycin). The adipogenic differentiation was induced by culturing the hMSCs in differentiation medium (84% alpha-MEM, 15% heat-inactivated FCS, 100 units/ml Penicillin, 100  $\mu\text{g}/\text{ml}$  Streptomycin, 10 nM Dexamethasone, 50  $\mu\text{g}/\text{ml}$  L-ascorbic Acid-2- $\text{PO}_4$ , 500  $\mu\text{g}/\text{ml}$  Isobutyl methylxanthine, 60  $\mu\text{M}$  Indomethacin) (Pittenger *et al.* 1999). The normal or not heat-inactivated FCS included various complements for cell growth such as growth factors, vitamins, amino acids, and so on. By heat inactivation, the complements of FCS were destroyed. The heat-inactivated FCS was used to ensure the adipogenic differentiation of stem cells only with differentiation factors by excluding the effects of various complements on the differentiation. As a control, hMSCs were cultured in medium without differentiation factors (84% alpha-MEM, 15% heat-inactivated FCS, 100 units/ml Penicillin, 100  $\mu\text{g}/\text{ml}$  Streptomycin).

The differentiation of stem cells is relevant for the treatment of atherosclerosis by using cell therapeutical approaches. Therefore, it was also investigated whether various differentiation processes can be determined by IS. To modify the cell differentiation, chlorpyrifos was used. It was reported that the chlorpyrifos affects the adipogenic differentiation by Hoogduijn *et al.* (2006). To monitor the effect of chlorpyrifos on hMSCs

during the differentiation, hMSCs were cultured with differentiation medium and 10  $\mu\text{M}$  chlorpyrifos. The 10  $\mu\text{M}$  chlorpyrifos dissolved in 15  $\mu\text{l}$  methanol was included in an experimental group. In a control group, only 15  $\mu\text{l}$  methanol without chlorpyrifos was applied. Further, the effect of chlorpyrifos on already differentiated adipocytes was studied. The differentiation medium with 10  $\mu\text{M}$  chlorpyrifos was applied once to the cell chip containing the differentiated adipocytes (at day 35 of differentiation). After 3 days from the addition of chlorpyrifos, the medium was recovered to the adipogenic differentiation medium. All mediums in the cell chips were refreshed twice a week. For the electrical characterization of hMSCs during the long-term cultivation or differentiation, the impedance of hMSCs on electrodes was measured as described in 4.1.1.

To interpret the measured impedance of cells by fitting analysis, an equivalent circuit model used by Wegener *et al.* (1996) was used. Wegener *et al.* (1996) represented the impedance of cell layer as a parallel connected resistance ( $R_{cl}$ ) and capacitance ( $C_{cl}$ ) shown in Fig. 4.7. For this model, it was assumed that the electrical properties of cell layer,  $R_{cl}$  and  $C_{cl}$ , are determined by the whole paracellular shunt, cellular adhesion, spreading, and extra cellular matrix. By non-linear curve fitting with the equivalent circuit model of Fig. 4.7, the parameters  $R_{cl}$  and  $C_{cl}$  in the circuit model were adjusted to minimize the sum of squared deviations between the model and measured impedance spectra.

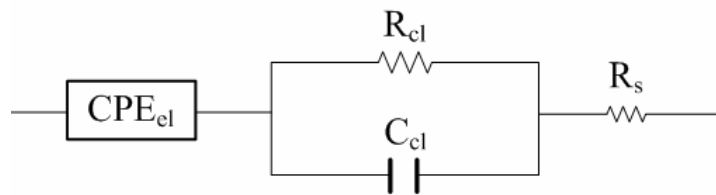


Fig. 4.7: An equivalent circuit for cell on electrodes,  $R_{cl}$  and  $C_{cl}$  are the resistance and the capacitance of cell layer (Wegener *et al.* 1996), respectively,  $CPE_{el}$ : the constant phase element for electrode impedance (Boer and Osterom 1978),  $R_s$ : the resistance of medium.

## 4.2 Results

### 4.2.1 Simulated Electrical Characteristics of Cells on Electrodes

Fig. 4.8 shows the simulated potential distribution near a cylindrically shaped cell on electrode in the model of Fig. 4.5 at 1 kHz (Fig. 4.8 (a)) or 1 MHz (Fig. 4.8 (b)) when the cell/substrate gap ( $h$ ) and cell/cell gap ( $g$ ) are 500 nm and 2  $\mu\text{m}$ , respectively. The black and white regions indicate the highest and the lowest value of potential, respectively. At the low frequency of 1 kHz (Fig. 4.8 (a)), a potential gradient, same as the electric field but with opposite sign, was observed in the cell/substrate gap due to the low conductivity of cell membrane. With the increase of frequency, the potential gradient was found in the intra cellular space as Fig. 4.8 (b).

Fig. 4.9 shows the Nyquist plot of simulated impedance of cell monolayer on the electrode with radius of radius of 500  $\mu\text{m}$  in the model of Fig. 4.5 with respect to different  $h$  (Fig. 4.9 (a)) and  $g$  (Fig. 4.9 (b)). The simulated impedance did not contain both the impedance of electrode and medium over the cells. The decrease of  $h$  or  $g$  caused the increase of resistance at the low frequency range. However, both the resistance and reactance were decreased with increase of frequency and then not distinguished each other with different  $h$  or  $g$  as the frequency was close to 1 MHz. When  $h$  and  $g$  are 100 nm and 1  $\mu\text{m}$  respectively, the contribution of intra cellular space to the impedance magnitude of cell layer was 0.39% at 10 kHz but increased to 25.6% at 1 MHz. At this frequency, all of the simulated impedance magnitude of cell layer was below 38  $\Omega$ .

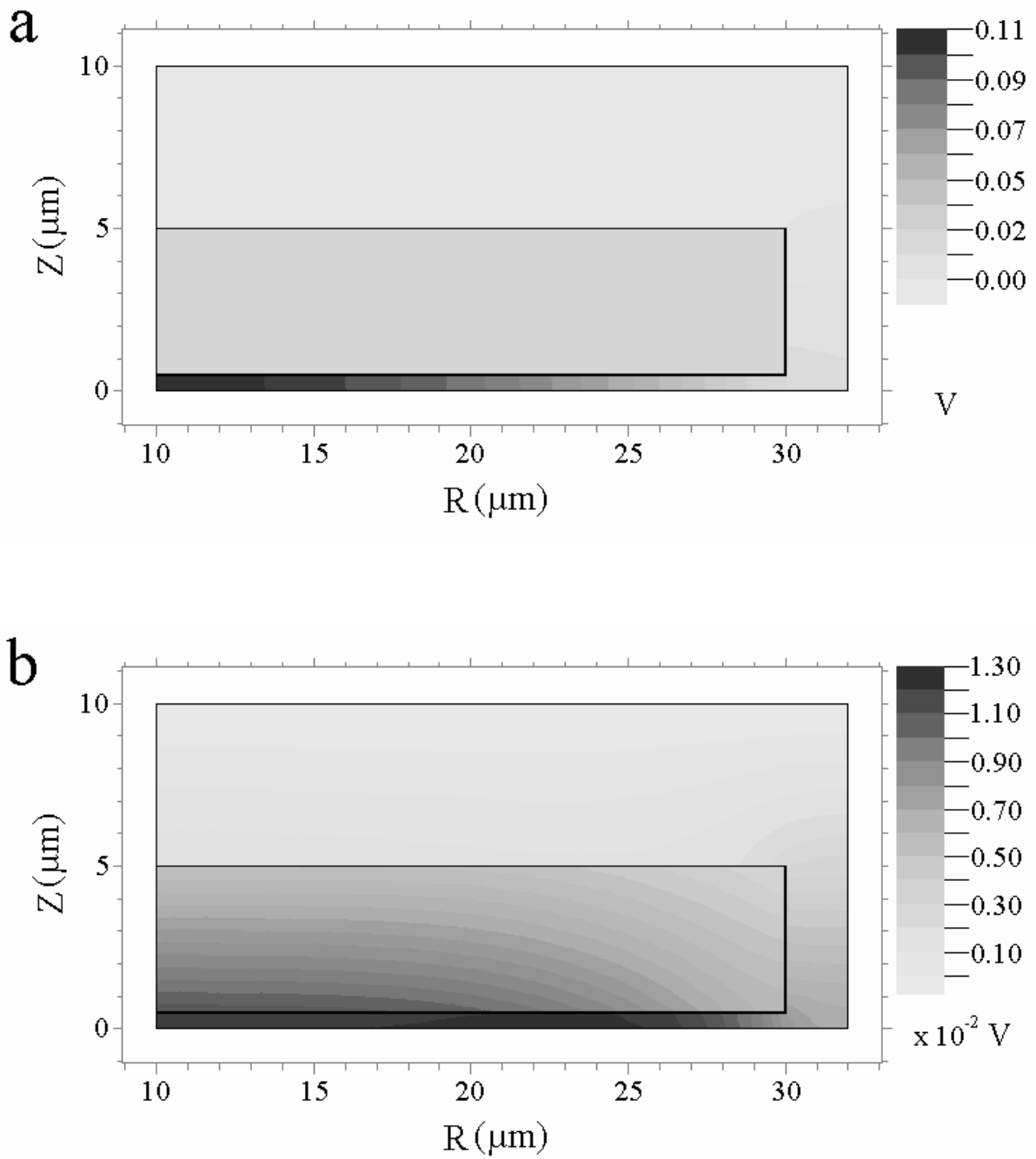


Fig. 4.8: Simulated potential distribution near a cylindrically shaped cell on electrode in the model of Fig. 4.5 with cell/substrate gap ( $h$ ) of 500 nm and cell/cell gap ( $g$ ) of 2  $\mu\text{m}$  at 1 kHz (a) or 1 MHz (b).

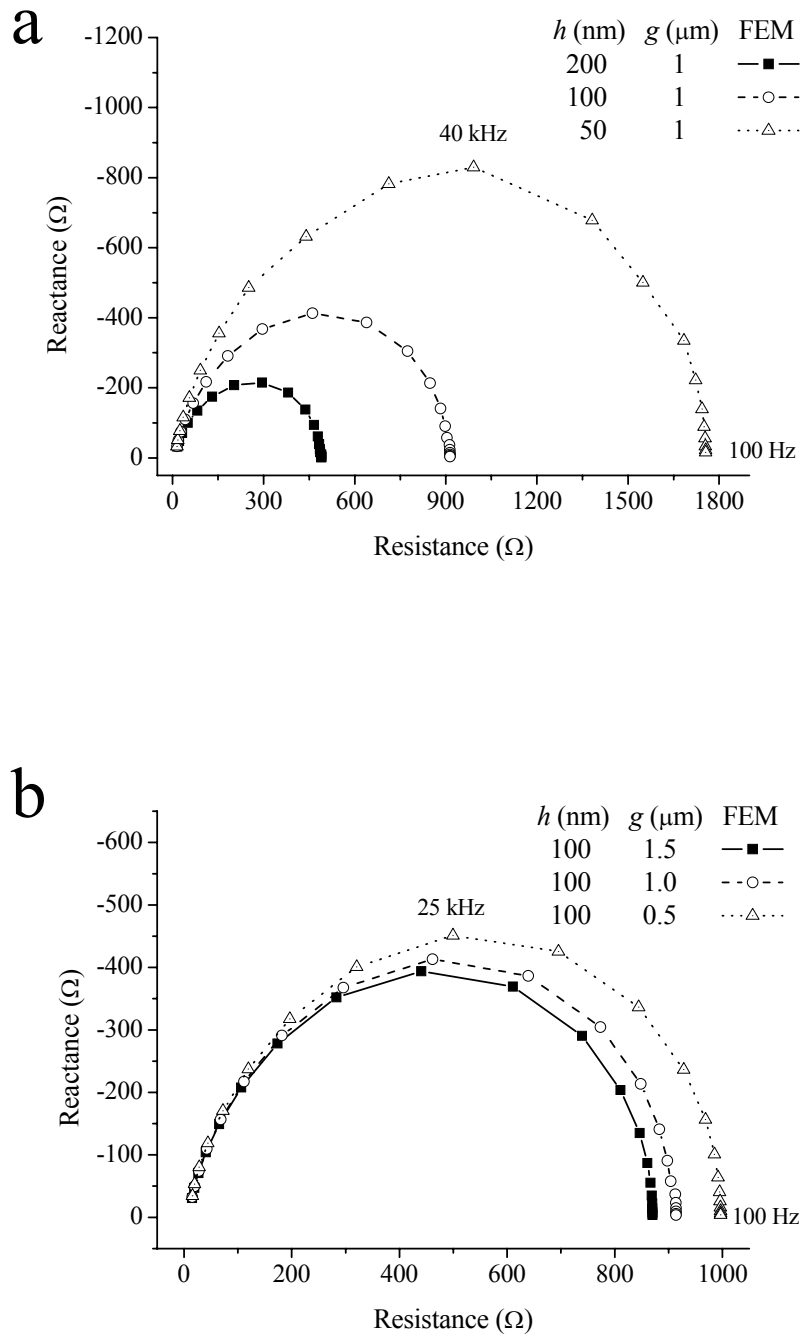


Fig. 4.9: Nyquist plot of simulated impedance (FEM) of cell mono layer on an electrode with radius of  $500\ \mu\text{m}$  in the model of Fig. 4.5 with respect to different cell/substrate gap ( $h$ ) (a) or cell/cell gap ( $g$ ) (b).

#### 4.2.2 Measured Impedance of Cell layer during HSV Infection

During *in vitro* cultivation in the culture dish, Vero cells adhered onto the surface of dish and proliferated. However, the cells infected with HSV showed a typical cytopathic effect finally leading to detachment from the surface which can be visualized by microscopy (see Fig. 4.10). Without the infection, the cells were cultivated on the microfabricated chip unit (see Fig. 4.11 (a)). Morphology of cells cultured on the chip surface was not different in comparison to standard culture dishes. Depending on the time of infection and virus concentration, the shape of infected cells was changed into round, and the infected cells were detached from the electrode (see Fig. 4.11). At 102 h after infection with HSV, the partially exposed electrode area caused by the detachment of cells was clearly observed by microscopy at the MOI of 0.06 and 0.006 but not at the MOI of 0.0006. The partially exposed electrode areas were indicated by arrows in Fig. 4.11 (c and d).

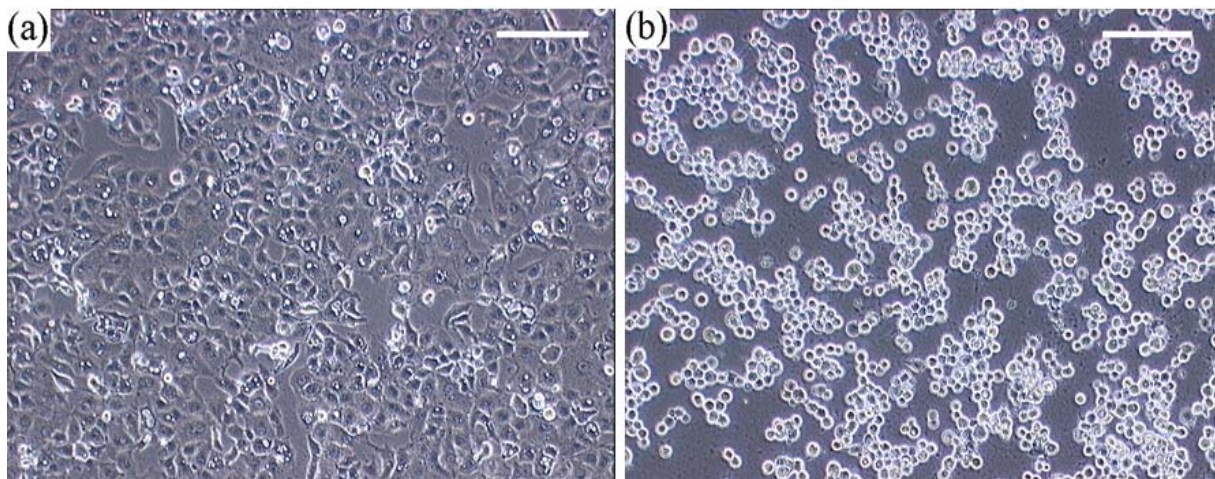


Fig. 4.10: Vero cells adhered onto the culture dish (a) and the detachment of cells infected with HSV (b), scale bar: 200  $\mu\text{m}$  (Cho *et al.* 2007).

The measured impedance spectra of cell chip and fitting lines were shown in Fig. 4.12. For frequencies higher than 300 Hz, the impedance magnitude recorded on electrodes with cells was increased in comparison to impedance magnitude recorded on electrodes without cells. At 4 kHz, the difference between the values of 'Vero cultured for 68 h' and 'No Cell' was 4.44 k $\Omega$ , and the fitted model parameters  $R_b$  and  $\alpha$  of of (eq. 4.1) were 13.55  $\Omega\text{cm}^2$  and 7.24  $\Omega^{0.5}\text{cm}$ , respectively. For cells without infection the parameter  $R_b$  increased almost linearly until a cultivation time of 52 h, then  $R_b$  decreased until the change of culture medium (see Fig. 4.13 (a)). After the first exchange of culture medium,  $R_b$  immediately increased and then decreased again with the time of cultivation. In all cases of cells infected with HSV, the curves of  $R_b$  were clearly different from those of controls for cultivation time higher than 100 h even at the MOI of 0.0006 (see Fig. 4.13).

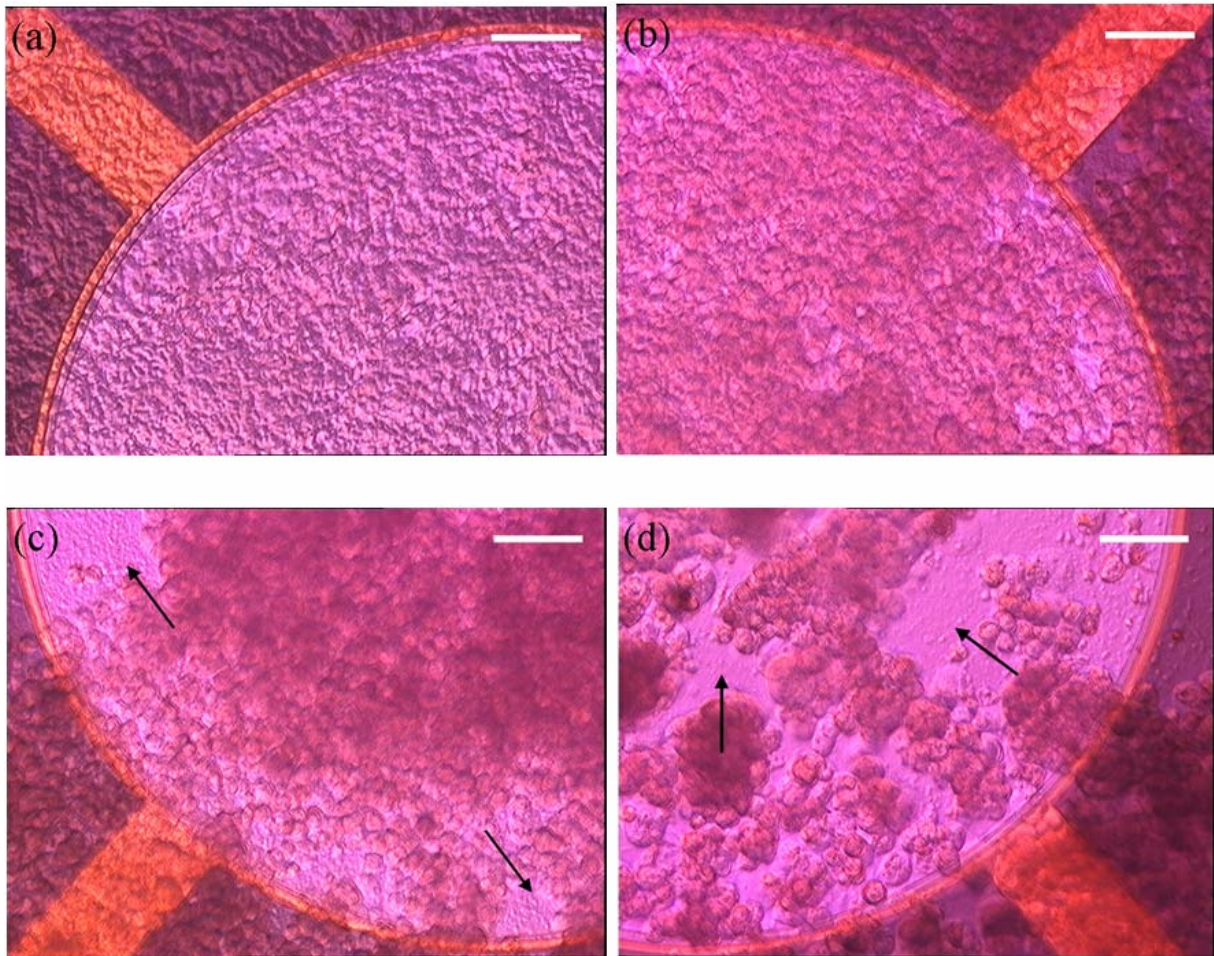


Fig. 4.11: Vero cells not infected (a) and infected with HSV for 102 h at the MOI of 0.0006 (b), 0.006 (c), or 0.06 (d) on the platinum electrode with a radius of 500  $\mu\text{m}$ , arrows indicate the partially exposed electrode area caused by the detachment of infected cells, scale bar: 100  $\mu\text{m}$  (Cho *et al.* 2007).

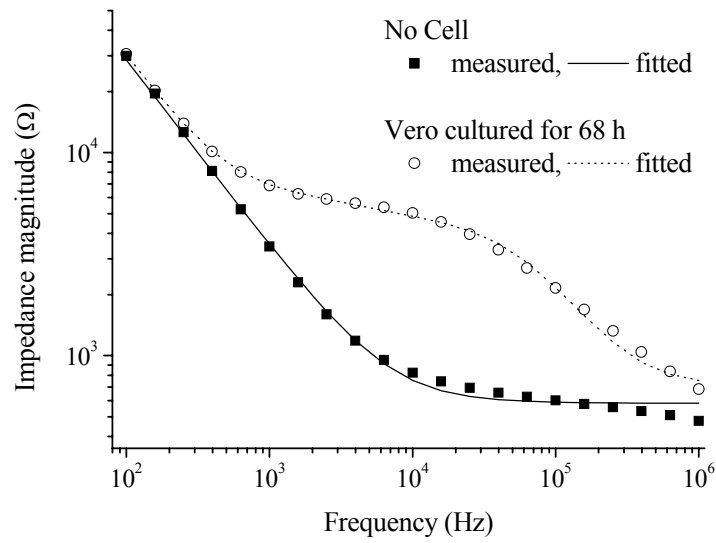


Fig. 4.12: Measured and fitted impedance spectra without cells (No Cell) and with Vero cells cultured for 68 h, in 'Vero cultured for 68 h', the fitted parameters  $R_b$  and  $\alpha$  of (eq. 4.1) were  $13.55 \Omega\text{cm}^2$  and  $7.24 \Omega^{0.5}\text{cm}$ , respectively (Cho *et al.* 2007).

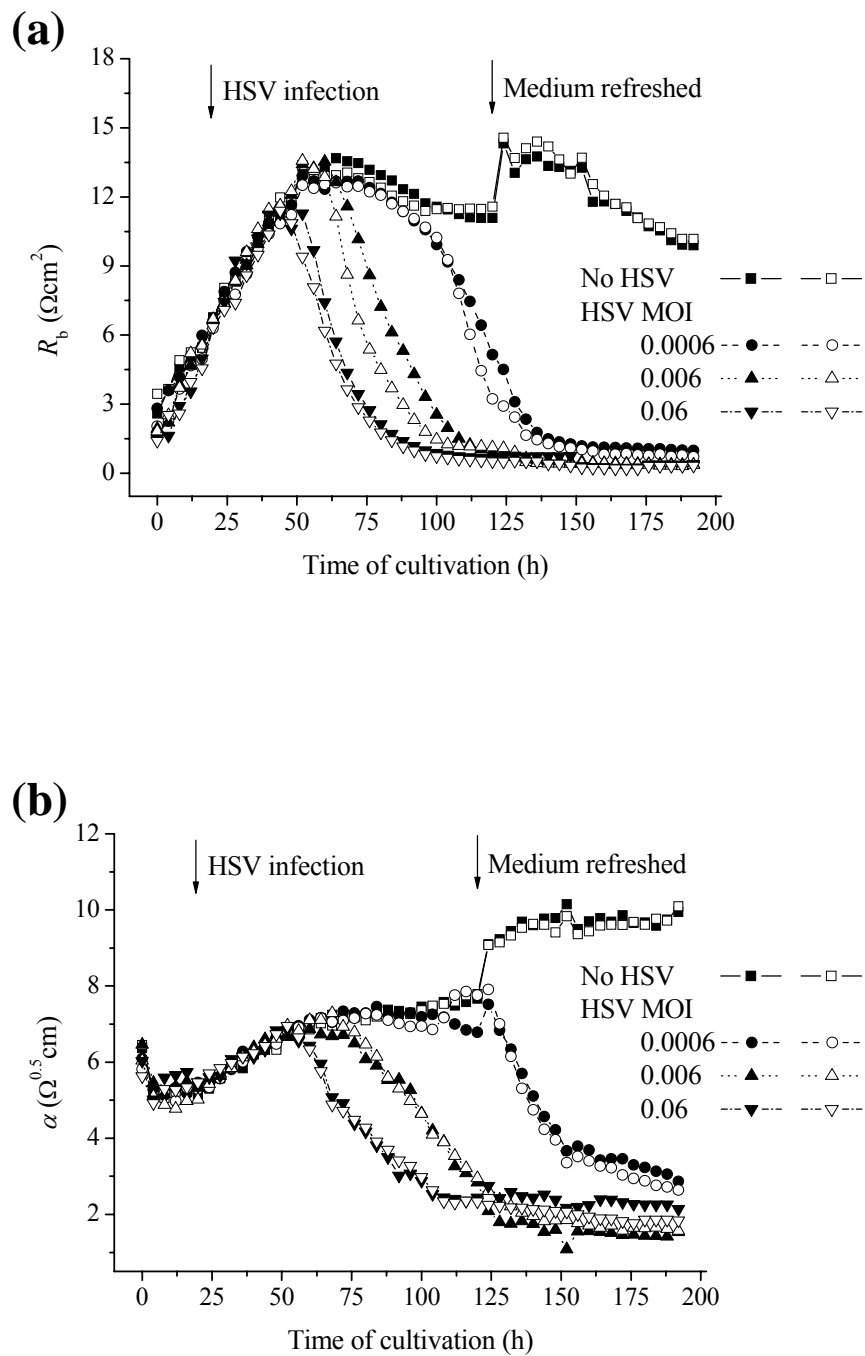


Fig. 4.13: Monitoring of  $R_b$  (a) and  $\alpha$  (b) of Vero cells during the cultivation or infection with HSV at the MOI of 0.0006, 0.006, or 0.06 (Cho *et al.* 2007).

### 4.2.3 Measured Impedance of Differentiated hMSCs

Human mesenchymal stem cells (hMSCs) adhered and spread on the planar electrodes of the fabricated chip during cultivation (Fig. 4.14). The impedance magnitudes of impedance spectra recorded on electrodes with cells after a cultivation of 460 h were clearly higher in comparison to control measurements without cells (Fig. 4.15 (a)). The parameters of the equivalent circuit model of Fig. 4.7 were determined from the recorded impedance data of electrodes covered with cells. The model parameter  $R_{cl}$  increased and the parameter  $C_{cl}$  decreased until the 420 h of cultivation time. Afterwards, the values for  $R_{cl}$  fluctuated between 1410  $\Omega$  and 1670  $\Omega$ . At 460 h of cultivation time, the value for  $R_{cl}$  was  $1556 \pm 52 \Omega$  and the value for  $C_{cl}$  was  $1.24 \pm 0.04$  nF (Fig. 4.15 (b)).

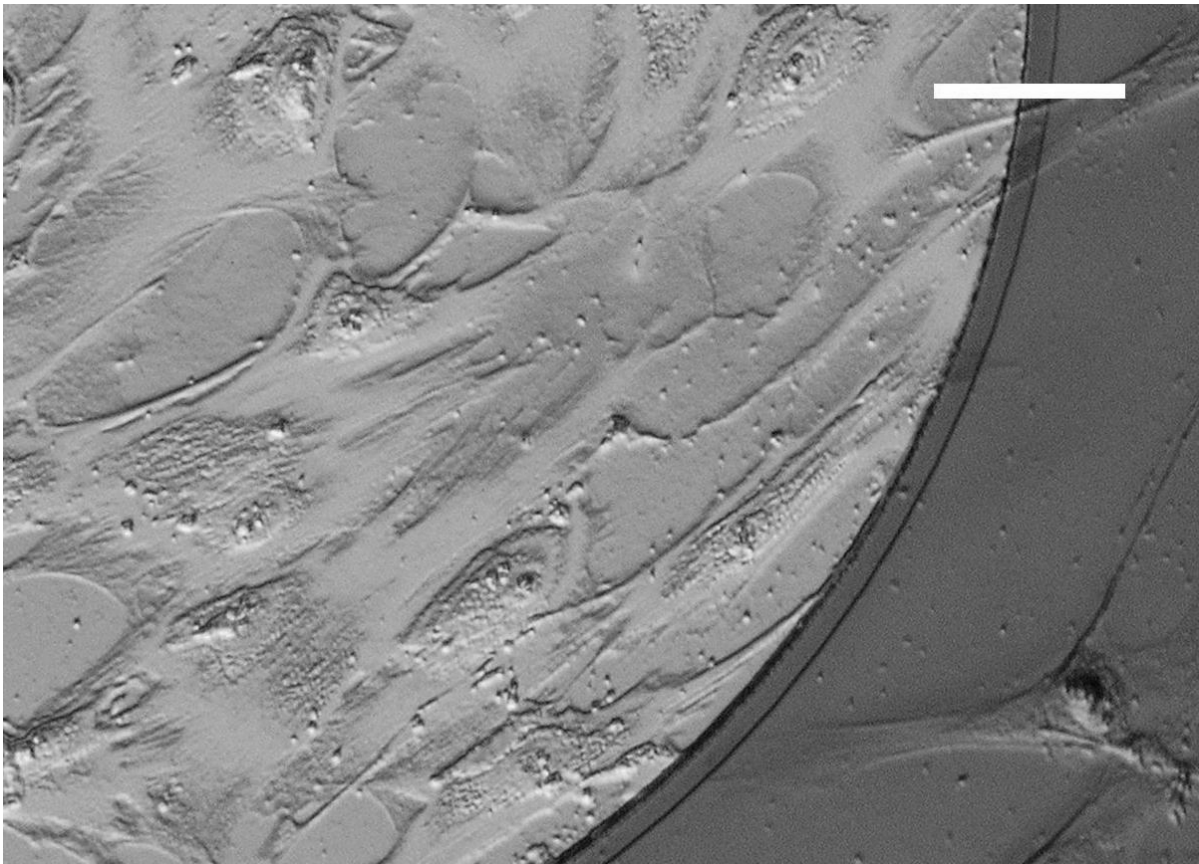


Fig. 4.14: Micrograph of human mesenchymal stem cells adhered on the fabricated circular electrode-based chip during the cultivation, scale bar: 60  $\mu\text{m}$ .

At day 13 of adipogenic differentiation, the fat vacuoles were clearly observed after staining the fat with triglyceride (Fig. 4.16). Further, the hMSCs cultured in the electrode-based chip were differentiated into adipogenic direction and the impedance of hMSCs at day 29 and 39 of adipogenic differentiation was measured (Fig. 4.17). The determined impedance data, represented by the model parameter  $R_{cl}$  and  $C_{cl}$ , of the differentiated cells were different from those of undifferentiated cells (Fig. 4.17 (a)). The averages and standard errors of  $R_{cl}$  and  $C_{cl}$  for differentiated hMSCs to adipocytes and the control were presented as symbols and bar, respectively ( $n$  for each group = 6). While the

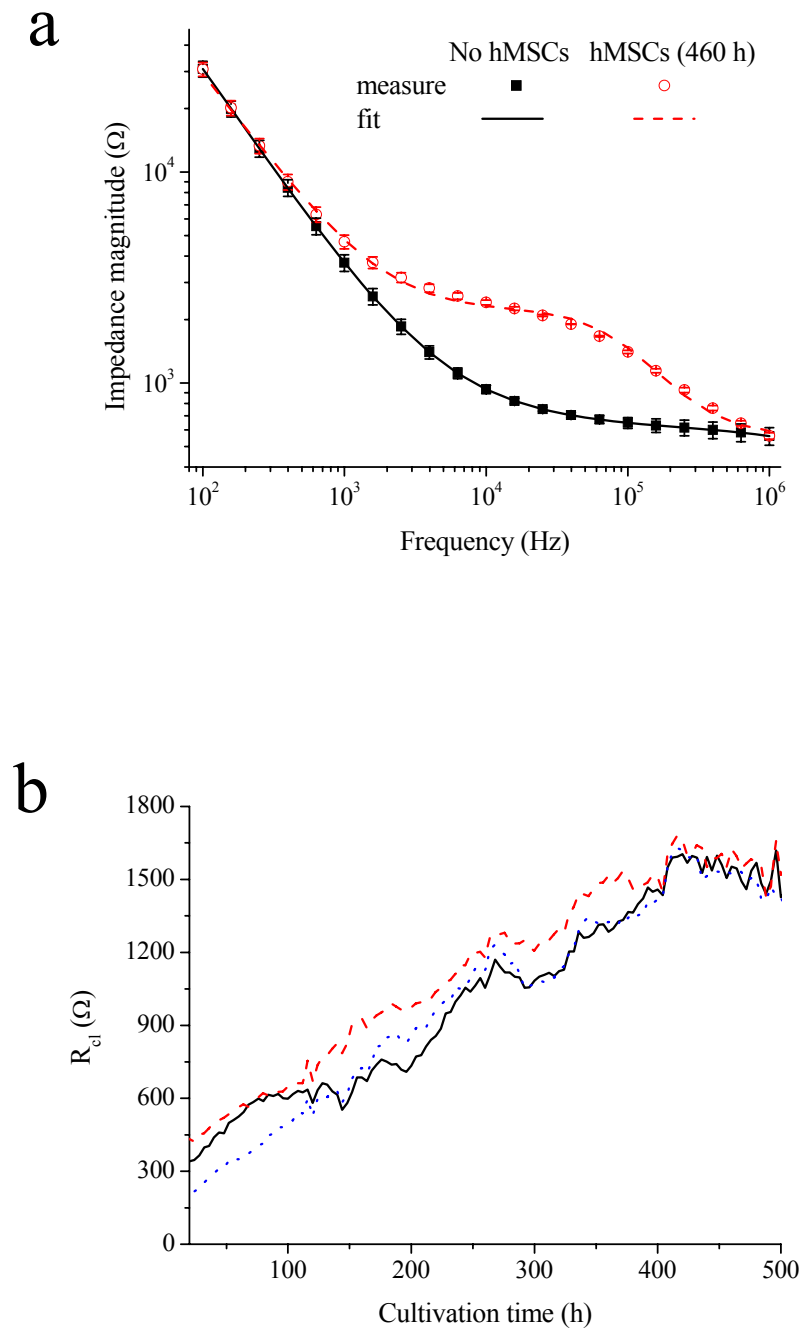


Fig. 4.15: Average and standard deviation of measured impedance magnitude (measure) over the frequency for electrodes without or with hMSCs cultured for 460 h (n for each group = 3) and fitted graph (fit): for fitting, the equivalent circuit of Fig. 4.7 was used (a), monitoring of model parameter  $R_{ei}$  during the growth of hMSCs on planar electrodes (b).

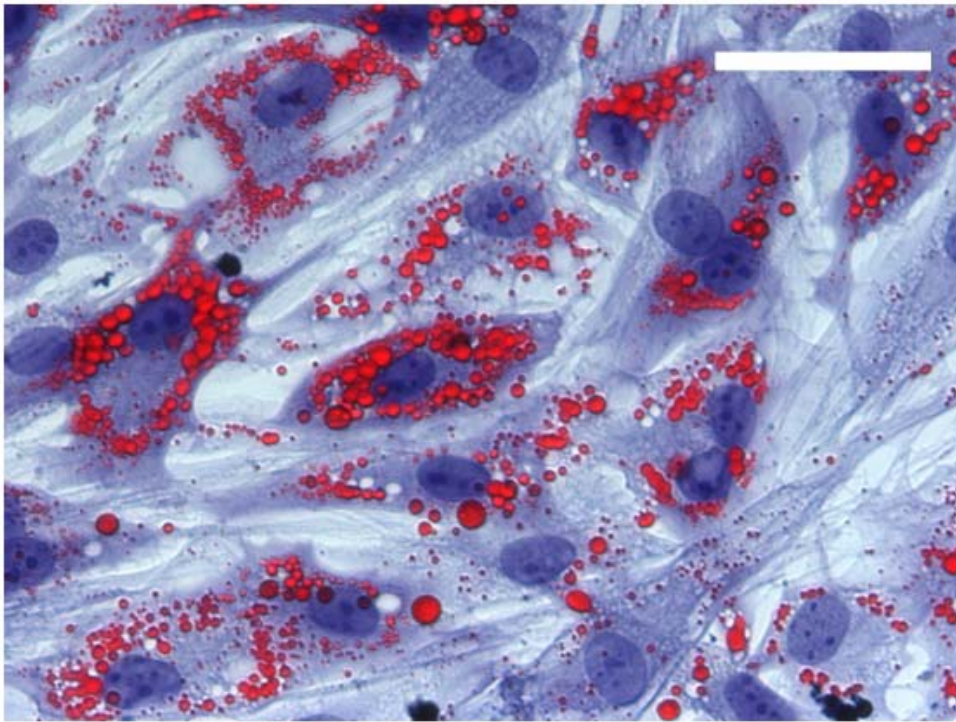


Fig. 4.16: Micrograph of hMSCs at day 13 of adipogenic differentiation showing lipid vacuoles, triglyceride in the fat storages was coloured redly through oil red O staining, scale bar: 50  $\mu\text{m}$ .

measured electrical resistance  $R_{cl}$  of the cell layer was higher in the group of adipogenic differentiation at day 29 and 39 than in the control, the capacitance of cell layer  $C_{cl}$  was lower in the differentiation group compared to the control. During the period of adipogenic differentiation, lipid vacuoles were observed in some hMSCs on the electrode of adipogenic induced chip (Fig. 4.17 (b)), but not in the control (Fig. 4.17 (c)).

The influence of chlorpyrifos on the adipogenic differentiation of hMSCs was monitored over a period of 14 days by impedance measurement. In both, chlorpyrifos and methanol treated cultures (as chlorpyrifos was dissolved in methanol, methanol was added to the medium of control chip) lipid vacuoles did not appear during the differentiation period. The methanol treated cells grew denser, and their model parameter  $R_{cl}$  increased from day 4 to day 7 of differentiation. The chlorpyrifos treated cells showed a lower density and a corresponding lower increase of normalized  $R_{cl}$  (Fig. 4.18 (a) and (b)). At day 7 of differentiation, the average of normalized  $R_{cl}$  of chlorpyrifos treated cells was 23.5 % lower than the methanol treated cells (Fig. 4.18 (c)).

The influence of chlorpyrifos on already differentiated hMSCs to adipocytes was determined. After a differentiation period of 30 days, several hMSCs showed the presence of lipid vacuoles (Fig. 4.19 (a)) and the measured average of normalized  $R_{cl}$  ( $n = 6$ ) was about 1 (Fig. 4.19 (c)). After applying 10  $\mu\text{M}$  chlorpyrifos, the average of normalized  $R_{cl}$  decreased strongly during the next 5 days by 44 % and the number of hMSCs with lipid vacuoles was much lower (Fig. 4.19 (b) and (c)). By changing the chlorpyrifos containing

medium to the differentiation medium, a recovering of the average of normalized  $R_{cl}$  was measured. On day 16 after removing chlorpyrifos, the average of normalized  $R_{cl}$  increased and reached 97.7 % of the value before applying the chlorpyrifos. During this recovery of  $R_{cl}$ , hMSCs spread and covered the exposed electrode area again; however the number of lipid vacuoles did not increase.

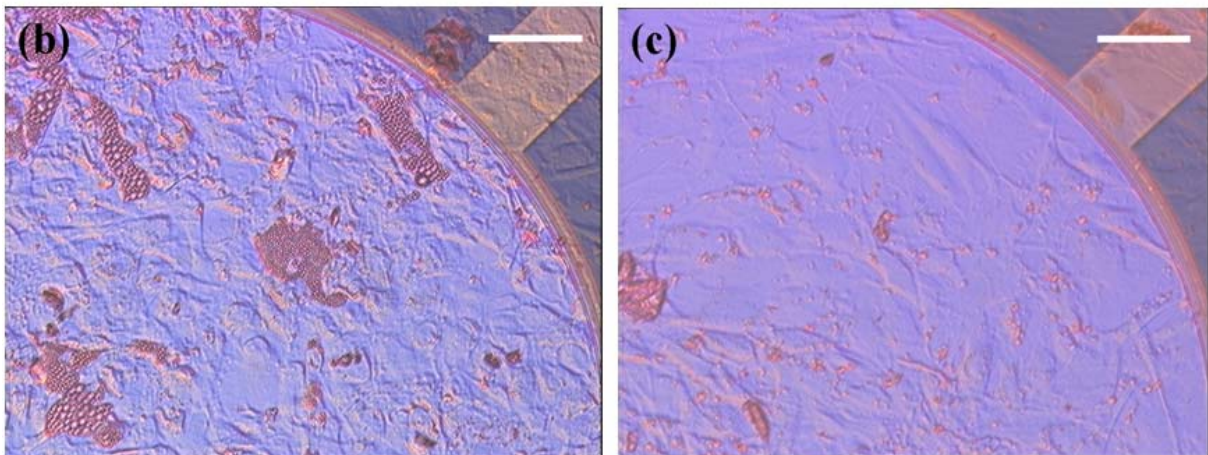
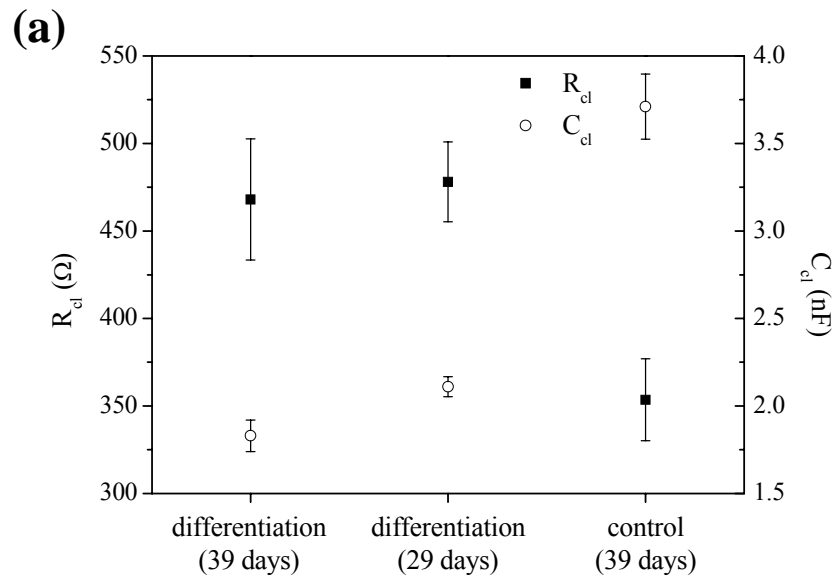


Fig. 4.17: Averages and standard errors of  $R_{cl}$  and  $C_{cl}$  ( $n$  for each group = 6) of hMSCs cultivated in the control medium for 39 days or in the differentiation medium for 29 days and for 39 days (a), micrographs of hMSCs on the electrode at day 39 of cultivation with (b) and without the adipogenic differentiation factor (c), respectively (scale bar: 100  $\mu m$ ).

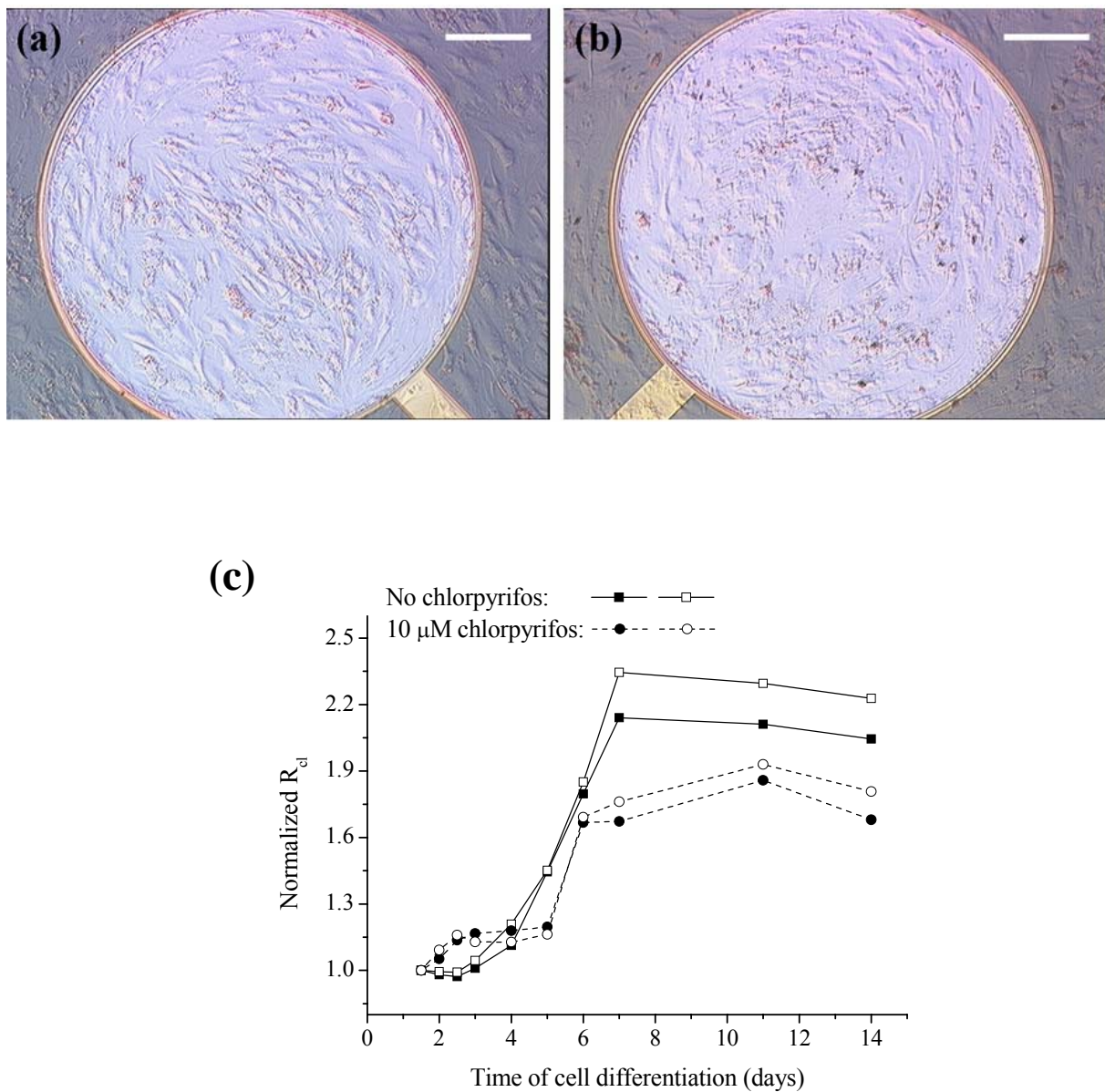


Fig. 4.18: Micrographs of hMSCs on a platinum electrode at day 9 of adipogenic differentiation cultivated without (a) and with 10  $\mu\text{M}$  chlorpyrifos (b) (scale bar: 200  $\mu\text{m}$ ), monitoring of normalized  $R_{d_i}$  of hMSCs during the adipogenic differentiation without and with 10  $\mu\text{M}$  chlorpyrifos (c).

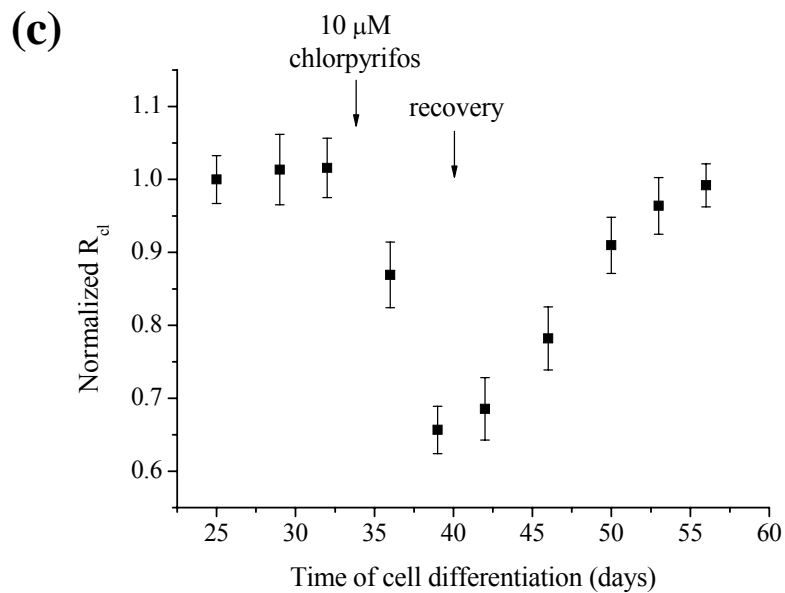
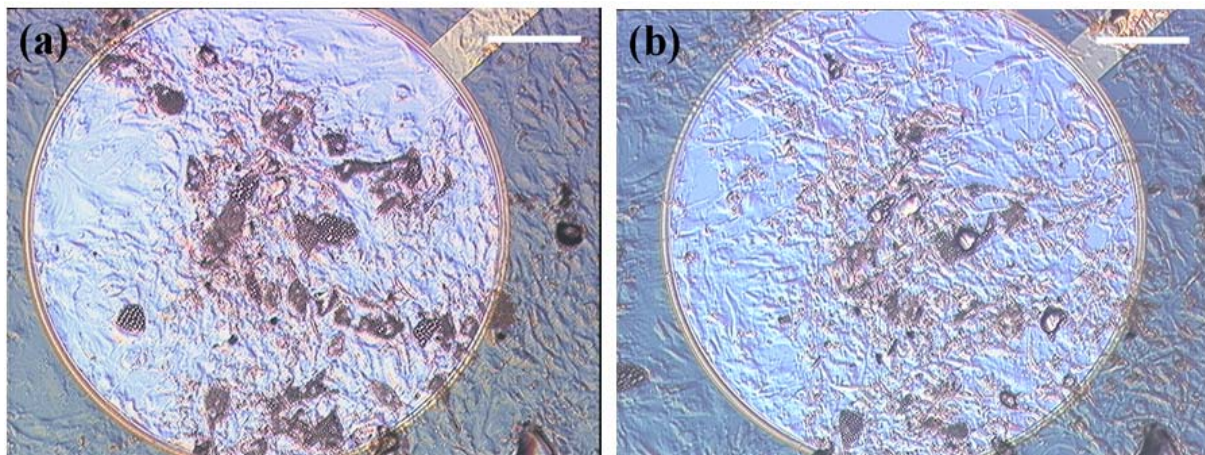


Fig. 4.19: Micrographs of hMSCs partially differentiated to adipocytes (at day 30 of differentiation) before (a) and after applying 10  $\mu$ M chlorpyrifos (at day 35 of differentiation or at day 5 after adding chlorpyrifos) (b) (scale bar: 200  $\mu$ m), influence of 10  $\mu$ M chlorpyrifos on the average and standard error of normalized  $R_d$  ( $n = 6$ ) of hMSCs differentiated to adipocytes (c).

### 4.3 Discussion

In this chapter, it is experimentally investigated whether the cellular alterations in cell assemblies related with atherosclerotic pathology (e.g. disruption of cell layer, accumulation of fat cells) can be determined by IS. Defined experimental and controllable conditions were ensured by using an *in vitro* approach based on a planar electrode-based chip. To understand how alterations of cell assemblies on electrodes are reflected in the measured impedance, general numerical simulations were performed. The simulations showed that in case of an applied electrical field with low frequency, the potential gradient is concentrated in the extra cellular region (cell/substrate or cell/cell gap) rather than the intra cellular space due to the low conductivity of cell membrane (see Fig. 4.8 (a)). Therefore, the impedance magnitude of the cell/electrode system increases at low frequencies as the cell/substrate gap or cell/cell gap decreased (see Fig. 4.9). With increasing frequency, however, the potential gradient is also observed in the intra cellular space (see Fig. 4.8 (b)), and therefore the magnitude of reactance caused by the potential distributed over the dielectric membrane was increased (see Fig. 4.9). This knowledge about the frequency dependent electrical characteristics of cell monolayer on electrodes is needed for the development of equivalent circuit models to characterize biological processes. The impedance analysis using a pair of planar electrodes on the chip was restricted by the electrode polarization at low frequencies (Boer and Osterom 1978), and also by the stray capacitance at high frequencies. As more as the measured impedance was governed by the electric double layer on electrodes, the relatively low impedance of cell layer was not able to be distinguished from the total measured impedance. The electrical properties of cell layer were revealed as the electrode impedance decrease at a higher frequency. At the sufficient high frequencies, the measured impedance without cells was similar to the spreading resistance determined by the radius of circular electrodes (Newman 1966). In case of cells on electrode, the impedance magnitude increased with increasing the density of cells adhered onto the electrode during the cultivation.

#### 4.3.1 Monitoring of Disruption of Cell Layers

It was found that IS can electrically characterize the HSV-induced disruption of cell layers involved with atherosclerotic pathology. The fabricated electrode-based chip with IS enabled to characterize electrically the behaviours of Vero cells during the cultivation or virus infection. During the cultivation, Vero cells adhered and spread well on the platinum electrode surface (see Fig. 4.11 (a)). In the confluent cell layer, it was difficult to determine the specific shape and radius of cell. Therefore, (eq. 4.1) used for the fitting to measured spectra might not be completely matched with practical conditions, since it was derived from the assumption that the cells are cylindrical in shape with certain radius. Nevertheless, the parameters  $R_b$  or  $\alpha$  of (eq. 4.1), involved with cell/cell or cell/substrate gap respectively, were tracked during the cultivation or infection. The extrapolated  $R_b$  and  $\alpha$  of Vero cells were increased at the beginning of cultivation (see Fig. 4.13). However,  $R_b$  of cells without infection reached a maximum and then decreased gradually until the first medium change. For this reason, the conductivity in cell/cell gaps might be increased or the cell/cell gap might become loose after the cells are enough proliferated on the limited area of electrode. After the first change of culture medium,  $R_b$  immediately increased and then decreased again with the time of cultivation. The reason for the rapid increase of  $R_b$  after

the medium change might be the recovery of conductivity in the cell/cell gaps or the behaviour of cells to the changed fresh medium (e.g. narrow the cell/cell gap).

The infected cells were detached from the electrode in dependence on MOI (see Fig. 4.11). During the infection, the cells were changed into round and then detached from the electrode. Correspondingly,  $R_b$  and  $\alpha$  were diminished dependently on MOI during the infection (see Fig. 4.13). At the cultivation time of 124 h, the partially exposed electrode area was clearly found when MOI was 0.06 or 0.006, but not 0.0006. This observation was well agreed with  $\alpha$ , because  $\alpha$  was reduced to the almost minimum at the MOI of 0.06 or 0.006 but not at the MOI of 0.0006 (see Fig. 4.13). However,  $R_b$  during the infection with even such a small MOI reflected sensitively the change of cell/cell gap. Therefore, the monitoring of  $R_b$  was more sensitive to diagnose the virus infection than the microscopic observations of cell detachment. This result demonstrates that the disintegration of cell assemblies can be sensitively monitored by IS. This has not only an impact on the intravascular electrical monitoring of virus-induced atherosclerosis or vessel recovery during the therapy against viruses but also on applications in virus diagnostics. Isolation of HSV in Vero cell culture provides the most reliable and specific method and is considered as the "Gold Standard" in the laboratory diagnosis (Athmananthan *et al.* 2002, El-Aal *et al.* 2006). From the results, it was shown that the electrode-based cell chip and IS can be an interesting new approach as a fast and quantitative sensing device for virus diagnostic. For the future work, it is worthwhile to characterize electrically the influence of various vaccines against virus infection by IS.

### 4.3.2 Characterization of Accumulation of Fat Cells

It was investigated whether IS can electrically characterize the accumulation of fat cells related with atherosclerotic pathology. The fabricated electrode-based cell chip and impedance measurement system showed an ability and stability for the non-invasive characterization of accumulation of adipocytes (fat cells) resulted from the long-term period of adipogenic hMSCs differentiation. From the experiment, it was found that the fabricated platinum electrodes are biocompatible to hMSCs during the cultivation and adipogenic differentiation. The resistance of hMSCs, a parameter of the equivalent circuit (Fig. 4.7), was increased correspondingly to the increase of hMSCs density on the electrodes during the cultivation. As the cells proliferated on the electrode until confluence, the resistance of cell layer  $R_{cl}$  was on a constant level (see Fig. 4.15 (b)). Under the used adipogenic differentiation condition, hMSCs differentiated to adipocytes showing lipid vacuoles in the intracellular region. The electrical properties of undifferentiated hMSCs ( $R_{cl}$  and  $C_{cl}$ ) were distinguished from those of differentiated hMSCs to adipocytes (Fig. 4.17). One interesting research theme can be the impedance monitoring of various kinds of hMSCs differentiation as a label-free method determining the level/type of differentiation. It is known from the research of Hoogduijn *et al.* (2006) that chlorpyrifos effects the cell attachment and adipogenic differentiation of hMSCs. These effects were reflected in the model parameter  $R_{cl}$ . The application of chlorpyrifos caused partially uncovered electrode areas with a decreased number of lipid vacuoles and also a rapid decrease of  $R_{cl}$ . After removing the chlorpyrifos,  $R_{cl}$  was recovered due to the re-coverage of hMSCs on electrodes. However, the increase of lipid vacuoles was not observed. From this, it was inferred that the measured  $R_{cl}$  of hMSCs is determined by the electrical properties of extra cellular space (e.g. cell/electrode or cell/cell junction) but not

by the lipid vacuoles appearing in the intracellular space during the adipogenic differentiation.

The experimental results showed that the cellular alterations in cell assemblies on atherosclerotic pathology (e.g. disruption of cell layer by virus infection, accumulation of fat cells) are well reflected in the impedance measurement. Based on these results, it is expected that cellular alterations in vessels related with atherosclerosis can be electrically characterized by IS. For the intravascular electrical characterization of atherosclerosis, however, it needs to understand the influence of complex structures and properties of vessel walls on impedance measurements. In the following chapter, it is investigated how the intravascular impedance measurement can be affected by different thicknesses of cell layers and relative positions of atherosclerotic plaques in vessels to electrodes. Furthermore, it is reported whether the intravascular electrical characterization of atherosclerotic plaques in vessels with BIC can be performed with such a sensitivity and reproducibility that relevant medical parameters by using an *in situ* atherosclerotic animal model.

#### 4.4 Conclusions

In this chapter, it was investigated whether the disruption of cells or accumulation of adipocytes involved with atherosclerotic pathology can be electrically characterized by IS. Therefore an experimental *in vitro* approach based on a planar electrode-based chip was chosen to ensure reproducible and controllable conditions. To understand how alterations of cell assemblies are reflected in the measured impedance, numerical simulations were performed. The simulations showed that the extra cellular space (cell/substrate or cell/cell gap) determines the impedance in the low frequency range. However, the high frequency electric fields were able to penetrate the cell membranes and to reveal the reactance caused by cell membranes with low conductivity. Using a fabricated electrode-based chip, the impedance spectra of Vero cells were measured during the HSV virus-induced disruption of cell layers. The behaviours of Vero cells during the HSV infection were clearly reflected in the impedance analysis. This finding demonstrates that the disintegration of cell assemblies can be monitored and qualified by IS. Therefore, the parameters related to cell/cell or cell/substrate gap were determined during the virus-induced disintegration of cell assemblies. Further, it was investigated whether the accumulation of fat in cells and an influence on cell differentiation are determinable by IS on cell assemblies. The fat accumulation was investigated by using the differentiation of hMSCs into the adipogenic direction, and the possibility of monitoring the influence on cell differentiation was investigated by using an active substance (chlorpyrifos) with known effect on the adipogenic differentiation. The experimental results showed that the cellular alterations in cell assemblies on atherosclerotic pathology (e.g. disruption of cell layers by virus infection, accumulation of fat cells) are well reflected in the impedance measurement. Considering the experimental results, it is expected that IS can be used to characterize electrically the cellular alterations in vessels related with atherosclerotic pathology (e.g. disruption of cell layers, accumulation of fat cells) for the improvement of intravascular diagnosis and therapy monitoring against atherosclerosis. However, it is necessary to investigate the use of IS for the characterization of atherosclerotic plaques in an *in situ* situation. This is described in the next chapter.

## 5 Intravascular Impedance Measurement of Vessels

The results of *in vitro* investigation in chapters 3 and 4 show that cellular alterations related to atherosclerosis can be characterized by IS. In this chapter, it is investigated which side conditions are necessary for a sensitive impedance measurement on vessel walls and whether reproducible impedance measurement can be performed in vessels. For the intravascular electrical characterization of vessel walls with high sensitivity, it is considered to use a balloon impedance catheter (BIC) with integrated flexible microelectrode arrays. To interpret correctly the impedance recorded in vessels, it is investigated how the impedance measurement of vessels can be dependent either on the different thicknesses of vessels or on the relative positions of atherosclerotic plaques in vessels to electrodes. Further, the use of multi-electrode arrays for BIC is theoretically investigated to increase the sensitivity of BIC-based impedance characterization with respect to variously distributed plaque in vessels. Finally, the feasibility of a fabricated BIC for an intravascular electrical characterization of atherosclerotic plaques is tested in an *in situ* atherosclerotic animal model which enables the impedance analysis of vessels in parallel to histological investigation.

### 5.1 Methodology

#### 5.1.1 Concept for Intravascular Impedance Measurement with BIC

The concept for an intravascular impedance measurement is based on a balloon catheter with integrated electrodes to avoid the influence of intravascular conditions (e.g. pulsatile blood flow, distance between the electrode and vessel wall). Balloon catheters are established in the treatment of vascular diseases and used to enlarge a narrow opening or passage within vessels. Fig. 5.1 shows a schematic of balloon catheter with microelectrode structures positioned on the surface of balloon, i.e. balloon impedance catheter (BIC). When the balloon is inflated, the microelectrodes of BIC contact to the vessel walls. From Fig. 5.1, it is anticipated that the intravascular electrical characterization of atheromatous vessels can be dependent either on the different thicknesses of vessels or on the relative positions of plaque to electrodes. Therefore, the dependence of impedance measurement on those factors should be investigated for the trustable intravascular IS of atherosclerosis. To test the feasibility of intravascular impedance measurement, an *in situ* animal model established in Department of Medicine in University Hospital of Mannheim is used. For the first investigation under *in situ* condition, the use of animal models instead of investigation on humans is necessary because of safety reasons and since histological investigation in parallel to impedance analysis is required which can not be performed on humans.

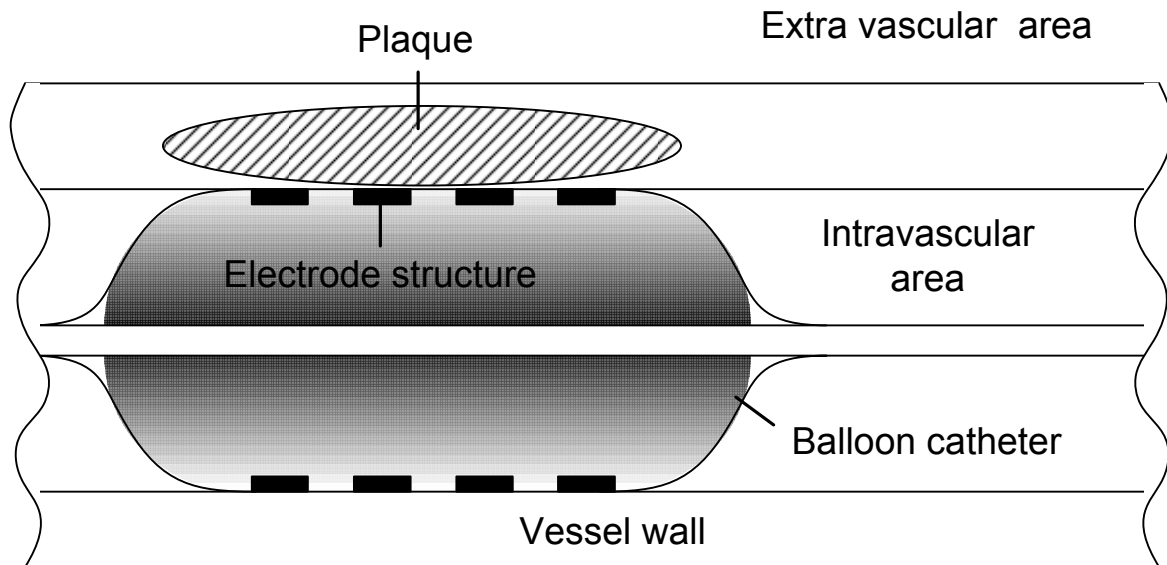


Fig. 5.1: Schematic of balloon impedance catheter (BIC) with microelectrode structure for intravascular IS of atheromatous vessel walls.

### 5.1.2 Fabrication and Characterisation of Microelectrodes

To enable the combination of a balloon with microelectrodes, flexible electrode structures were microfabricated. For the fabrication on flexible microelectrodes, the process technology described by Stieglitz *et al.* (1997) and Stieglitz and Meyer (1999) was used. The geometrical dimensions of the electrode structures were adapted to the size of aortas of rabbit and to the size of plaques of the chosen animal model. As substrate and insulation material for electrode structures, the flexible polyimide PYRALIN PI 2611 (Du Pont) was used since it has a low water absorption and low conductivity as shown in 1.4. First, the polyimide resin was coated on a silicon wafer by spin coating and imidized in a curing process at 350°C under nitrogen atmosphere. After making the rough surface of polyimide by reactive ion etching for a sufficient adhesion of metals, a titanium adhesion layer of 30 nm thickness and platinum of 300 nm thickness were deposited in sequence by sputtering. Platinum was used for the electrode material due to its biocompatibility (Thanawala *et al.* 2007) and electrochemical stability (Sawyer *et al.* 1995). The platinum structure of four-rectangular electrodes, transmission lines, and terminal pads was patterned by lift-off technique. After the deposition of polyimide layer with 5  $\mu\text{m}$  thickness over the patterned metals, the areas of electrodes and terminal pads were exposed by reactive ion etching. Fig. 5.2 showed a fabricated polyimide-based microelectrode array with four rectangular-shaped electrodes. The rectangularly exposed area of electrodes was 100  $\mu\text{m}$  by 100  $\mu\text{m}$  and the separation distance between centres of electrodes was 333  $\mu\text{m}$ .

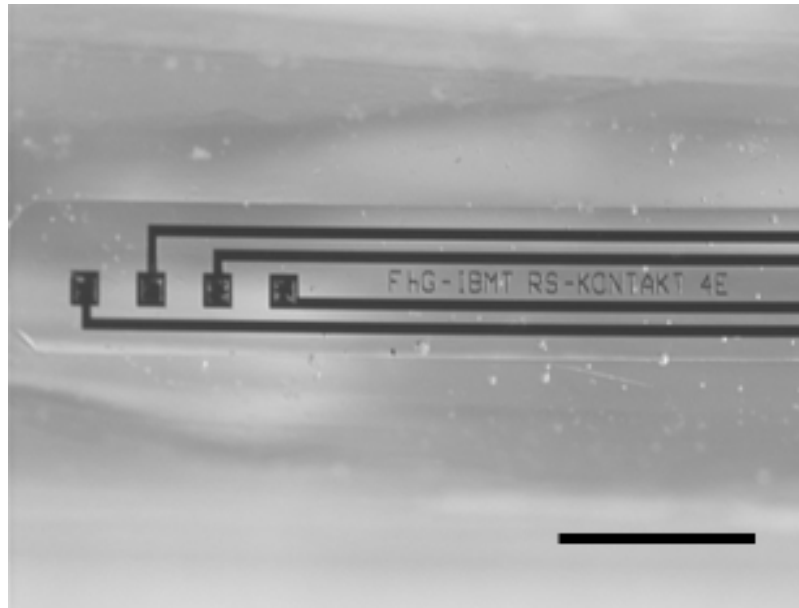


Fig. 5.2: Fabricated flexible polyimide-based electrode array with four electrodes, exposed area of rectangular electrode:  $100\ \mu\text{m} \times 100\ \mu\text{m}$ , separation distance between electrode centers:  $333\ \mu\text{m}$  (scale bar:  $1\ \text{mm}$ ).

The impedance characteristic of the electrode structure in two-electrode and four-electrode configuration was determined experimentally in electrolytes with known electrical properties. The resistance of the electrolytic solution was determined from the measured impedance spectra and compared to calculated values. The impedance of electrolyte measured by using microelectrodes can be presented as a series of constant phase element ( $\text{CPE}_e$ ) describing the interfacial electrode impedance (Boer and Osterom 1978) and resistance of electrolyte ( $R_s$ ) with a parallel connected stray capacitance ( $C_s$ ) as Fig. 5.3. The resistance of electrolyte is determined by the configuration and dimension of electrodes and the conductivity of electrolyte (Kovacs 1994). According to Kovacs (1994), the resistance of object with the conductivity of  $\sigma$  for a single planar rectangular electrode of length  $l_e$  and width  $w_e$  is as follows.

$$R_s = \frac{\ln(4l_e/w_e)}{\sigma\pi l_e} \quad (\text{eq. 5.1})$$

As described in chapter 1.3, the four-electrode method can be used to avoid the electrode impedance. A four-point electrode arrangement, which consists of outer electrodes applying the currents and inner electrodes measuring the potential, with the equal separation distance between electrodes ( $r$ ) is called Wenner Alpha type (Oldenburg and Jones 1998). For a four-point electrode structure of the Wenner alpha type, an analytically calculated resistance of a semi-infinite object ( $R_{\text{inf}}$ ) is as follows (Oldenburg and Jones 1998).

$$R_{\text{inf}} = \frac{1}{2\sigma\pi r} \quad (\text{eq. 5.2})$$

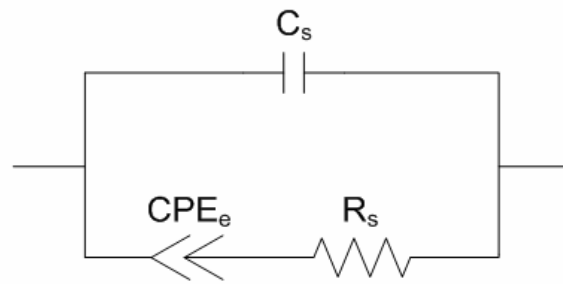


Fig. 5.3: An equivalent circuit of electrolyte impedance measured by using electrodes in,  $CPE_e$ : constant phase element for interfacial electrode impedance,  $R_s$ : electrolyte resistance,  $C_s$ : stray capacitance.

To characterize the fabricated electrode array with rectangular-shaped electrodes experimentally, the impedance of 0.9% NaCl electrolyte ( $\sigma = 1.6 \text{ S/m}$  at  $25^\circ\text{C}$ ) was measured by using an impedance analyzer and interface 1294 (Solartron Analytical, Farnborough, UK). For the linear condition of impedance measurement, the alternating potential was set to 100 mV. In the frequency range of 1 Hz to 1 MHz, the responsive current was recorded. Thus, the impedance, the ratio of alternating potential to current, was measured. From the measurement with two- and four-electrode method (Wenner Alpha type), it was investigated how much the electrode impedance contributes to the total measured impedance. By fitting the equivalent circuit of Fig. 5.3 to the measured spectra, the electrical characteristics of electrode/electrolyte interface and the resistance of electrolyte were interpreted. Additionally, the impedance of NaCl electrolyte was measured at  $25^\circ\text{C}$  according to the different concentration of NaCl in liquid. The concentration of NaCl in liquid used for the experiment and the correspondent conductivity of NaCl electrolyte at  $25^\circ\text{C}$  is as follows.

Tab. 5.1: Concentration of NaCl in liquid (NaCl conc.) and corresponding conductivity of NaCl electrolyte at  $25^\circ\text{C}$  (Sawyer *et al.* 1995).

NaCl conc. (%)	Conductivity (S/m)	NaCl conc. (%)	Conductivity (S/m)
0.1	0.20	1.2	2.08
0.3	0.57	1.5	2.56
0.6	1.09	1.8	3.01
0.9	1.60		

### 5.1.3 Investigation of Effect of Vessel Thickness on Intravascular Impedance Measurement

In the intravascular impedance characterization of vessels with BIC, the different thickness of vessel walls and extra vascular conditions may affect the measured impedance if the vessel thickness is so thin that current is sufficiently distributed beyond the vessel. To characterize the effect of vessel thickness on intravascular impedance measurement by using FEM simulation, a simple quasi-vessel model as Fig. 5.4 was considered at first. The quasi-vessel model consists of vessel containing non-plaques ( $\sigma = 0.43 \text{ S/m}$ ,  $\epsilon_r = 10^5$ , Slager *et al.* 1992) and the body liquid (blood) as an extra vascular material ( $\sigma = 0.68 \text{ S/m}$ ,  $\epsilon_r = 3 \times 10^3$ , Schwan 1963) although different types of tissues or body liquids surround the vessels in practice. The electrode array of Wenner alpha type was on the intravascular vessel wall in the model. The area of rectangular electrodes and equal separation distance between centers of electrodes were  $100 \mu\text{m} \times 100 \mu\text{m}$  and  $333 \mu\text{m}$ , respectively. In Fig. 5.4, C1, C2 and V1, V2 were electrode pairs for current applying and voltage measurement, respectively. For the FEM simulation, it was assumed that all materials are regarded as source-free, homogenous, and linear volume dielectrics. If the magnetic fields in them are negligible, then the potential distribution induced by current sources satisfies the generalized Laplace's equation. The impedance can be obtained by using volume dielectric analysis involving the lead field theory and the reciprocal

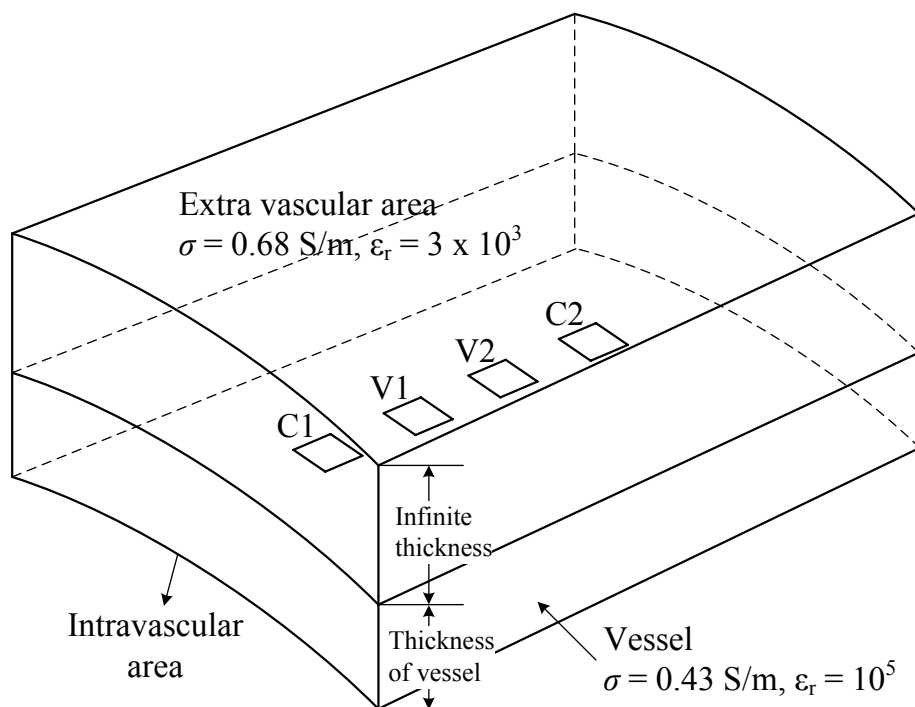


Fig. 5.4: Schematic of a quasi-vessel model with electrode array of Wenner alpha type (area and separation of rectangular electrodes:  $100 \mu\text{m} \times 100 \mu\text{m}$  and  $333 \mu\text{m}$ ), C1, C2 and V1, V2: electrode pairs on intravascular wall for current injecting and voltage measurement, respectively.

energization of leads (Malmivuo and Plonsey 1995). The sensitivity  $S$  within the measured biomaterial is a measure of the contribution of a small volume segment  $dv$  to the total measured impedance, and the total measured impedance  $Z$  is as follows (Geselowitz 1971, Martinsen 2004).

$$Z = \int_V \frac{S}{(\sigma + i\omega\varepsilon_0\varepsilon_r)} dv, \quad S = \frac{\vec{J}_1 \cdot \vec{J}_2}{I^2} \quad (\text{eq. 5.3})$$

where  $\sigma$  and  $\varepsilon_r$  are the conductivity and relative permittivity, respectively,  $\varepsilon_0$  is vacuum permittivity ( $= 8.854 \times 10^{-12} \text{ Fm}^{-1}$ ),  $i = (-1)^{1/2}$ ,  $\omega = 2\pi f$  with  $f$  the frequency of the electric fields,  $\vec{J}_1$  the current density when a current  $I$  flows between the two current electrodes, and  $\vec{J}_2$  the current density when  $I$  flows between the two voltage electrodes.

With increasing positive sensitivity of the confined volume, the contribution of the confined volume to the total measured impedance increases. Similarly, the decreasing sensitivity makes the lower contribution of the confined volume to the total impedance (Martinsen 2004). By FEM (used software: FlexPDE, PDE Solutions, Antioch, USA), the sensitivity and impedance magnitude at 10 kHz were simulated with respect to different thicknesses and different inner radii of vessel wall in the quasi-vessel model.

For the experimental validation of the dependence of impedance measurement on the thickness of vessel, a simple two-layer model was considered as Fig. 5.5 (a). The two-layer model consists of the electrolyte with known conductivity as the layer 1 (regarded as a vessel) and an insulating material with almost zero conductivity as the layer 2 (regarded as an extravascular material). Fig. 5.5 (b) shows the experimental set-up for the two-layer model. The 0.9% NaCl solution ( $\sigma = 1.6 \text{ S/m}$  at  $25^\circ\text{C}$ ) was used as the layer 1 and an insulated glass plate with air was used as the layer 2. After fixing the fabricated electrode array onto the centre of a container (diameter of 5.5 cm) bottom, 0.9% NaCl solution was poured in the container. The level of the electrolyte was controlled by using an insulated glass plate (diameter of 3.5 cm) which was integrated with a stick and micro manipulator and aligned in parallel to the bottom of the container. The electrodes as Wenner Alpha type were electrically connected with the impedance analyzer, and the impedance magnitude was measured at 10 kHz and  $25^\circ\text{C}$  with respect to different thickness of electrolyte. Further, the measured impedance magnitude was compared with simulated one in the two-layer model of Fig. 5.5 (a). A program code for the simulation based on the two-layer model was exemplarily shown in Appendix C.

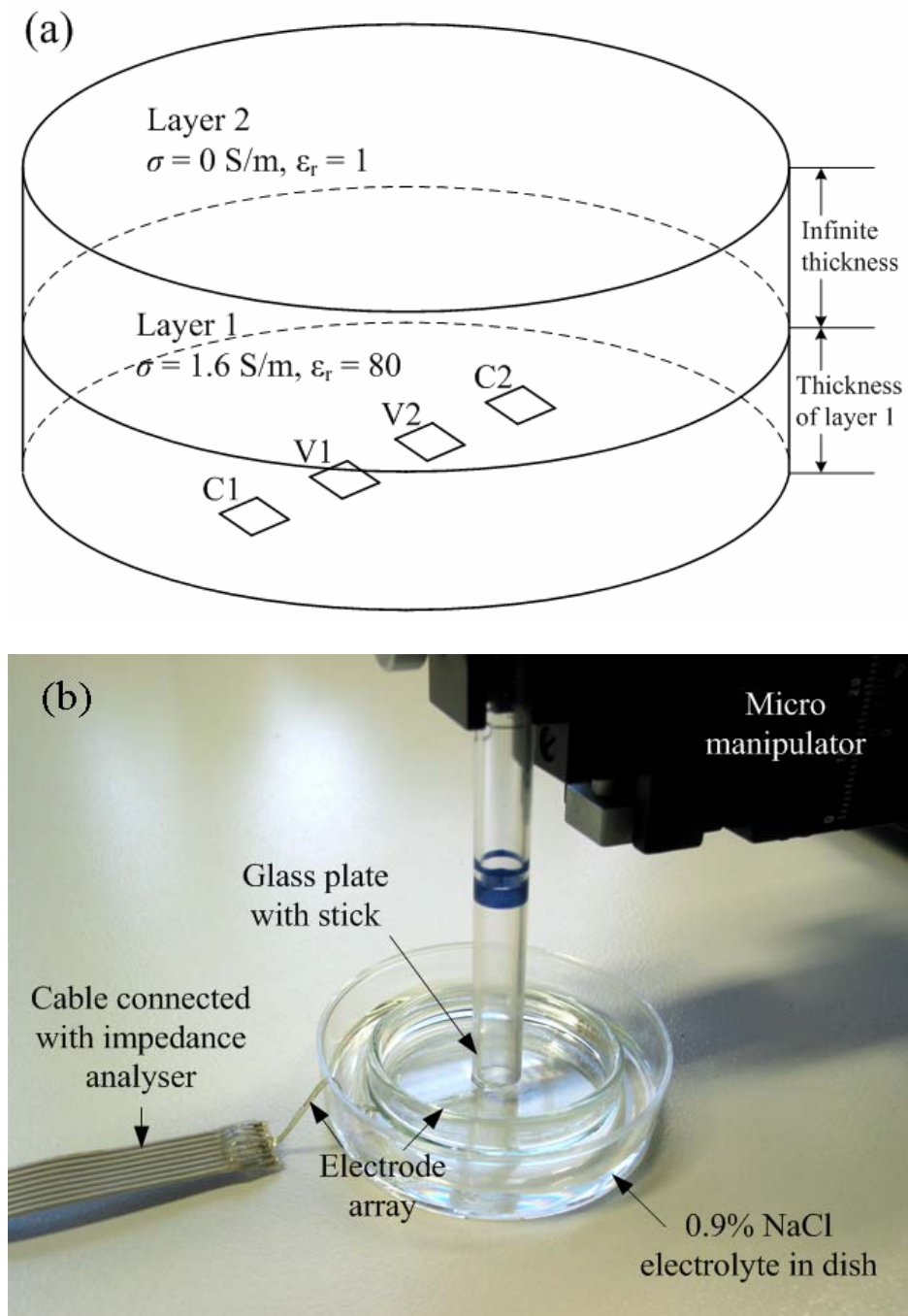


Fig. 5.5: Schematic of a two-layer model with electrode array of Wenner alpha type (area and separation of rectangular electrodes:  $100 \mu\text{m} \times 100 \mu\text{m}$  and  $333 \mu\text{m}$ ), C1, C2 and V1, V2: electrode pairs on the bottom of layer 1 for current injecting and voltage measurement, respectively (a), experimental set-up for two-layer model with electrode array, layer 1: 0.9% NaCl electrolyte, layer 2: an insulated glass plate with air (b).

#### 5.1.4 Investigation of Effect of Relative Plaque Position to Electrodes on Intravascular Impedance Measurement

The intravascular diagnosis of atherosclerosis by using BIC is dependent on how sensitively the atherosclerotic plaques variously distributed in vessels can be characterized by the impedance measurement. If the atherosclerotic plaque is more far away from the electrodes, the contribution of plaque on the impedance measurement is more decreased since the electric fields induced by the electrodes less reach the plaque. Therefore, the relative positions of plaque to electrodes affect the sensitivity of BIC. To investigate the influence of relative positions of plaque to electrodes on the intravascular impedance measurement, FEM simulation based on a quasi-vessel model containing lipid plaque with BIC was used. A quasi-atheromatous vessel model for FEM simulation was designed like Fig. 5.6. The radius and the length of balloon expanded in the lumen were 2.5 mm and 12 mm, respectively. A four-terminal electrode array that has same dimension and configuration of the fabricated one was positioned on the surface of balloon. It was assumed that the electrode array is completely contacted to the endothelium of vessel as the inflation of balloon. The outer electrodes were used for injecting an alternating current and the inner electrodes for measuring the potential (Wenner Alpha type). The lipid, located in the vessel wall, had a crescent shape on the cross section (distributed  $45^\circ$  to  $-45^\circ$  from  $x$  axis), and the longitudinal length of lipid was 2.4 mm. The shape of vessel boundary on the cross section was eccentric. The length of eccentric vessel was 8.2 mm on  $x$  axis and 8.0 mm on  $y$  axis. On the  $x$  axis in Fig. 5.6 (a), the thickness of vessel on the left side (side of no lipid in the vessel) was 1.1 mm. Since the ratio of thickness of vessel to the separation between the outer current electrodes is above than 1, the impedance is almost not affected by the extra vascular conditions (see chapter 5.2.2). To set the different relative positions of lipid plaque to electrode array, the electrode array was rotated with angle ( $\theta_e$ ) from the  $x$  axis. Further, the lipid depth from the endothelium was set as  $r_l$  and the longitudinal separation between the middles of electrode array and the lipid as  $z_l$ . The electrical properties of the vessel and lipid were shown in Tab. 5.2. The relative permittivity of vessel was inferred from the property of muscle (Gabriel *et al.* 1996). The current density and impedance were simulated by 3D FEM with (eq. 5.3) at the frequency of 1 k or 10 kHz (used software: FlexPDE, PDE Solutions, Antioch, USA). The initial values for  $\theta_e$ ,  $r_l$ , and  $z_l$  used for the simulations were given in Tab. 5.3. A program code for the simulation with respect to different  $\theta_e$  when  $r_l$  and  $z_l$  are 0.4 mm and 0 mm respectively was shown in Appendix D.

Tab. 5.2: Conductivity and relative permittivity of materials used for FEM simulation with atheromatous vessel model of Fig. 5.6 (Slager *et al.* 1992, Gabriel *et al.* 1996).

Frequency (Hz)	Conductivity (S/m)		Relative permittivity	
	1 k	10 k	1 k	10 k
Vessel	0.43	0.43	$2 \times 10^5$	$10^5$
Lipid	0.034	0.034	1500	500

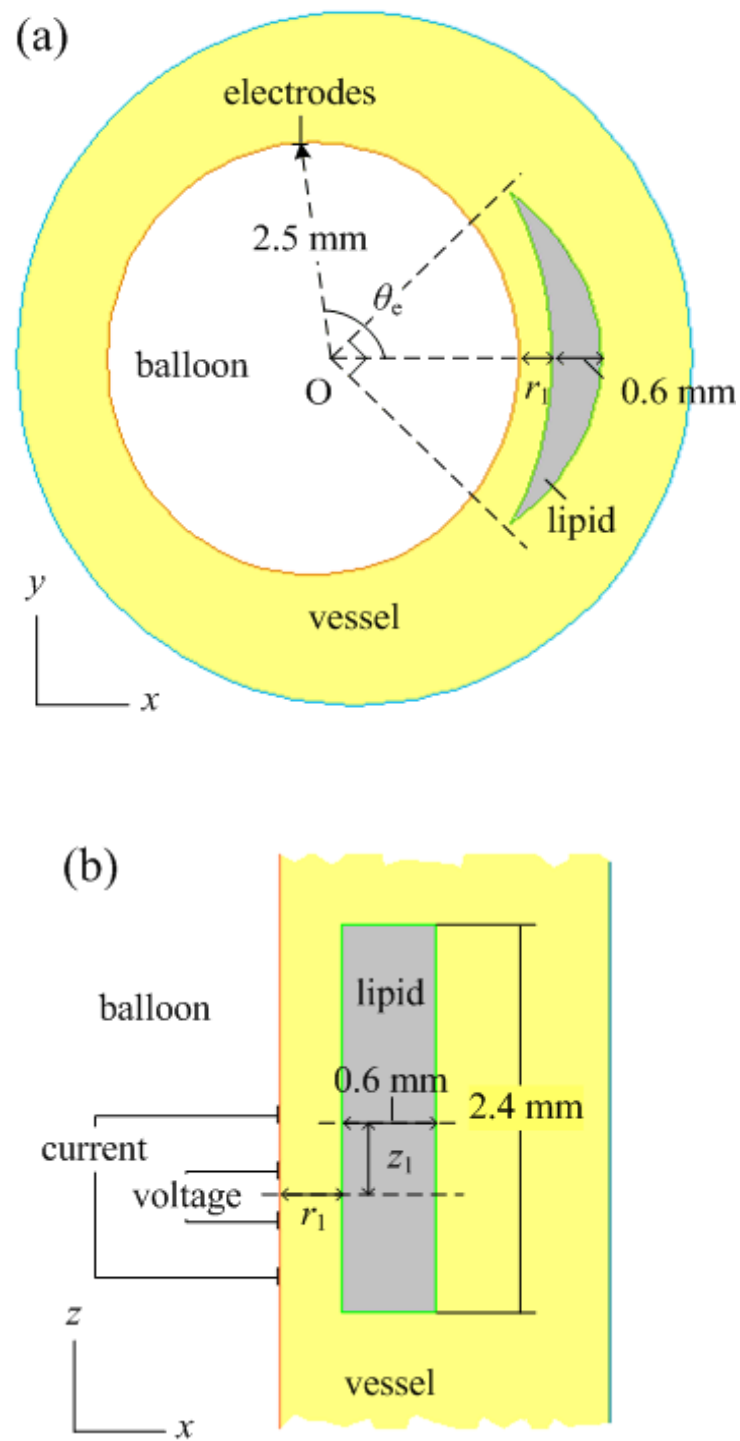


Fig. 5.6: Quasi-atheromatous vessel model with BIC for 3D FEM simulation on the cross (a) and longitudinal section (b) at the middle of electrode array,  $O$ : middle axis of catheter,  $\theta_e$ : separation angle between the electrode array and  $x$  axis,  $r_1$ : depth of lipid from the endothelium,  $z_1$ : longitudinal separation between the middles of electrode array and lipid.

Tab. 5.3: Value set of parameters used for FEM simulation with atheromatous vessel model of Fig. 5.6 (Cho and Thielecke 2006).

Procedure	$\theta_e$ (°)	$r_l$ (mm)	$z_l$ (mm)
1 <sup>st</sup>	Variable	0.4	0
2 <sup>nd</sup>	0	Variable	0
3 <sup>rd</sup>	0	0.4	Variable

$\theta_e$ : Separated angle between the electrode array and the lipid,  $r_l$ : Lipid depth from the endothelium,  $z_l$ : Longitudinal separation between the lipid and the electrode array

Further, it was investigated by simulation whether the impedance measurement of a four-electrode arrangement of Wenner Alpha type is affected by neighbored electrode arrangements positioned concentrically on the balloon catheter. This was investigated since too closely neighbored electrodes in the arrays can affect the current flow around electrodes due to high conductivity of electrodes themselves (so called "short-circuiting" effect). To estimate the short-circuiting effect on the impedance measurement, a set of five electrode arrangements (Wenner Alpha type), equidistantly arranged on a balloon (equal arc length), was considered as Fig. 5.7. The middle electrode arrangement of the set was located under the middle of lipid in the model of Fig. 5.6 ( $\theta_e = 0$ ,  $r_l = 0.4$  mm,  $z_l = 0$ ). Then, for the middle electrode arrangement, the measurable impedance magnitudes at 10 kHz were simulated in dependency of the equal arc length of the neighbored arrangements.

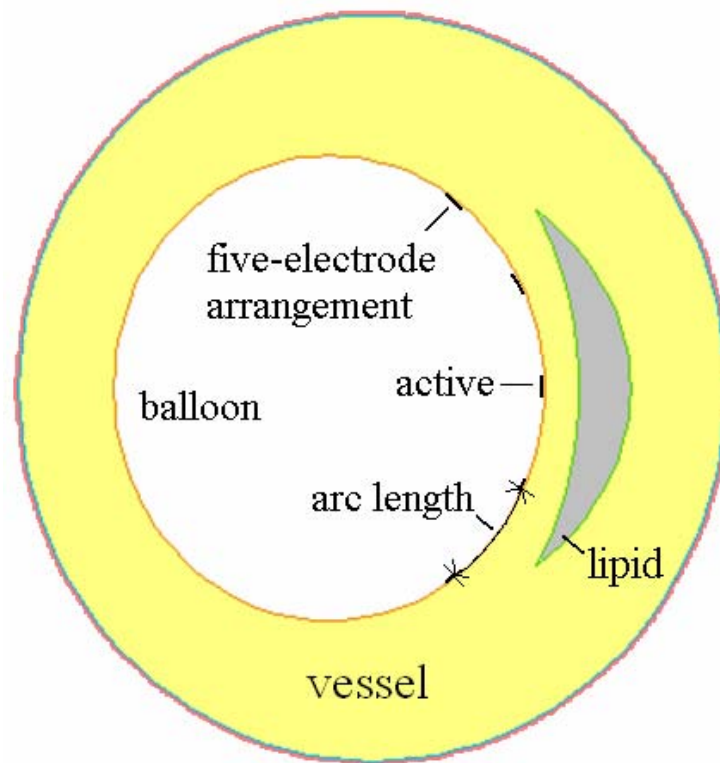


Fig. 5.7: Schematic of a set of five electrode arrangements positioned concentrically on the balloon catheter and separated each other with equal distance (arc length), the middle electrode arrangement (active) is located under the middle of lipid in the model of Fig. 5.6 ( $\theta_e = 0$ ,  $r_1 = 0.4$  mm,  $z_1 = 0$ ).

### 5.1.5 Experiment of Atherosclerotic Animal *in situ*

Animal experiments were designed in accordance with the German Law for Animal Protection and were approved by the Review Board for the Care of Animal Subjects in Karlsruhe, Germany. The experiments conform to the Guide for the Care and Use of Laboratory animals published by the US National Institutes of Health (NIH Publication No. 85–23, revised 1996). Six female New Zealand White rabbits (Harlan-Winkelmann, Borchon, Germany), 1.5 kg were kept at standard conditions (temperature 21 °C, humidity 55%) and fed with a 5% cholesterol-enriched diet (Ssniff Spezialdiäten GmbH, Soest, Germany) for 17 weeks to induce atherosclerosis. Chow and water were fed ad libitum. Anesthesia was induced by intramuscular application of ketamine 35 mg/kg (Hostaket®, Intervet, Unterschleißheim, Germany) and xylazine 5 mg/kg (Rompun® Bayer, Leverkusen, Germany). A 20 G cannula (BD, Franklin Lakes, NJ, USA) was placed into the ear vein to maintain the anesthesia. After shaving the groin and dissection of the right femoral artery, a 4 F sheath (Cordis, Johnson and Johnson Company, L.J. Roden, The Netherlands) was introduced and a bolus of 500 international units heparin (Hoffman-La Roche, Grenzach-Wyhlen, Germany) was administered. Under fluoroscopy, a 0.014 inch guidewire (Guidant, Temecula, CA, USA) was positioned right above the aortic valve and an angiogram of the thoracic aorta was performed by injection of 5 ml contrast dye (Imeron 400 MCT, Altana, Konstanz, Germany) via a Multipurpose Catheter (Cordis, Johnson and Johnson Company, L.J. Roden, The Netherlands), which was documented on

a VHS-video tape. Subsequently, the aorta was scanned using a 20 MHz, 2.9 F ultrasound catheter (Jomed, Rancho Cordova, USA) by manual pullback beginning distally of the aortic arch to the renal artery. All images were digitally stored. The angiograms and ultrasound images were visually analyzed by two independent investigators. After all images were obtained, the animals were sacrificed by a lethal dosage of pentobarbital and the thoracic aorta was prepared. The aorta was flushed by physiological saline solution over the femoral sheath to maintain tissue humidity and an arteriotomy was performed distally from the renal arteries. Then, black points were marked on the superficial layer of aorta via the needle with ink to guarantee an exact matching of the histology of marked aortic tissues and the impedance measurements (separation distance between marked points: 5 – 10 mm).

For the intravascular impedance measurement of vessels, a fabricated BIC as Fig. 5.8 was used. The polyimide-based electrode array was integrated with a balloon catheter (Jomed Maestro 3.0 diameter, length 20 mm, Jomed, Rangendingen, Germany) by fixing it on the balloon surface with a silicon rubber. The polyimide-based electrode array was flexible enough and ultralight that the property of the balloon catheter was not degraded during the expansion and contraction of balloon. The impedance measurement system consisted of an impedance analyzer SI 1260 (Solartron, Farnborough, UK) in combination with a bioimpedance interface SI 1294 (Solartron, Farnborough, UK). A sinusoidal current was fed via two outer electrodes and controlled in a way that the voltage drop across the inner electrodes was 10 mV (Wenner Alpha type). Such a low level of voltage drop for IS guaranteed the linear condition as a premise of IS and the conservation of cell membrane from over-potential. Before using the BIC on the animal models, the electrode array was calibrated in saline of known electrical conductivity. After introduction of the guide wire, the impedance catheter system was placed distally of the aortic arch. The BIC was exactly positioned at the anterior wall of the aorta under fluoroscopy control and the balloon catheter was inflated with 0.5 atm to ensure a close contact of the electrodes to the aortic wall. When the position of electrodes is exactly matched to the marked points on the surface of aorta, the impedance was measured at 1 kHz and 10 kHz at room temperature. For all measurements, the magnitude and the phase angle of the impedance were determined. Each impedance measurement could be performed during an inflation period of 30 seconds. Fifteen to 25 marked segments of each aorta were measured starting at the aortic arch and ending in the area of the diaphragm.

After the impedance measurements, each aorta was dissected and cryoconserved for histological analysis. Sections of 4  $\mu\text{m}$  were sliced near the center of the marked segment. After staining of sections with hematoxylin-eosin solution, photomicrographs were taken to measure plaque and media thicknesses. To avoid the influence of relative plaque positions to the electrode array on the measured impedance (see chapter 5.2.3), the histology of sections was analyzed at the marked points (measured points). The histomorphologic classification was performed without knowledge of the impedance results. Segments were classified into three groups. The group 'P0' represented segments without any plaque formation. Group 'PI' represented segments with plaque thickness smaller than that of the aortic media and group 'PII' plaques thicker than that of the aortic media. From the results in chapter 5.2.2, it was anticipated that if the thickness of aorta is below the separation distance between the current electrodes (1 mm), the impedance measurement might be strongly affected by the thickness of vessel and the extra vascular space of air with zero conductivity under the used *in situ* animal models. To minimize the dependence of impedance on the different thicknesses of vessels, a new analytic concept

of impedance change versus frequency (ICF) was created as follows. Since the media of vessels contains muscle cells, it was assumed that the conductivity of aorta without plaque is mainly governed by one of muscles. On the other hand, as more as the aorta contains the lipid plaques, the conductivity of aorta with plaque is more governed by one of fat. According to Gabriel *et al.* (1996), the conductivity of muscles is lower at 1 kHz than at 10 kHz, however, the conductivity of fat is nearly constant both at 1 kHz and 10 kHz. Therefore, it was inferred that ICF ( $|Z|_{1\text{kHz}} - |Z|_{10\text{kHz}}$ ) of aorta without plaque is presented by positive values however ICF of aorta with plaques is close to zero. Statistical comparison of values was made by the Student *t*-test with a statistical analysis software package (ORIGIN 6.1, Northampton, MA, USA). Differences between the classified groups were considered significant at  $p < 0.05$ .

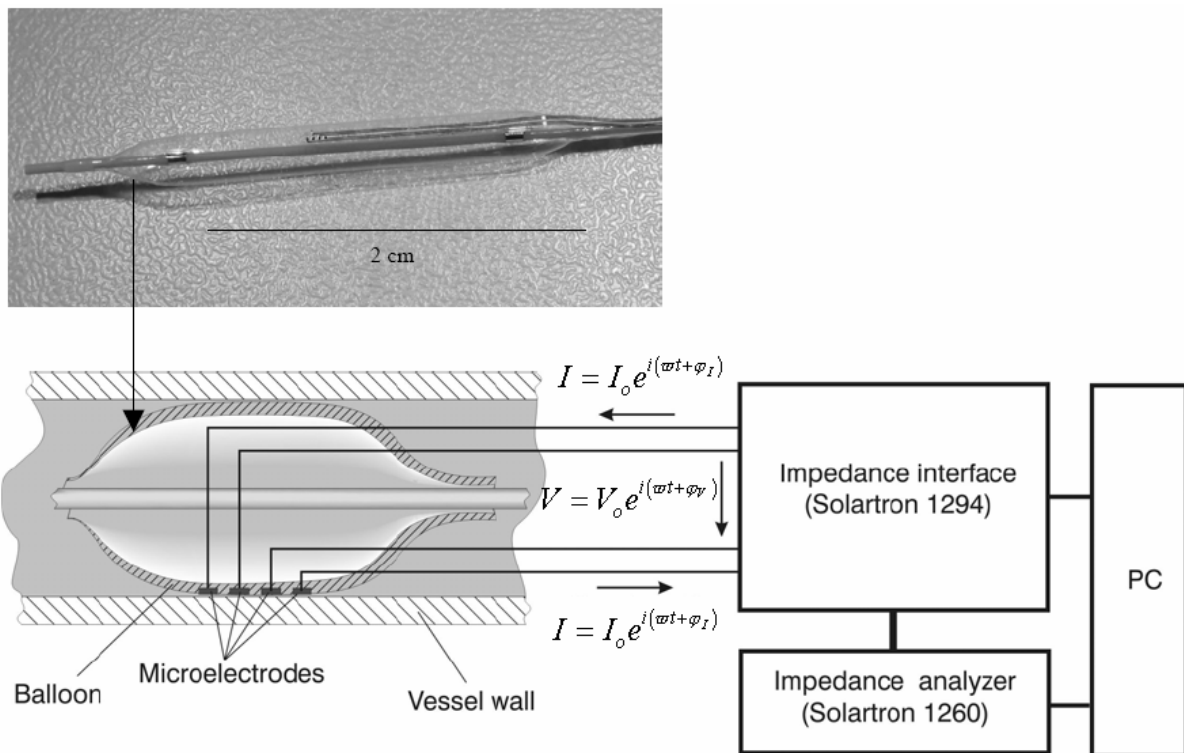


Fig. 5.8: Expanded balloon of BIC (upper) and schematic of intravascular impedance measurement of vessel walls with BIC,  $I$ : current with the amplitude of  $I_o$  and phase of  $\phi_I$ ,  $V$ : potential with the amplitude of  $V_o$  and phase of  $\phi_V$  (Süselbeck *et al.* 2005).

## 5.2 Results

### 5.2.1 Electrical Characteristics of Electrode Array

With the fabricated electrode array, the impedance spectra of 0.9% NaCl at 25°C measured by the two-electrode and four-electrode method were shown in Fig. 5.9. In case of the two-electrode method, the magnitude of impedance decreased with increasing frequency, whereas the slope of the curve was steeper at frequency below several tens of kHz and was flatter (almost constant) above several tens of kHz. The phase was about  $-75^\circ$  at frequencies below 1 kHz. In the frequency range from 1 kHz to 200 kHz, the phase increased with increasing frequency up to  $-12^\circ$  and in the frequency range above 200 kHz, the phase decreased. For the resistance of electrolyte, the fitting analysis based on the measured impedance data and the equivalent circuit model of Fig. 5.3 resulted in a value of 5.93 k $\Omega$ . The calculated value by using (eq. 5.1) was 5.52 k $\Omega$ . In case of the four-electrode array of Wenner Alpha type, the measured magnitude and phase of impedance were almost constant in the frequency range of 1 kHz to 100 kHz (Fig. 5.9). In this frequency range, the average and standard deviation of measured impedance magnitude and phase were  $296.0 \pm 17.5 \Omega$  and  $-0.6 \pm 1.9^\circ$ , respectively. The average of resistances of measured impedance at the frequencies from 1 kHz to 100 kHz was  $295.9 \pm 17.5 \Omega$ . By using (eq. 5.2), the resistance of electrolyte was calculated to 298.7  $\Omega$ . Beyond the frequency range, the impedance magnitude was slightly increased and the phase was decreased (see Fig. 5.9).

With respect to the different concentration of NaCl in liquid, the impedance spectra of NaCl electrolyte measured at 25°C by using an four-electrode arrangement of Wenner Alpha type were shown in Fig. 5.10 (a). Below 100 Hz, the impedance magnitudes were not clearly distinguishable at the different NaCl concentration. The frequency range at which the impedance magnitude became constant was dependent on the concentration of NaCl (see Fig. 5.10 (a)). At the different concentration of NaCl in liquid, the calculated and measured resistances were shown in Fig. 5.10 (b). The resistances measured in the frequency range of 1 kHz to 10 kHz were well dependent on the concentration of NaCl and also agreed to the values calculated by (eq. 5.2).

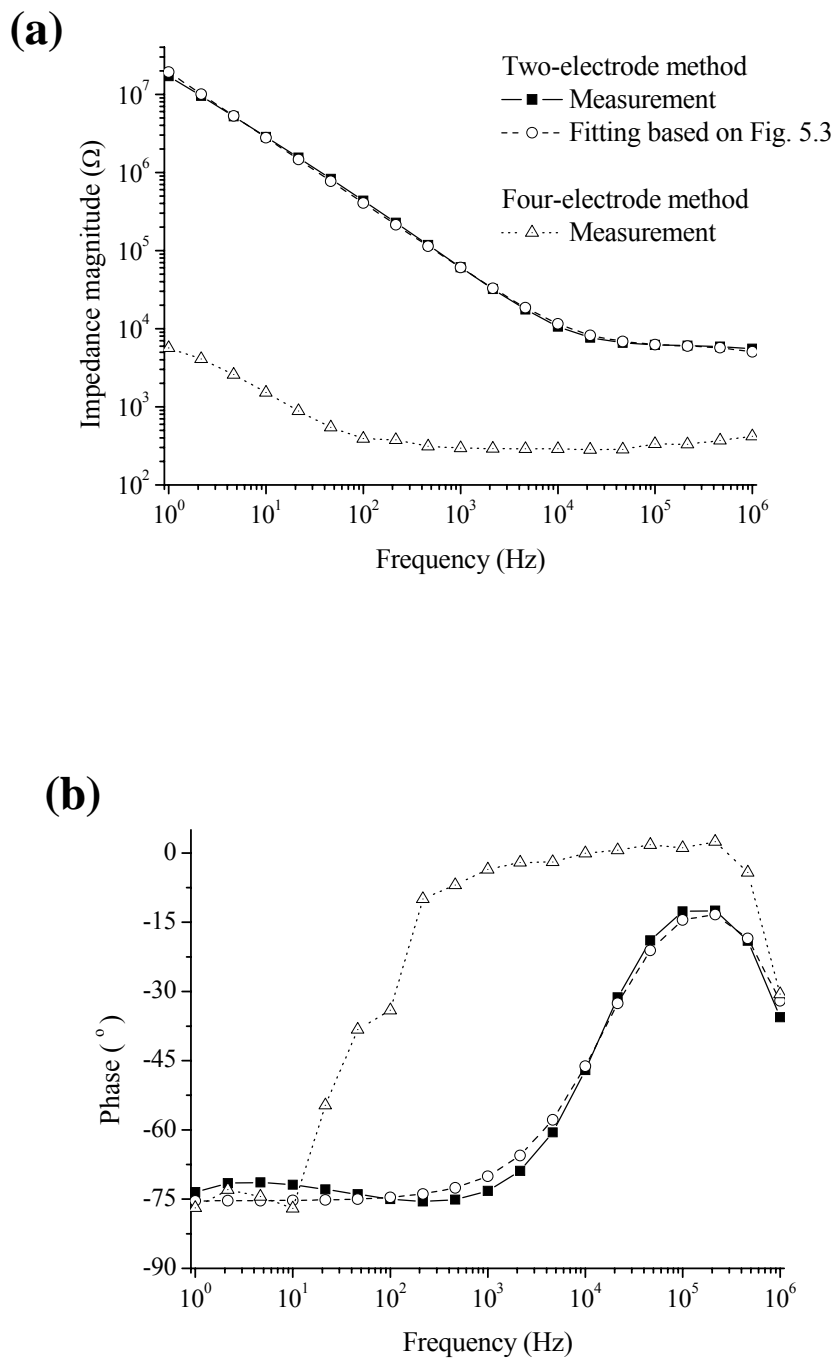


Fig. 5.9: Impedance spectra of 0.9% NaCl electrolyte at 25°C measured by two-electrode and four-electrode method with fabricated electrode array, log-scaled impedance magnitude (a) and phase (b) vs. log-scaled frequency, spectrum measured by two-electrode method was fitted by the equivalent circuit in Fig. 5.3.

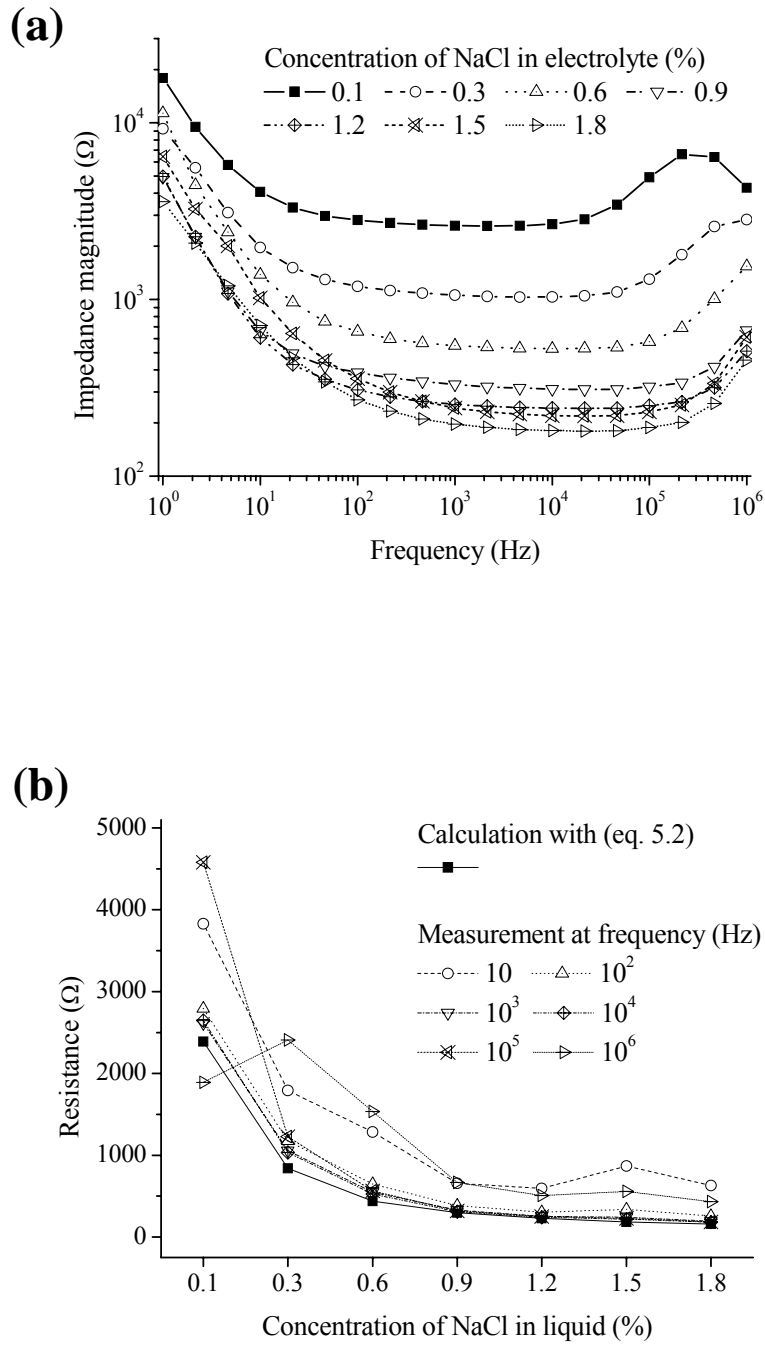


Fig. 5.10: Impedance magnitude over the frequency (a) and resistance (b) measured at different concentration of NaCl in the electrolyte (at 25°C) by four-electrode method with fabricated electrode array.

## 5.2.2 Dependence of Intravascular Impedance Measurement on Thickness of Vessel

By numerical simulations based on the quasi-vessel model of Fig. 5.4, the sensitivity fields were obtained as Fig. 5.11 for the inner radius of vessel of 0.5 (a), 1 (b), 1.5 (c), or 2 mm (d). For a given electrode structure, the simulated measurable impedance magnitude  $|Z|_{\text{app}}$  was dependent on the thickness of vessel wall (Fig. 5.12). With decreasing the thickness of vessel wall,  $|Z|_{\text{app}}$  decreased. When the thickness of vessel was above 50 % of separation distance between current electrodes, the decrease of measurable impedance magnitude  $|Z|_{\text{app}}$  was smaller than 5 % of  $|Z|_{\text{inf}}$  (impedance magnitude when the thickness of vessel is 1 cm (quasi-infinite)). The inner radius of vessel in the quasi-vessel model had no influence on the simulated  $|Z|_{\text{app}}$  (see Fig. 5.12).

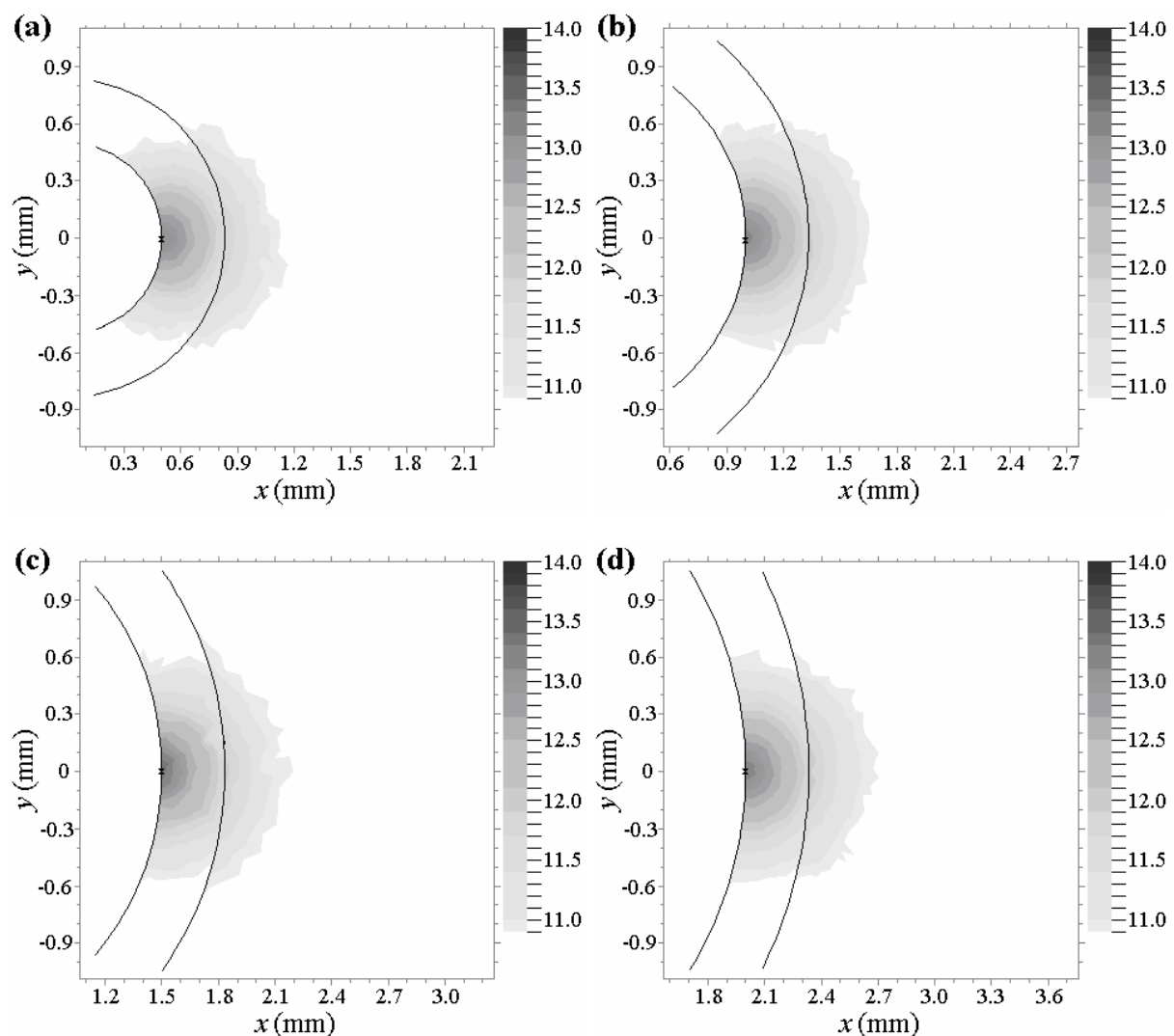


Fig. 5.11: Log of simulated sensitivities (at 10 kHz) at the middle of the electrode array on the transverse plane in the quasi-vessel model with vessel thickness of 333  $\mu\text{m}$  and with inner vessel radius of 0.5 (a), 1 (b), 1.5 (c), or 2 mm (d) (Cho and Thielecke 2005).

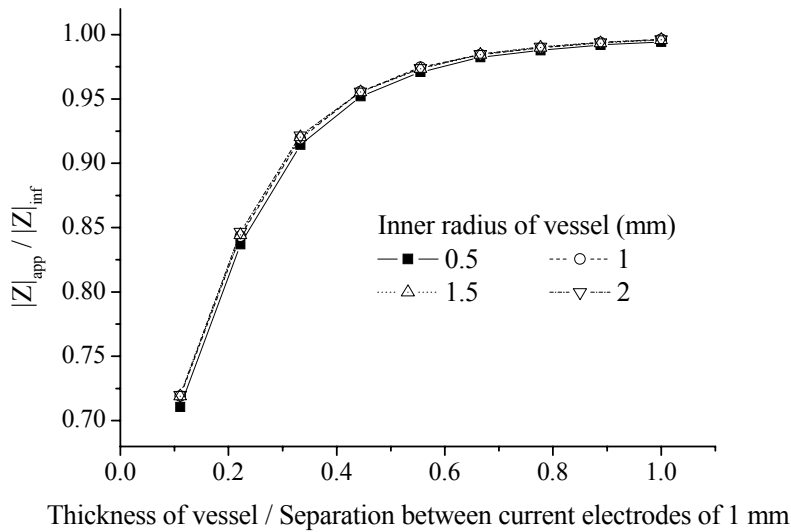


Fig. 5.12: Ratio of impedance magnitude at 10 kHz simulated at different thickness of vessel to one when the thickness of vessel is 1 cm ( $|Z|_{app}/|Z|_{inf}$ ) in the quasi-vessel model with the inner vessel radius of 0.5, 1, 1.5, or 2 mm vs. the ratio of vessel thickness to the separation distance between the outer electrodes for applying current of 1 mm.

Fig. 5.13 shows the distributions of sensitivity simulated at 10 kHz when the thickness of layer 1 in the planar two-layer model of Fig. 5.5 (a) is 333  $\mu\text{m}$  or 1 cm (quasi-infinite). When the thickness of layer 1 was 333  $\mu\text{m}$  rather than 1 cm, a higher sensitivity field was distributed between the inner two voltage sensing electrodes. The impedance measured by using the experimental setup of Fig. 5.5 (b) was depended on the level of electrolyte (see Fig. 5.14). The measured ratio of  $|Z|_{app}/|Z|_{inf}$  (impedance magnitude when the electrolyte is 1 cm (quasi-infinite)) was agreed with the simulated one. When the electrolyte thickness was above 78% of separation distance between current electrodes, the change of measured impedance magnitude in dependency of electrolyte level was below 5 % of  $|Z|_{inf}$ . With decreasing the level of electrolyte, the measured and simulated  $|Z|_{app}$  at 10 kHz increased exponentially.

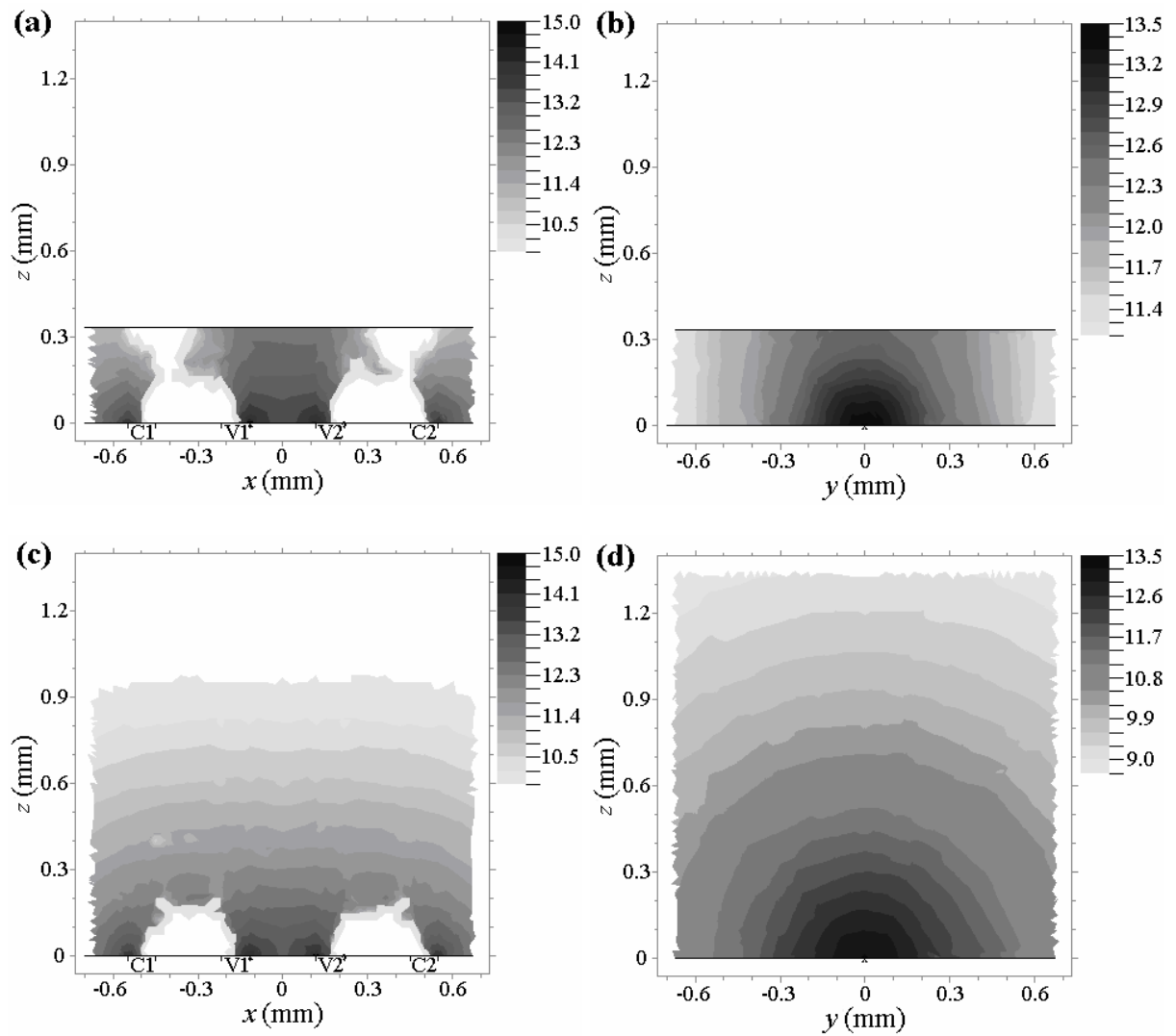


Fig. 5.13: Log of sensitivities simulated at 10 kHz in the two-layer model with the level of  $333\ \mu\text{m}$  (a and b) and semi-infinite (c and d) along the longitudinal (a and c) and transverse axis (b and d) at the middle of the electrode array. C1, C2 and V1, V2: electrode pairs for current applying and voltage measurement, respectively (Cho and Thielecke 2005).

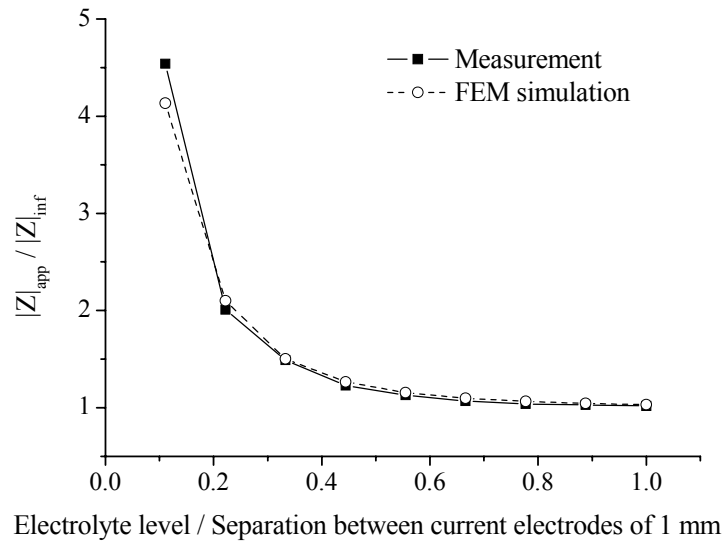


Fig. 5.14: Ratio of impedance magnitude at 10 kHz at different level of electrolyte to one when the level of electrolyte is 1 cm ( $|Z|_{app}/|Z|_{inf}$ ) in the two-layer model with respect to the ratio of the electrolyte level to the separation distance between the outer electrodes for applying current of 1 mm (Cho and Thielecke 2005).

### 5.2.3 Dependence of Intravascular Impedance Measurement on Relative Position of Plaque to Electrodes

For the atheromatous vessel model of Fig. 5.6 (a), the measurable impedance magnitudes at 1 kHz and 10 kHz in dependence on the separation angle between the electrode array and lipid  $\theta_e$  were simulated (Fig. 5.15 (a)). The magnitude of impedance had its maximum if  $\theta_e$  was  $0^\circ$ , and decreased with increasing  $\theta_e$ . When  $\theta_e$  was higher than  $25^\circ$ , the difference of simulated impedance magnitude from the impedance magnitude at a non-plaque region (e.g.  $\theta_e = 180^\circ$ ) was less than 10%. Fig. 5.15 (b) shows the impedance magnitude at 1 kHz and 10 kHz in dependence on the depth of lipid from the endothelium  $r_l$ . When  $r_l$  was higher than 0.6 mm, the difference of impedance magnitude from the impedance magnitude at a non-plaque region was less than 10%. Further, the atheromatous vessel model of Fig. 5.6 (b), the measurable impedance magnitudes at 1 kHz and 10 kHz in dependence on the longitudinal separation between the lipid and the electrode array  $z_l$  were simulated (Fig. 5.15 (c)). The magnitude of impedance had its maximum if  $z_l$  was 0 mm, and decreased with increasing  $z_l$ . When  $z_l$  was higher than 1.6 mm, the difference of impedance magnitude from the impedance magnitude at a non-plaque region was less than 10%.

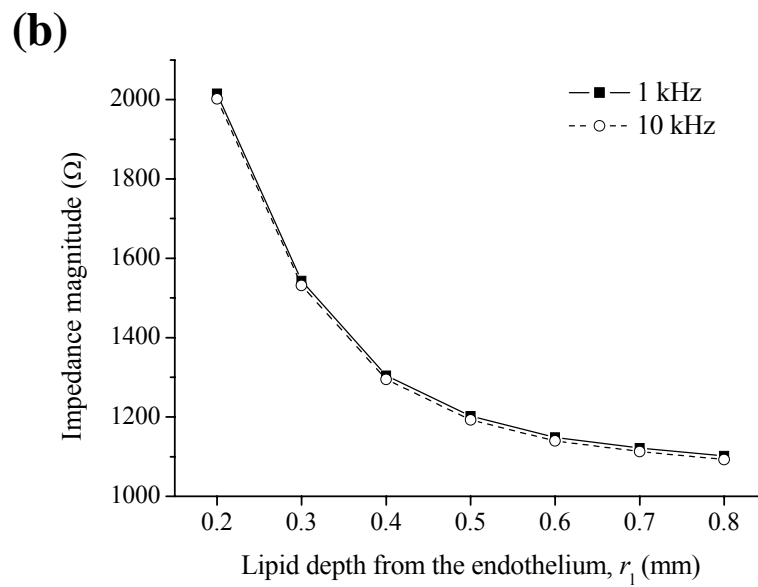
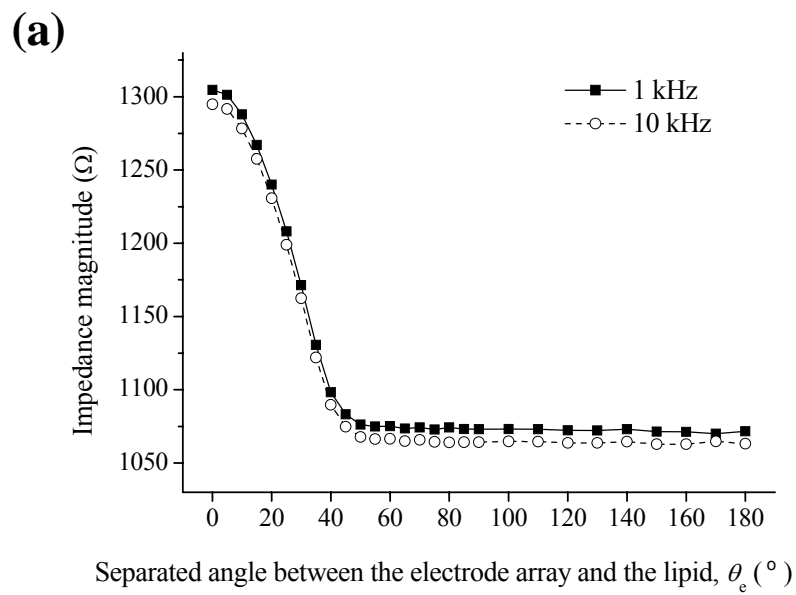


Fig. 5.15 (continued)

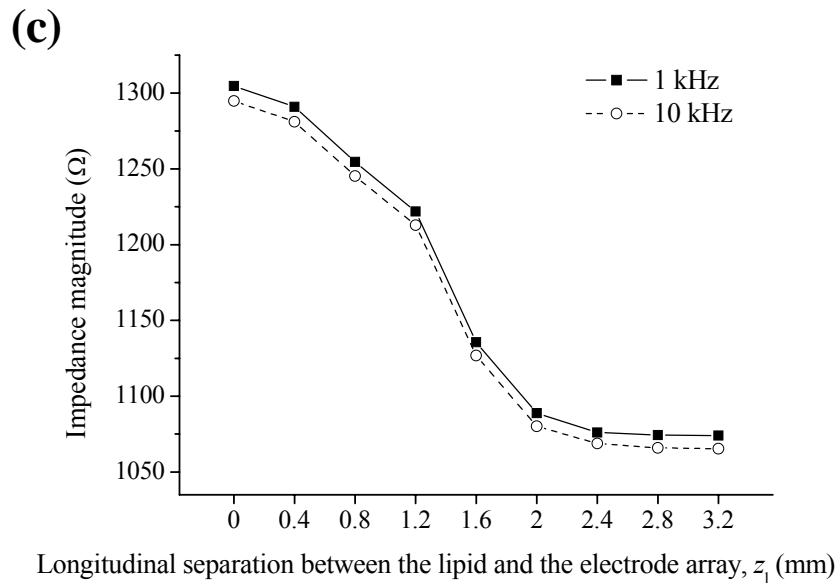


Fig. 5.15: Simulated impedance magnitude at 1 kHz or 10 kHz with atheromatous vessel model with respect to the separation angle between the electrode array and the lipid,  $\theta_e$  (a), the depth of lipid from the endothelium,  $r_l$  (b), and the longitudinal separation between the lipid with length of 2.4 mm and the electrode array,  $z_1$  (c) (Cho and Thielecke 2006).

Fig. 5.16 shows the log-scaled magnitude of current density simulated at 10 kHz on the cross section (according to Fig. 5.6 (a)) of the middle of electrode array with respect to different separation angles  $\theta_e$  in the atheromatous vessel model. When  $\theta_e$  was  $0^\circ$  and  $20^\circ$ , most of the currents were blocked by the lipid with low conductivity, and the magnitude of current density between the electrode array and the lipid was increased. At higher  $\theta_e$ , the influence of lipid on the current flow decreased. Fig. 5.17 shows the log-scaled magnitude of current density at 10 kHz on the longitudinal section (according to Fig. 5.6 (b)) of the middle axis of electrode array with respect to different  $z_1$  in the atheromatous vessel model. With decrease of  $z_1$ , the current density more distributed over the lipid with high resistivity. With increasing  $z_1$ , however, the influence of the lipid on the distribution of current decreased.

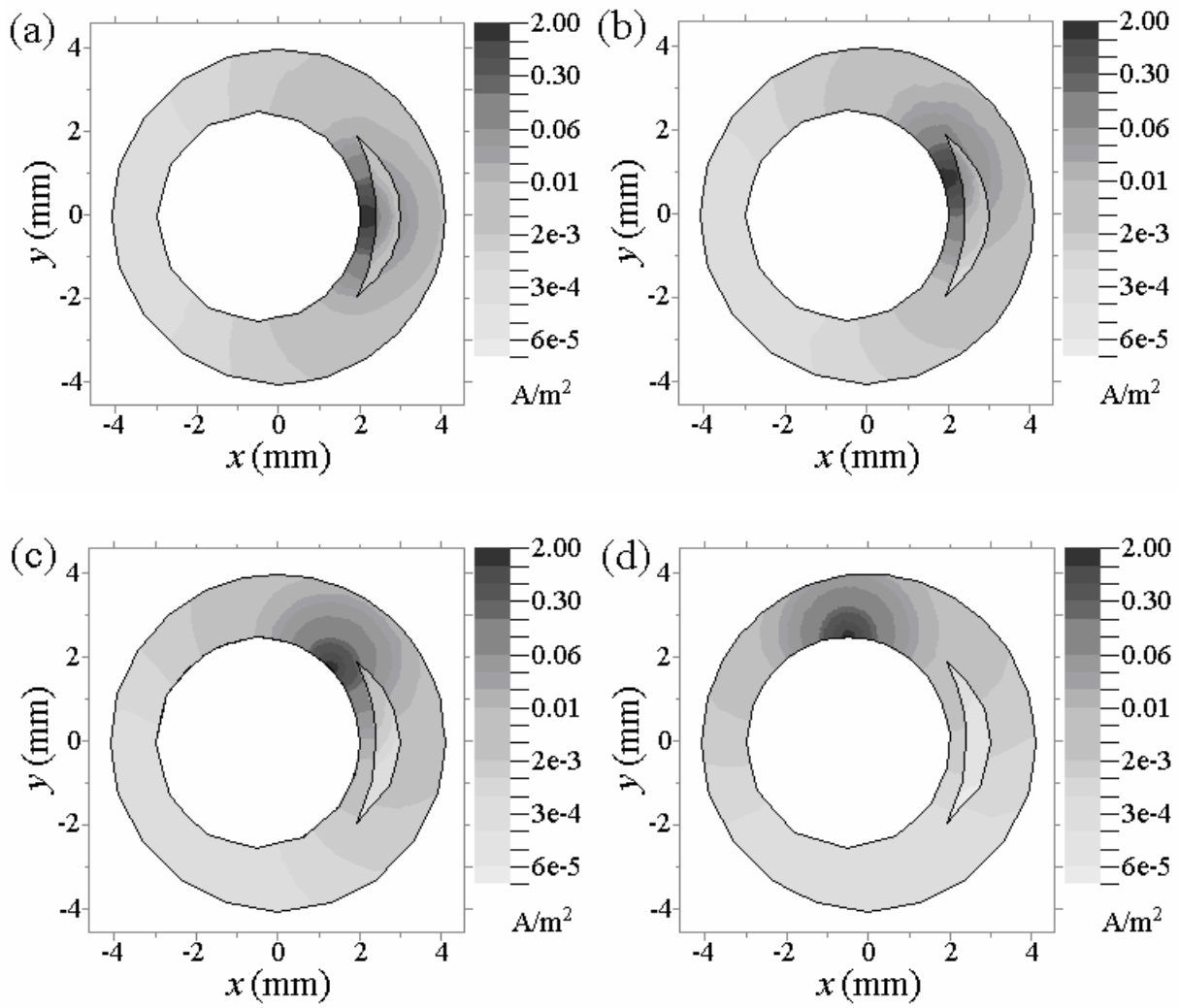


Fig. 5.16: Log-scaled magnitude of current density at 10kHz along the cross section of artery at the middle of electrode array with respect to the separation angle between the electrode array and the lipid,  $\theta_e$  (a =  $0^\circ$ , b =  $20^\circ$ , c =  $45^\circ$ , and d =  $90^\circ$ ) in the atheromatous vessel model.

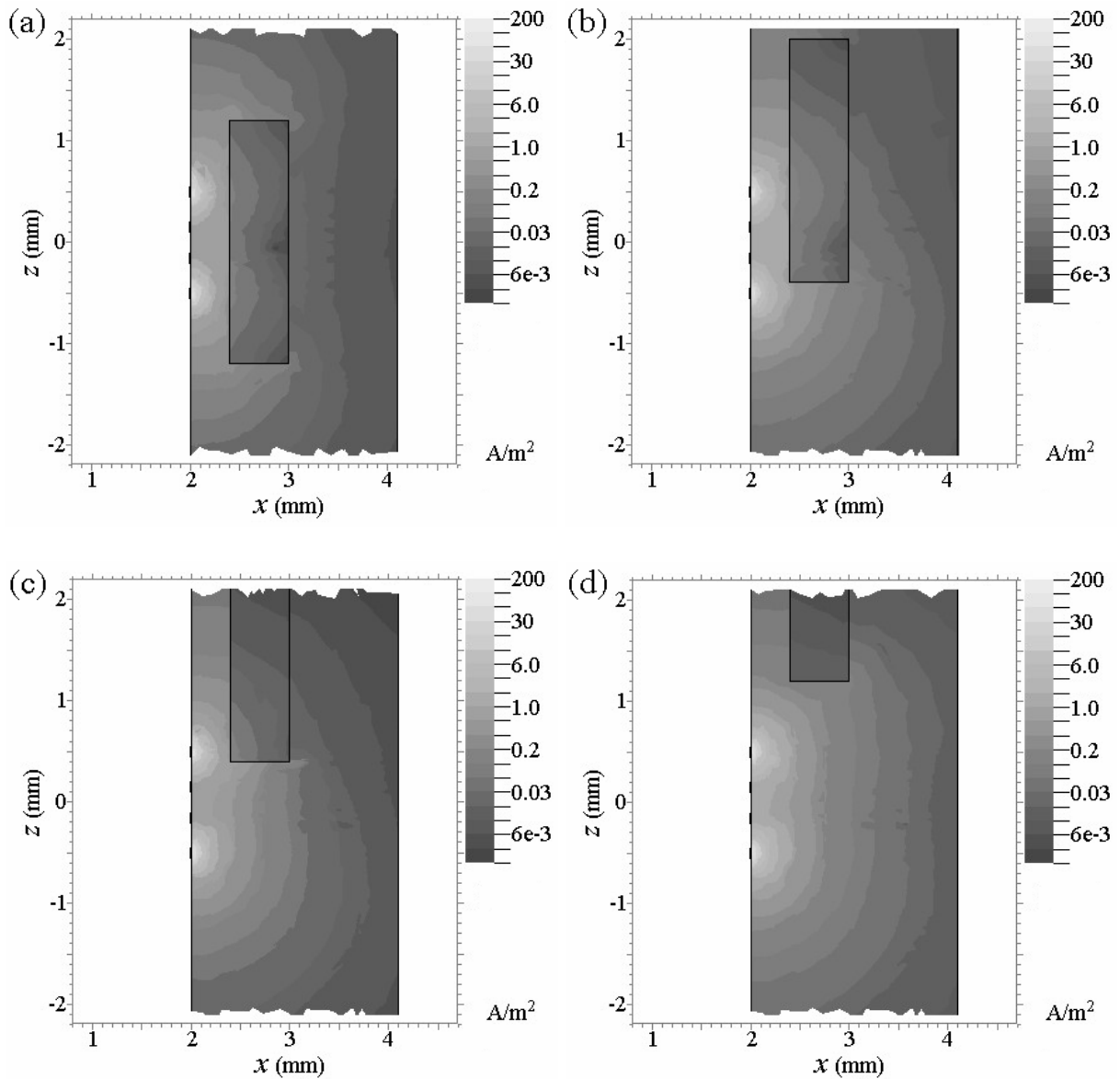


Fig. 5.17: Log-scaled magnitude of current density at 10 kHz along the longitudinal section of artery at the middle of electrode array with respect to the longitudinal separation between the lipid and the electrode array,  $z_1$  ( $a = 0$  mm,  $b = 0.8$  mm,  $c = 1.6$  mm, and  $d = 2.4$  mm) in the atheromatous vessel model.

The influence of the "short-circuiting" effect was investigated based on the setup of Fig. 5.7 (see Fig. 5.18). With decreasing the distance (arc length) between electrode arrangements, the impedance magnitude decreased. When the arc length between electrode arrangements was  $150 \mu\text{m}$  (or separation angle:  $3.4^\circ$ ), the impedance magnitude was 93.8% of the value obtained for a balloon catheter with one electrode arrangement only.

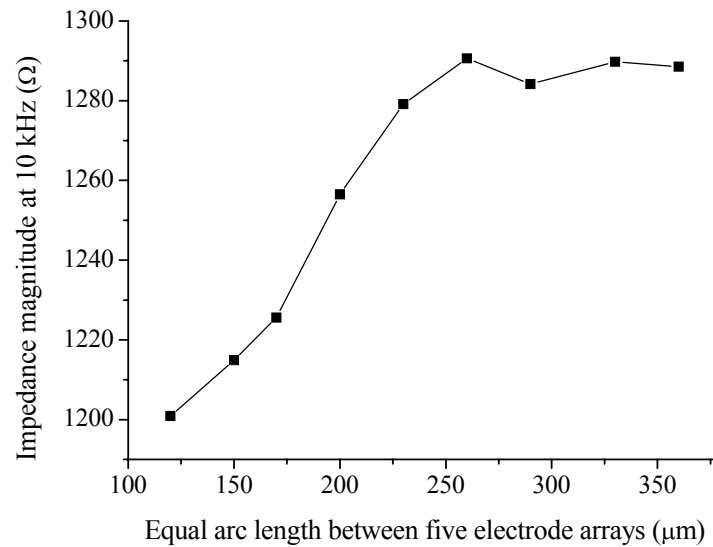


Fig. 5.18: Simulated impedance magnitude at 10 kHz for the setup in Fig. 5.7 in dependency of the distance (arc length) between the neighbored electrode arrangements (Cho and Thielecke 2006).

#### 5.2.4 Measured Impedance *in situ* and Analysis

Atherosclerotic aortas of five rabbits were investigated *in situ* by X-ray angiography, intravascular ultrasound (IVUS), IS, and histology. All angiograms and IVUS images revealed the early stages of atherosclerosis without any visible stenoses. Fig. 5.19 shows an angiogram (a), a typical IVUS image (b), and micrographs of aorta wall (c and d) of one selected animal. In dependence on the characteristic of plaques, the thickness of aortas was various from several hundreds  $\mu\text{m}$  to a few mm. The induced lipid plaques were distributed partially in the intima (indicated by right-top arrow in Fig. 5.19 (d)). Generally, the vessel walls including plaques were thicker than ones without plaques. 48 aortic segments (52%) contained a fatty or fibrous plaque formation but 44 segments (48%) showed no atherosclerosis at all. Three different groups were classified by histology. 44 segments without atherosclerotic material were identified as the group P0 (48%), whereas 12 aortic segments containing the plaques thinner than media as PI (13%). 36 segments including plaques thicker than media were characterized as group PII (39%).

Fig. 5.20 depicts the impedance measurements of all five aortas at 1 kHz and 10 kHz by using BIC. The average and standard deviation of impedance magnitude at 1 kHz and 10 kHz for the group of plaque type classified as P0, PI, or PII were shown in Fig. 5.21. The average and standard deviations of impedance magnitude at 1 kHz were  $1428 \pm 603 \Omega$  in group P0,  $1134 \pm 252 \Omega$  in group PI, and  $1141 \pm 427 \Omega$  in group PII. At 10 kHz, the average and standard deviation of impedance magnitude were  $1219 \pm 517 \Omega$  in group P0,  $996 \pm 273 \Omega$  in group PI, and  $1163 \pm 529 \Omega$  in group PII. There was statistically no significant difference between the absolute impedance magnitudes of P0, PI, and PII.

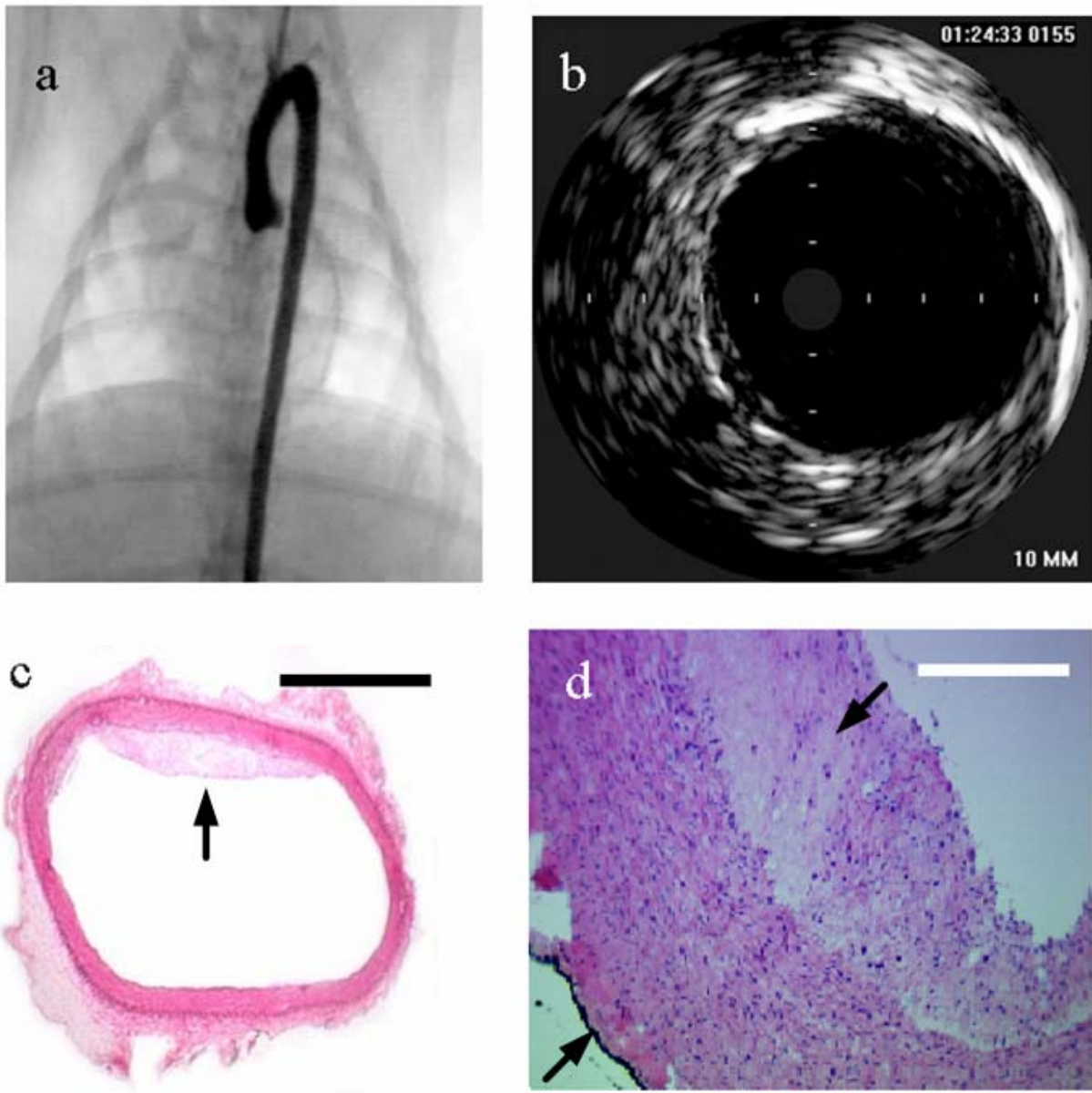
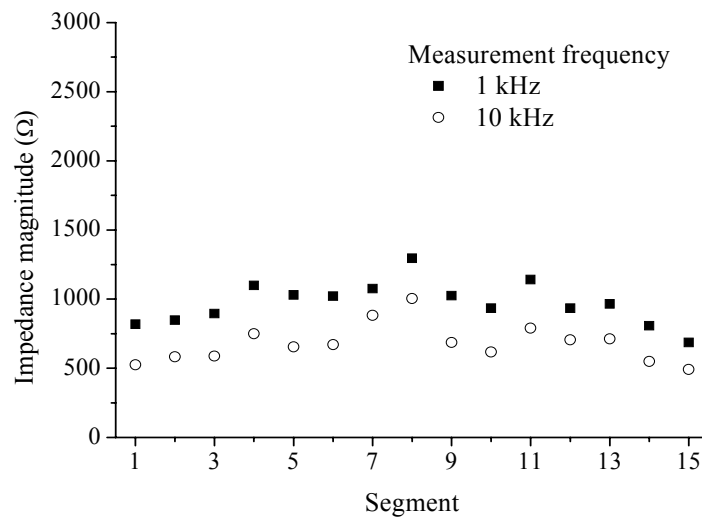
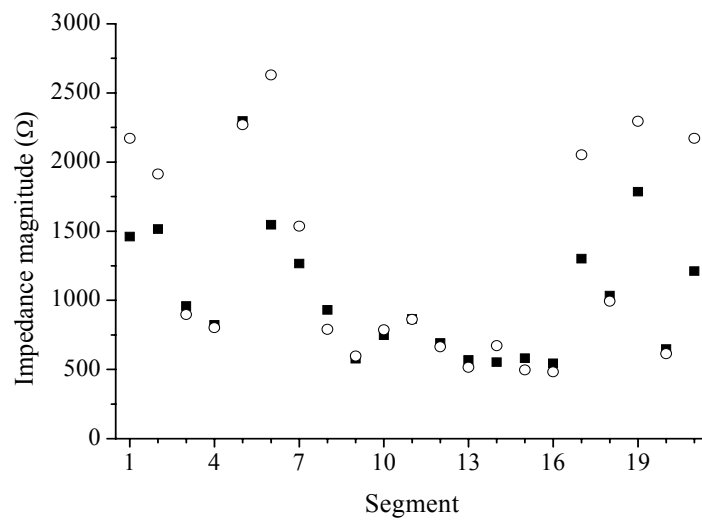


Fig. 5.19: Example of aortic angiogram (a) and intravascular ultrasound cross section image (b) of a rabbit, micrograph of an aortic segment with plaque indicated by arrow, scale bar: 2 mm (c) and an enlarged micrograph of marked vessel (left-bottom arrow) with plaque (right-top arrow), scale bar: 500  $\mu\text{m}$  (d) (Süselbeck *et al.* 2005).

Aorta 1



Aorta 2



Aorta 3

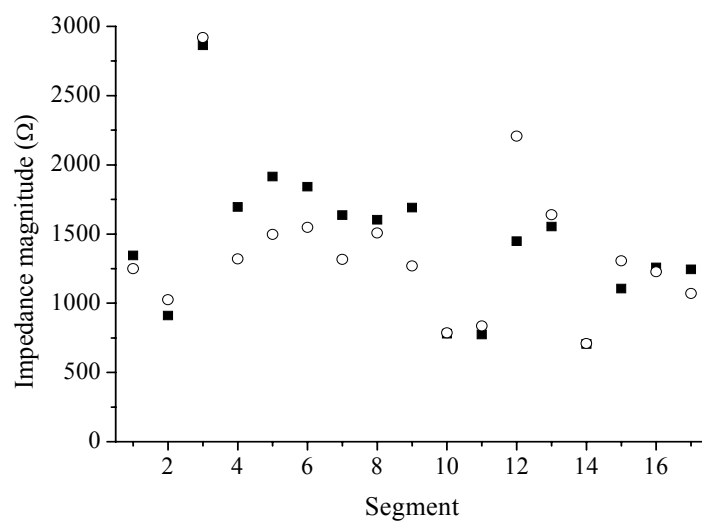


Fig. 5.20 (continued)

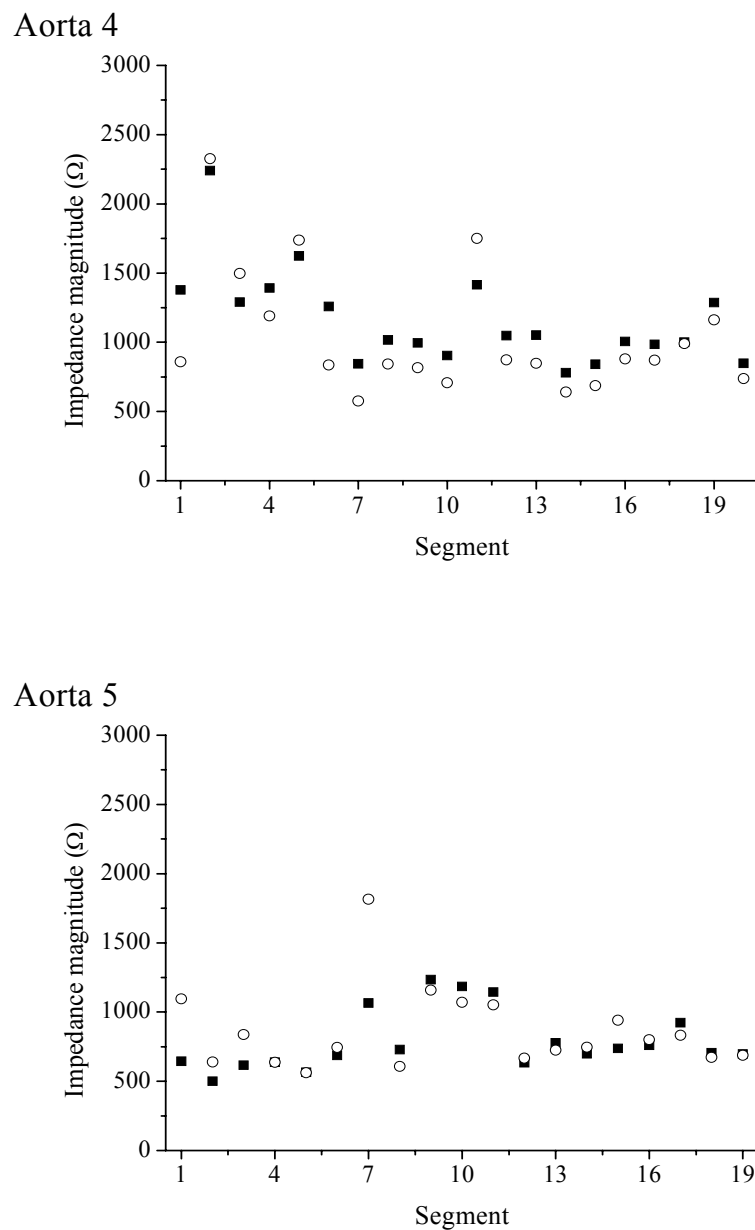


Fig. 5.20: Impedance magnitude of all aortic segments of 5 rabbits (Aorta 1 to Aorta 5) after 17 weeks of high cholesterol diet measured intravascularly at 1 kHz (■) and 10 kHz (○) recorded by using the developed balloon impedance catheter.

Fig. 5.22 shows the averages and standard errors of ICF ( $|Z|_{1\text{kHz}} - |Z|_{10\text{kHz}}$ ) analyzed for each group. The ICF of group PII ( $-22.2 \pm 43.29 \Omega$ ) was significantly lower in comparison to PI ( $137.7 \pm 53.29 \Omega$ ;  $p = 0.05$ ) and P0 ( $208.5 \pm 55.16 \Omega$ ;  $p = 0.002$ ). However, there was no difference between group P0 and PI ( $p = 0.515$ ).

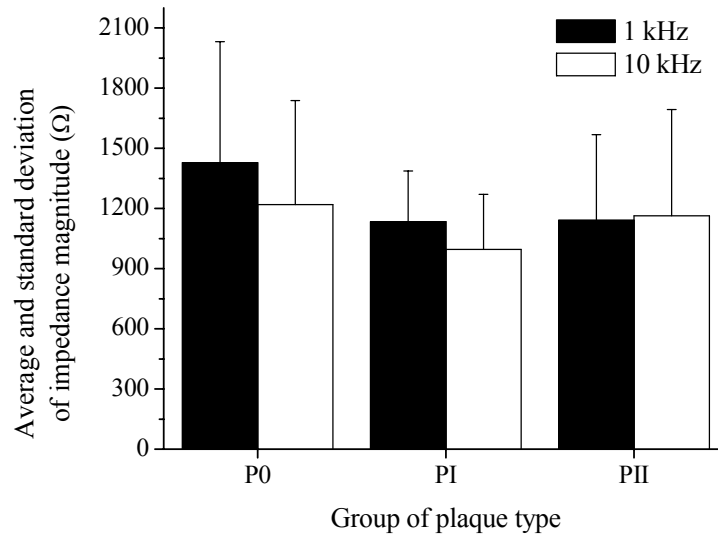


Fig. 5.21: Averages and standard deviations of measured impedance magnitudes in Fig. 5.20, classified by the thickness of plaque, P0: no plaque (n = 44), PI: plaque thinner than media (n = 12), PII: plaque thicker than media (n = 36) (Süselbeck *et al.* 2005).

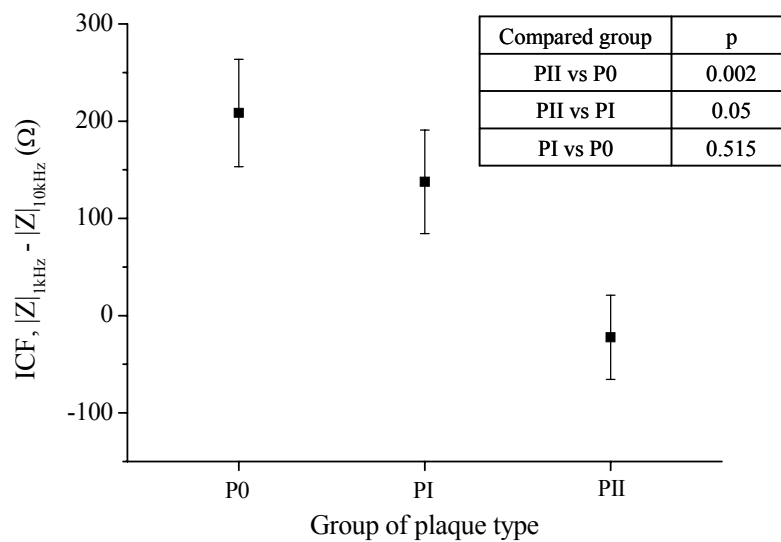


Fig. 5.22: Averages and standard errors of ICF (impedance magnitude at 1 kHz – impedance magnitude at 10 kHz) calculated from the data of Fig. 5.20 and result of hypothesis t-test, P0: no plaque (n = 44), PI: plaque thinner than media (n = 12), PII: plaque thicker than media (n = 36) (Süselbeck *et al.* 2005).

### 5.3 Discussion

The presented results demonstrate for the first time that atherosclerotic plaques are distinguishable based on impedance data recorded *in situ*. Intravascular impedance measurement under *in vivo* or *in vitro* conditions has been limited so far. The first experimental study measuring resistance of human atherosclerotic plaques was performed in an *in vitro* experiment by using a two-electrode system with a spot electrode in conjunction with a large plate electrode (Slager *et al.* 1992). In this experimental setup, different types of atherosclerotic plaque could not be differentiated by measuring the resistance only. Further experiment investigated an impedance catheter system in a human iliac artery under *in vitro* conditions by using an array of five annular electrodes. In the model, atherosclerotic plaques were imitated by small disc shaped plastic drops, which were inserted into the iliac artery. These artificial plaques could be easily detected by the impedance catheter system with four-electrode method (Konings *et al.* 1997). Recently, a computer simulation explored the feasibility of an array of four point electrodes mounted onto a balloon catheter and simulated the impedance of various lesions in vessels. The simulation results demonstrated a large difference of impedance for the various lesion morphologies (Stiles and Oakley 2003). Based on these results, a four-microelectrode structure was selected. The separation of excitation and measuring electrodes reduced the influence of the impedance of the electrode interfaces on the total measured impedance. The micro-scaling and spacing of the electrodes enabled the measurements within small areas of vessels. The highly flexible microelectrode structure of polyimide ensured an excellent electrode contact to the aortic walls. The integration of the electrodes onto a conventional coronary balloon catheter facilitated the performance of intravascular impedance measurements. In this first investigation of atherosclerotic processes, a canine animal model was used to perform IS *in situ* and to imitate the anatomical size of coronary atherosclerotic lesions. Furthermore, this experimental approach guaranteed an accurate match of histology and impedance measurement of every analysed aortic lesion. The results of this chapter are discussed in more detail below.

#### 5.3.1 Impedance Characteristics of Microfabricated Electrodes

The microfabricated electrodes were experimentally characterized. From the electrical characterization of the electrodes in electrolytes with known conductivities, it was possible to determine the impedance characteristic of the electrode in a physiological environment. In the low frequency range, the impedance measured by two-electrode method of the fabricated electrode array was governed by the electrode impedance. Since the impedance of metal/electrolyte interface decreased with increasing frequency, the resistance of electrolyte was observable when the frequency was higher than several tens kHz. However, the impedance again was decreased again at frequencies above several hundreds kHz since the high frequency current can stray. Compared with the two-electrode method, the four-electrode method was able to reduce the effect of electrode impedance on the total measured impedance and to extend the effective frequency range in which the impedance of electrolyte dominates the measured impedance. This is already the case below several tens of kHz (see Fig. 5.9). However, the increase of impedance magnitude and decrease of phase were still observed below 100 Hz. A reason for this can be the polarization of the inner electrodes for potential measurement since the current prefers the high conductive path of metal electrode

(Grimnes and Martinsen 2000). The polarization may not be uniform over the electrode surface area and may occur according to the local current direction. At a sufficient high frequency, the impedance measurements of both two- and four-electrode method were affected by parasitic components (e.g. stray capacitance, impedance of transmission lines). These electrode polarization and parasitic components disturbed the impedance measured in experiment on electrolytes with different conductivities (see Fig. 5.10). The results of Fig. 5.10 show that the impedance measurement with the fabricated electrode array of Wenner Alpha type is dominated by the sample (medium surrounding electrodes) in the frequency range of 1 kHz to 10 kHz when the impedance magnitude of the sample is 150  $\Omega$  to 3 k $\Omega$ , approximately. For this range of frequency, the fabricated electrodes are suitable for the characterization of samples with an impedance magnitude of 150  $\Omega$  to 3 k $\Omega$ .

### **5.3.2 Influence of Vessel Thickness on Intravascular Impedance Measurement**

To understand the influence of complex vessel structures and properties on the intravascular electrical characterization of vessels, it was studied how the intravascular impedance measurement is dependent on the vessel thicknesses by using the quasi-vessel model and two-layer model. The FEM simulation based on the quasi-vessel model shows that the intravascular impedance measurement of vessels is affected by the conductivity of extra vascular material when the thickness of vessel is so thin that the current density is sufficient high in the extra vascular region (see Fig. 5.11 and Fig. 5.12). The experiment based on the two-layer model (layer 1: electrolyte, layer 2: air) validated the theoretical study about the influence of vessel thickness on the impedance measurement. The impedance magnitudes measured at the different level of electrolyte agreed with those simulated by FEM. The FEM simulation of the two-layer model shows that the reflection caused by the different conductivities of two layers increases with decreasing thickness of the layer 1 and thus the impedance magnitude is increased (see Fig. 5.13 and Fig. 5.14). By aid of FEM simulation, it is therefore possible to design various configurations of electrodes to get the required measurable depth considering the thickness of vessels and to avoid the effect of extra vascular materials on impedance measurement. Reversely, if the electrical properties of vessels are distinguished from those of extra vascular materials, it is possible to determine the thickness of vessels based on impedance measurement with different configuration of electrodes. Likewise, if the electrical properties of plaques in vessels are different from those of vessels, it is possible to determine the radial distance of a plaque layer in vessels from electrodes.

### **5.3.3 Influence of Relative Plaque Position to Electrodes on Intravascular Impedance Measurement**

It was investigated how the intravascular impedance measurement with BIC is dependent on the relative positions of atherosclerotic plaque (lipid) to electrode array. The FEM simulation based on the quasi-atheromatous vessel model shows that the influence of plaque impedance on the total impedance magnitude increases with decreasing the distance of the electrode array of BIC to the lipid plaque with low conductivity (see Fig. 5.15). Thus, the impedance diagnosis of lipid plaque in vessels is dependent either on the

angular separation or the distance between the electrodes and the plaque on the longitudinal axis. Further, in real vessels, the depth of plaque from endothelium would affect the sensitivity of plaque characterization. The sensitivity of plaque characterization by using BIC is determined by how the electric fields are distributed in the vessel regarding the area of plaque (see Fig. 5.16 and Fig. 5.17). The radial field distribution can be optimized regarding the angular position of a plaque, if an impedance catheter is used which contains several concentrically positioned electrode arrangements. Simulations show under what special condition the impedance measurement of a four-electrode arrangement of Wenner Alpha type is influenced, if several electrode arrangements are positioned concentrically on the balloon of an impedance catheter. This was investigated, since too closely neighbored electrodes in arrays can affect the current flow around electrodes because of the high conductivity of the neighbored electrodes themselves (so called "short-circuiting" effect). These FEM simulations are helpful to design for a given vessel a set of electrode arrangements which has an equal separation angle or arc length between the sets of in-line electrodes to ensure the required resolution of intravascular impedance measurement. For the geometrical conditions of Fig. 5.15 (a), for example, it is inferred that the separation angle between the sets of in-line electrodes should be less than  $50^\circ$  (or arc length  $< 2.18$  mm) to ensure that the plaque would cause an impedance magnitude at at least one in-line electrode arrangement not less than 10 % in comparison to the impedance magnitude in a vessel without any plaques. On the other hand, the distance (arc length) between the in-line electrode arrangements should be larger than  $200 \mu\text{m}$  to avoid that the influence of the short-circuiting effect on the measurable impedance magnitude is larger than 3% (see Fig. 5.18).

By using a cylindrically arranged multi-electrode arrays (see Fig. 5.23), it is possible to control the sensitive area or the resolution and depth of intravascular impedance measurement. Further, an intravascular impedance imaging with multi-electrode arrays is

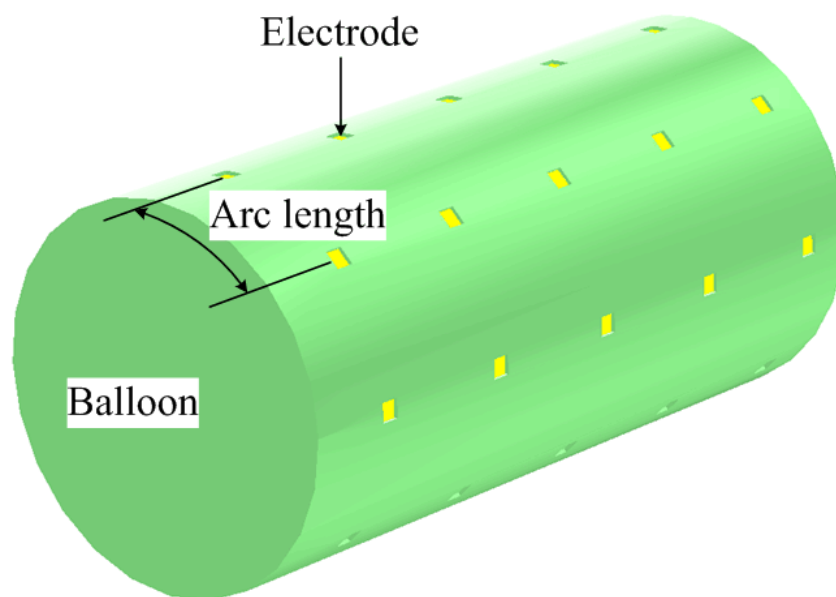


Fig. 5.23: Schematic of balloon catheter with multi-electrode arrays for controlling the distribution of electric fields intravascularly.

possible by using algorithms for the reconstruction of distribution of conductivities based on measured impedances (impedance tomography, Holder 2005).

### 5.3.4 Intravascular Electrical Characterization of Atherosclerotic Plaque in Vessel Walls

For the intravascular impedance measurements of arteries, the four-electrode method with separated excitation and measuring electrodes was chosen to reduce the influence of electrode interfacial impedance on the total measured impedance. The small size and spacing of the microelectrodes enabled impedance measurement within the aortas of rabbits used for the animal model. The high flexible microelectrode structures based on polyimide ensured a durability of balloon catheter and excellent electrode contacting to the aortic wall. The developed BIC facilitated to perform the intravascular impedance measurement. It was not possible to distinguish the segments of vessels with plaques from the segments without plaques by comparing the raw data of impedance magnitude. This can be explained by the influence of the vessel thickness on the measured impedance. The ICF analysis enabled the minimization of the influence of different vessel thickness on the measured impedance and the differentiation of segments with plaque from segments without plaque (see Fig. 5.22). This is due to the fact that the impedance of fatty plaques is constant over the relevant frequency range, but the impedance of muscle tissue decreases with increasing frequency. Therefore, it is expected that diagnosis based on ICF analysis is also valid in clinical *in vivo* applications if the extra vascular material has the constant conductivity versus the frequency change. If the environment of the investigated vessels is not constant regarding the electrical properties, the geometry of the used electrode arrangement must be adapted to the thickness of vessel wall in that way that the current field is limited mainly to the wall of vessel. It was anticipated that vessel damages might constitute an important limitation of the technique itself since BIC requires a close tissue contact. Alterations induced by the BIC were not able to be either quantified or excluded in this investigation. However, when the balloon expansion was limited to a maximum pressure of 0.5 atm in this experiment, the histological investigation demonstrated non-relevant trauma of the neointima. For the future work, it will be investigated whether the different plaques of human aortas can be characterized by IS. Further, the practical use of BIC under *in vivo* models should be investigated.

In this chapter, it was reported that the intravascular impedance measurement of atherosclerosis is determined not only by the different thickness of vessel but also by the relative position of plaque to electrodes. From the *in situ* animal experiments, it was shown that the BIC is feasible for the intravascular impedance measurement of vessels and that the atherosclerotic plaques with low conductivity can be electrically characterized by ICF analysis. Due to the dependence of intravascular impedance measurement on the different vessel thickness and relative position of plaques to electrodes, it is necessary to control the distribution of electric fields in vessels to get the high sensitivity for the detection of atherosclerotic plaques. For this, in future work, it should be investigated to use multi-electrode arrays of BIC for the control of electric fields in vessels and also for the intravascular imaging of electrical properties. Further, the use of BIC will be studied on atherosclerotic human models *in vivo*. Finally, it is expected that the electrical characterization with BIC can be combined with existed diagnoses to improve the diagnosis of atherosclerosis.

## 5.4 Conclusions

In this chapter, it was investigated which side conditions are necessary for a sensitive impedance measurement on vessel walls and whether reproducible impedance measurements can be performed in vessels *in situ*. A balloon impedance catheter (BIC) with integrated flexible microelectrodes was used for experimental investigation *in vitro* and *in situ*, and considered for theoretical investigations respectively. The influence of extra vascular conditions and the relative position of electrodes to the plaque on the intravascular impedance measurement of vessel walls were studied systematically by using quasi-vessel models and numerical finite element method (FEM) simulation. For the first time, it was successfully demonstrated that aortas including fatty plaques are distinguishable from normal ones by intravascular impedance analysis with a developed BIC. The influence of extra vascular conditions on the impedance measurement using a given microelectrode configuration was studied. From the experiment using a two-layer model and FEM simulation, it was shown that the measured impedance is dependent on the relative thickness of vessel wall to the electrode configuration, and therefore that the configuration of electrode arrays should be optimized to minimize the undetermined extra vascular conditions *in vivo*. Intravascular impedances in the atherosclerotic rabbits were measured. To solve the problem about the influence of different thickness of vessel walls on impedance measurement, a parameter – impedance change versus frequencies (ICF) – was derived. By histological studies, the cross sections of aortic segments including fatty plaques were significantly distinguished from normal. The sensitivity of impedance diagnosis with respect to the relative position of electrode array to the plaque in vessels was investigated by FEM. To solve the lack of resolution, a set of multi-electrode arrays was considered. Further, it was simulated that the short circuiting effect is occurred when the high conductive electrodes are neighbored closely in the set. FEM simulation supported the optimal design of electrode arrangements for the intravascular impedance diagnosis of atherosclerosis.

## 6 General Discussion

In this thesis a method and a measurements system based on a balloon catheter with integrated microelectrodes were developed for the diagnosis and therapy monitoring of atherosclerosis.

The use of IS for the diagnosis and therapy monitoring of atherosclerosis requires to understand how the changes of tissue parameter on cellular level can be characterized by IS. The theoretical and experimental investigations to understand basically the influence of cellular parameter on the tissue impedance are based on a single cell/micro hole model in this thesis. To investigate the influence of single cell behaviours (e.g. physiological and morphological change of cells, cell/substrate gap) on impedance measurements experimentally, it needs to decrease the size of transducers used for impedance measurement to the size of a cell. Impedance measurements with microelectrodes adapted to the size of single cells can not be performed with a high sensitivity, since a high impedance of the electrode/electrolyte interface. By using the single cell/micro hole model, the use of a microelectrode is avoided for impedance measurements on a single cell. Numerical simulations based on the single cell/micro hole model show that the passive electrical characteristic of single cells is determined by the cellular shape or cell/substrate gap at the hole interface due to the cell membrane with low conductivity but not by the intracellular conditions. From the results, it is found that the impedance measurement of cells on the hole is strongly determined by the cellular coverage and membrane integrity. Therefore, it is expected that the changes in the corresponding parameters of tissues (e.g. cellular shape, membrane integrity, or extra cellular space) affect the electrical characteristics of tissues and that IS can be used to characterize electrical effects of atherosclerosis related to these parameters. However, real biological tissues are not a distribution of single cells. In biological tissues the cells interact. The interaction of cells can not be represented by a single cell model.

To include cell/cell interaction, models based on cell assemblies or tissues are required. In 2D *in vitro* models, it is investigated whether the accumulation of fat cell in cell assemblies and the disruption of cell assemblies can be determined by IS. The quantification of fat cells and characterization of cell assemblies regarding disruptions are important precondition for the use of IS in diagnosis of plaques and therapy monitoring of atherosclerosis. An accumulation of fat cells in tissue and the disruption of cell layer are characteristic for atherosclerotic plaques. In this thesis, the effect of an accumulation of fat cells on measured impedance is investigated basically *in vitro* by using the adipogenic differentiation of stem cells as a model. To investigate how sensitively pathologic degeneration processes in cell assemblies can be determined by IS, a virus infection and cytotoxic model are used. The experimental results show that the cellular alterations in cell assemblies on atherosclerotic pathology (e.g. disruption of cell layer by virus infection, accumulation of fat cells) are well reflected in the impedance measurement. Based on these results, it is expected that cellular alterations in vessels related with atherosclerosis can be electrically characterized by IS. For the intravascular electrical characterization of atherosclerosis, however, it needs to understand the influence of complex structures and properties of vessel walls on impedance measurements.

Therefore, it is investigated in this thesis which side conditions are necessary for a sensitive impedance measurement on vessel walls and whether reproducible impedance measurements can be performed in vessels *in situ*. The intravascular impedance

measurement is affected by different thicknesses of cell layers and relative positions of atherosclerotic plaques in vessels to electrodes. The numerical simulations show that these unwanted effects can be minimized if the electrode arrangements are adapted to the conditions of the vessels. Therefore, the electrode arrangements must be optimized regarding measurement sensitivity in the plaque area, short circuiting effect, and certain resolution.

A developed impedance balloon impedance catheter (BIC) with integrated flexible microelectrodes was used *in situ* on an atherosclerotic animal model. The results demonstrate for the first time that atherosclerotic plaques are distinguishable based on impedance data recorded *in situ*. Intravascular impedance data of arteries recorded under *in vivo* or *in vitro* conditions are limited so far. The first experimental study measuring resistance of human atherosclerotic plaques was performed in an *in vitro* experiment by using a two electrode system with a spot electrode in conjunction with a large plate electrode (Slager *et al.* 1992). In this experimental set up, different types of atherosclerotic plaques could not be differentiated by measuring the resistance only. Further experiments investigated an impedance catheter system in a human iliac artery under *in vitro* conditions by using an array of five-annular electrodes. In this model, atherosclerotic plaques were imitated by small disc shaped plastic drops, which were inserted into the iliac artery. These artificial plaques could be easily detected by the impedance catheter system with four-electrode method (Konings *et al.* 1997). Recently, a computer simulation explored the feasibility of a four-point electrode mounted onto a balloon catheter and simulated the impedance of various lesions in vessels. The simulation results demonstrated a large difference of impedance for the various lesion morphologies (Stiles and Oakley 2003). Based on these results, a four-microelectrode structure was selected. The separation of excitation and measuring electrodes reduced the influence of the impedance of the electrode interfaces on the total measured impedance. The highly flexible microelectrode structures of polyimide ensured an excellent electrode contact to the aortic walls. The integration of the electrodes onto a conventional coronary balloon catheter facilitated the performance of intravascular impedance measurements. In this first investigation of atherosclerotic processes, a canine animal model was used to perform IS *in situ* and to imitate the anatomical size of coronary atherosclerotic lesions. Furthermore, this experimental approach guaranteed an accurate match of histology and impedance measurement of every analysed aortic lesion.

Under *in vivo* conditions, however, the plaque position and the vessel thickness/extra vascular condition are not predetermined. To avoid the dependence of intravascular impedance measurement on the thickness of vessels/extra vascular condition and on the relative position of plaques to electrodes, it is necessary to control the distribution of electric fields in vessels by using multi-electrode arrays for BIC. Further, it needs to investigate whether the atherosclerotic plaque of human can be characterized according to the degree of lesion, and whether the intravascular impedance measurement can be used in combination with other diagnostic methods e.g. X-ray angiography, IVUS. Further, a combined medical device comprising electrodes for intravascular impedance and sensors for ultrasound imaging can be fabricated.

## 7 Summary

Chronic diseases led by cardiovascular disease are the largest cause of death in the world and the number of people dying from heart disease and stroke is increasing (Yach *et al.* 2004). The main cause of heart attack or stroke is atherosclerosis, a chronic disease affecting the arterial blood vessel and forming multiple plaques within the arteries (Stary *et al.* 1995). The goal of this thesis was the development of a method and a measurements system based on a balloon catheter with integrated microelectrodes for the diagnosis and therapy monitoring of atherosclerosis. Therefore, the following questions were addressed:

1. how changes of tissue parameter on the cellular level can affect the measured impedance,
2. whether cellular alteration related to atherosclerosis can be characterized by IS,
3. which side conditions are necessary for a sensitive impedance measurement on vessels walls,
4. whether reproducible impedance measurements can be performed in vessels under *in situ* conditions.

For 1 – To understand basically how the change of tissue parameter on cellular level can be characterized electrically by IS – the theoretical and experimental investigations were based on a single cell/micro hole model. To understand the electrical properties of single cell/micro hole model, the current density and impedance of the micro hole/cell were investigated by FEM simulation. From the simulation, it was found that the impedance of single cell/hole model is dependent on the cellular shape or cell/substrate gap rather than on the intra cellular conditions. The cell/substrate gap of the single cell/hole model corresponds to the extra cellular space of a tissue. For the experiments with a single cell/hole model, a cell was positioned on a hole of a micro fabricated chip. The measured impedance of single cell/micro hole model corresponded to the theoretical investigations. Furthermore, it was investigated by using small concentration of DMSO whether changes of membrane properties are reflected in the measurable impedance. The results indicate that changes in the tissue parameters on the cellular level like cellular shape and membrane integrity affect the electrical characteristics of tissues and that IS can be used to characterize electrically effects of atherosclerosis related to these parameters.

For 2 – It was investigated whether the disruption of cells or accumulation of adipocytes involved with atherosclerotic pathology can be electrically characterized by IS. Therefore an experimental *in vitro* approach based on a planar electrode chip was chosen to ensure reproducible and controllable conditions. To understand how alterations of cell assemblies on electrodes are reflected in the measured impedance, numerical simulations were performed. The simulations showed that the extra cellular space (cell/substrate or cell/cell gap) determines the impedance in the low frequency range. However, the high frequency electric fields were able to penetrate the cell membrane and to reveal the passive cell membrane capacitance. Using a fabricated electrode-based chip, the impedance spectra of Vero cells were measured during the HSV virus-induced disruption of cell layers. The behaviours of Vero cells during the HSV infection were clearly reflected

in the impedance analysis. This finding demonstrates that the disintegration of cell assemblies can be monitored and quantified by IS. Therefore, the parameters, which are related to the cell/cell and cell substrate gap respectively, should be determined. Further, it was investigated whether the accumulation of fat in cells and the influence on cell differentiation are determinable by IS on cell assemblies. The fat accumulation was investigated by using the differentiation of hMSCs into the adipogenic direction and the possibility of monitoring the influence on cell differentiation was investigated by effecting the adipogenic differentiation with an active substance with known effect (chloropyrifos). The experimental results showed that the cellular alterations in cell assemblies on atherosclerotic pathology (e.g. disruption of cell layer by virus infection, accumulation of fat cells) are well reflected in the impedance measurement. Considering the experimental results, it is expected that IS can be used to characterize electrically the cellular alterations in vessels related with atherosclerotic pathology (e.g. disruption of cell layers, accumulation of fat cells) for the improvement of intravascular diagnosis and therapy monitoring against atherosclerosis.

To address the questions 3 and 4 – a balloon impedance catheter (BIC) with integrated flexible microelectrodes was used for experimental investigation *in vitro* and *in situ* and considered for theoretical investigations respectively. It was investigated which side conditions are necessary for a sensitive impedance measurement on vessel walls and whether reproducible impedance measurements can be performed in vessels *in situ*. The influence of extra vascular conditions and the relative position of electrodes to the plaque on the intravascular impedance measurement of vessel walls were studied systematically by using quasi-vessel models and numerical FEM simulations. For the first time, it was successfully demonstrated that aortas including fatty plaque are distinguished from normal ones by intravascular impedance analysis with a developed BIC. The influence of extra vascular conditions on the impedance measurement using a given microelectrode configuration was studied. From the experiment using a two-layer model and the FEM simulation, it was shown that the measured impedance is dependent on the relative thickness of vessel wall to the electrode configuration, and therefore that the configuration of electrode arrays should be optimized to minimize the undetermined extra vascular conditions. Intravascular impedances in the atherosclerotic rabbits were measured. To solve the problem about the influence of different thickness of vessel walls on impedance measurement, a parameter – the impedance change versus frequencies (ICF) – was derived. By histological studies, the cross sections of aortic segments were observed. From the analysis of ICF and histological pictures, the aorta segments including fatty plaques were significantly distinguished from normal segments. The sensitivity of impedance diagnosis with respect to the relative position of electrode array to the plaque in vessels was investigated by FEM simulation. To solve the lack of resolution, a set of multi electrode arrays was considered. Further, it was simulated that the short circuiting effect is occurred when the high conductive electrodes are neighbored closely in the set. FEM simulation supported the optimal design of electrode arrangements for the intravascular impedance diagnosis of atherosclerosis.

## 8 Zusammenfassung

Chronische Krankheiten sind die häufigste Todesursache in der Welt. Bei den chronischen Erkrankungen mit Todesfolge sind die kariovaskulären Erkrankungen und die Schlaganfälle mit steigender Tendenz führend (Yach *et al.* 2004). Die Hauptursache von Herzinfarkten und Schlaganfällen ist die Arteriosklerose, eine chronische Krankheit der arteriellen Blutgefäße, die zu Ablagerungen innerhalb der Arterien führt (Stary *et al.* 1995). Ziel dieser Arbeit war die Entwicklung einer Methode und eines Messsystems zur Diagnose und Therapie der Arteriosklerose, die auf einem Ballonkatheter mit integrierten Mikroelektroden basieren. Dabei wurden untersucht

1. wie Änderungen der Gewebeparameter auf Zellebene die gemessene Impedanz beeinflussen,
2. wie zelluläre Veränderungen, die für die Atherosklerose relevant sind, mittels IS charakterisiert werden können,
3. welche Randbedingungen notwendig sind, um eine Impedanzmessung an den Gefäßwänden mit hoher Empfindlichkeit durchzuführen und
4. unter welchen Bedingungen reproduzierbare Impedanzmessungen in Gefäßen *in situ* durchgeführt werden können.

Zu 1: Um grundsätzlich zu verstehen, wie die Änderung der Gewebeparameter auf Zellebene elektrisch mit Hilfe der IS charakterisiert werden kann – erfolgten theoretische und experimentelle Untersuchungen auf Basis eines Einzelzell/Mikroloch-Modells. Die elektrischen Eigenschaften des Einzelzell/Mikroloch-Modells wurden mit Hilfe von numerischen Simulationen relevanter Stromdichten und Impedanzen theoretisch untersucht. Aus den Simulationen war ersichtlich, dass die Impedanz des Einzelzell/Mikroloch-Modells eher von der Zellmorphologie und vom Zell/Substrat-Abstand abhängt, als von den intrazellulären Bedingungen. Der Zell/Substrat-Abstand des Einzelzell/Mikroloch-Modells entspricht dem extrazellulären Raum eines Gewebes. Für die Experimente mit dem Einzelzell/Mikroloch-Modell wurde eine Zelle auf dem Loch eines Mikrochips platziert. Die gemessene Impedanz des Einzelzell/Mikroloch-Modells entsprach den theoretischen Untersuchungen. Weiterhin wurde mit Hilfe geringer Konzentrationen von DMSO untersucht, ob sich eine Änderung der Membraneigenschaften in den gemessenen Impedanzen widerspiegelt. Die Ergebnisse zeigen, dass Änderungen der Gewebeparameter auf Zellebene (wie z. B. Zellform und Membranintegrität) die messbaren elektrischen Eigenschaften der Gewebe beeinflussten und dass die IS zur Charakterisierung von entsprechenden Atherosklerose-bedingen Änderungen von Zellparameter verwendet werden kann.

Zu 2: Es wurde untersucht, ob ausgewählte Vorgänge, die mit der atherosklerotischen Pathologie im Zusammenhang stehen, mittels IS charakterisiert werden können. Die Untersuchungen erfolgten sowohl für die Zersetzung von Zellen in Zellverbänden als auch für die Anreicherung von Adipozyten in Zellverbänden. Um für die experimentellen Untersuchungen reproduzier- und kontrollierbare Bedingungen zu gewährleisten, kam in einem *in vitro*-Ansatz ein planarer Elektrodenchip zum Einsatz. Zur Erklärung, wie sich Änderungen der Zellverbände in den gemessenen Impedanzen widerspiegeln, wurden numerische Simulationen durchgeführt. Die Simulationen zeigten,

dass der extrazelluläre Raum (Zell/Substrat oder Zell/Zellabstand) die Impedanz bei niedrigen Frequenzen bestimmt. Jedoch konnten bei hohen Frequenzen die kapazitiven Eigenschaften der Zellmembranen bestimmt werden. Die Impedanzspektren von Vero-Zellverbänden wurden vor und nach HSV-Virusinfektionen aufgenommen. Die virusinduzierten Effekte auf die Vero-Zellverbände spiegeln sich deutlich in den Impedanzdaten wider. Dieses Ergebnis zeigt, dass die Auflösung und Störung von Zellverbänden mittels IS überwacht und bestimmt werden können. Weiterhin wurde untersucht, ob die Anreicherung von Fettzellen in Zellverbänden und Einflüsse auf die Zelldifferenzierung mit Hilfe der IS bestimmt bestimmbar sind. Die Fettanreicherung wurde mit Hilfe der adipogenen Differenzierung humaner mesenchymaler Stammzellen untersucht. Zur Untersuchung der Bestimmbarkeit von Einflüssen auf die Zelldifferenzierung wurde die adipogene Differenzierung durch einen Wirkstoff mit bekanntem Effekt (Chloropyrifos) beeinflusst. Die experimentellen Ergebnisse zeigen, dass sich Veränderungen in Zellverbänden bei atherosklerotischer Pathologie (z. B. Störung der Zellverbände durch Virusinfektionen, Anreicherung von Fettzellen) in den Impedanzmessungen widerspiegeln. In Anbetracht der experimentellen Ergebnisse kann erwartet werden, dass die IS zur Charakterisierung der arteriosklerotischen Veränderungen in Blutgefäßen (Ansammlung von Fettzellen, Störungen in Zellverbänden) genutzt und zur Verbesserung der intravaskulären Diagnostik und Therapieüberwachung beitragen kann.

Um die Untersuchungen zu den Punkten 3 und 4 durchzuführen, kam für in vitro und in situ Experimente ein Ballonimpedanzkatheter mit integrierten flexiblen Mikroelektroden zum Einsatz. Die theoretischen Untersuchungen basierten ebenfalls auf den Ballonkatheter-Ansatz. Es wurde untersucht, welche Randbedingungen für Impedanzmessungen an Gefäßwänden mit hoher Empfindlichkeit notwendig sind und ob Impedanzmessungen in Gefäßen reproduzierbare unter in situ Bedingungen durchgeführt werden können. Der Einfluss der extravaskulären Bedingungen und der Relativposition der Elektroden zu den arteriosklerotischen Veränderungen in den Gefäßen wurde systematisch mit Hilfe von quasi-Gefäß-Modellen und numerischen FEM-Simulationen untersucht. Zum ersten Mal wurde erfolgreich gezeigt, dass Aorten mit Fettablagerungen mittels intravaskuläre Impedanzanalysen von normalen unterschieden werden können. Der Einfluss der extravaskulären Umgebung auf Impedanzmessungen wurde mit Hilfe eines Zwei-Schicht-Modells untersucht. Die Experimente mit einem Zwei-Schichten-Modell und die Untersuchungen auf Basis von FEM-Simulationen zeigten, dass die gemessene Impedanz von dem Verhältnis der Dicke der Gefäßwände zur Größe der Elektrodenkonfiguration abhängt und dass deshalb zur Minimierung unbestimmter Einflüsse die Konfiguration der Elektroden für eine gegebene Gefäßwanddicke optimiert werden muss. Impedanzen wurden in situ intravaskulär an atherosklerotischen Kaninchen gemessen. Auch dabei zeigte sich, dass unterschiedliche Gefäßwanddicken die Impedanzmessungen beeinflussen können. Um dieses Problem zu lösen, wurde ein Parameter ICF eingeführt, der aus der Differenz von an verschiedenen Frequenzen gemessenen Impedanzbeträgen gebildet wird. Die Ergebnisse der Impedanzanalyse wurden mit histologischen Untersuchungen an Aortensegmente korreliert. Mit Hilfe der ICF-Impedanz-Analyse wurden die Aortenbereiche mit fetthaltigen Plaques von den normalen Bereichen unterschieden werden. Weiterhin wurde theoretisch untersucht und diskutiert wie sich im klinischen Einsatz bei intravaskulären Impedanzmessungen eine hinreichende Ortsauflösung erreichen lässt.

## 9 Publications related with Thesis

### Journals

1. **Cho, S.**, Castellarnau, M., Samitier, J., Thielecke, H.: "Dependence of impedance of embedded single cells on cellular behaviour". *Sensors* **8**, 1198-1211 (2008).
2. **Cho, S.**, Thielecke, H.: "Micro hole based cell chip with impedance spectroscopy". *Biosensors and Bioelectronics* **22**, 1764-1768 (2007).
3. **Cho, S.**, Becker, S., Briesen, H., Thielecke, H.: "Impedance monitoring of herpes simplex virus-induced cytopathic effect in Vero cells," *Sensors and Actuators B: Chemical* **123**, 978-982 (2007).
4. **Cho, S.**, Thielecke, H.: "Influence of the electrode position on the characterisation of artery stenotic plaques by using impedance catheter". *IEEE Trans. Biomed. Eng.* **53**, 2401-2404 (2006).
5. **Cho, S.**, Thielecke, H.: "Design of electrode array for impedance measurement of lesions in arteries". *Physiological Measurement* **26**, S19-S26 (2005).
6. Süselbeck, T., Thielecke, H., Koechlin, J., **Cho, S.**, Weinschenk, I., Metz, J., Borggreffe, M., Hasse, K. K.: "Intravascular electric impedance spectroscopy of atherosclerotic lesions using a new impedance catheter system". *Basic Research in Cardiology* **100**, 446-452 (2005).

### Proceedings

1. **Cho, S.**, Thielecke, H.: "Electrical characterization of cell behaviour on microelectrode," Book of abstracts: 33rd International Conference on Micro- and Nano Engineering, 345, (2007).
2. Streitner, I. I., Goldhofer, M., **Cho, S.**, Kinscherf, R., Thielecke, H., Metz, J., Grobholz, R., Süselbeck, T.: "Intravascular electric impedance spectroscopy of human atherosclerotic lesions using a new impedance catheter system," *Atherosclerosis Supplements* **8**, 139 (2007).
3. **Cho, S.**, Becker, S., Briesen, H., Thielecke, H.: "Impedance monitoring of virus-induced cytopathic effect in cells," *IFMBE Proc.* **14**, 597-600 (2006).
4. **Cho, S.**, Thielecke, H.: "Micro hole based single cell chip". *IFMBE Proc.* **11** (2005).
5. **Cho, S.**, Thielecke, H.: "In vitro monitoring of L929 cells growth using impedance spectroscopy". *IFMBE Proc.* **11** (2005).

6. **Cho, S.**, Thielecke, H.: "Simulated impedance of atheroma versus position of electrode array". Proceedings of the 12th FEM Workshop (2005).
7. **Cho, S.**, Thielecke, H.: "Design of electrodes for impedance measurement of lesions in arteries". Proceedings of XII International Conference on Electrical Bio-impedance & V EIT **2**, 351-354 (2004).
8. Thielecke, H., **Cho, S.**, Gorjup, E.: "Monitoring of stem cell differentiation by using a planar electrode chip". IFMBE Proc. **14**, 4242 (2006).
9. Thielecke, H., Suesselbeck, T., **Cho, S.**, Koechlin, J., Metz, J.: "Evaluation of impedance spectroscopy for intravascular tissue characterisation and endoscopy". IFMBE Proc. **11** (2005).

## 10 References

Ambrose, J. A., Tannenbaum, M. A., Alexopoulos, D., Hjemdahl-Monsen, C. E., Leavy, J., Weiss, M., Borrico, S., Gorlin, R., Fuster, V.: "Angiographic progression of coronary artery disease and the development of myocardial infarction". *J. Am. Coll. Cardiol.* **12**, 56-62 (1988).

Arndt, S., Seebach, J., Psathaki, K., Galla, H. J., Wegener, J.: "Bioelectrical impedance assay to monitor changes in cell shape during apoptosis". *Biosensors and Bioelectronics* **19**, 583-594 (2004).

Asami, K., Takahashi, Y., Takashima, S.: "Frequency domain analysis of membrane capacitance of cultured cells (HeLa and myeloma) using the micropipette technique". *Biophysical Journal* **58**, 143-148 (1990).

Athmananthan, S., Reddy, S. B., Nutheti, R., Rao, G. N.: "Comparison of an immobilized human corneal epithelial cell line with Vero cells in the isolation of herpes simplex virus-1 for the laboratory diagnosis of Herpes simplex keratitis". *BMC Ophthalmology* **2**:3 (2002).

Awan, S. A., Gould, R., D.: "Conductivity and dielectric properties of silicon nitride thin films prepared by RF magnetron sputtering using nitrogen gas". *Thin Solid Films* **423**, 267-272 (2003).

Ayliffe, H. E., Frazier, A. B., Rabbitt, R. D.: "Electric impedance spectroscopy using microchannels with integrated metal electrodes". *IEEE Journal of Microelectromechanical Systems* **8**, 50-57 (1999).

Bard, A. J., Faulkner, L. R.: "Electrochemical methods, fundamentals and applications". Wiley, New York (2001).

Barr, D. B., Angerer, J.: "Longitudinal investigation of dietary exposure to selected pesticides". *Environmental Health Perspectives* **109**, 1763-1769 (2001).

Benditt, E. P.: "Implications of the monoclonal character of human atherosclerotic plaques". *Ann. N.Y. Acad. Sci.* **275**, 96-100 (1976).

Carlos, A. F.: "Introduction to finite element methods". Lecture Notes in University of Colorado Boulder, Colorado (2004).

Cheung, K., Gawad, S., Renaud, P.: "Impedance spectroscopy flow cytometry: On-chip label-free cell differentiation". *Cytometry Part A* **65A**, 124-132 (2005).

Cho, S., Thielecke, H.: "Design of electrode array for impedance measurement of lesions in arteries". *Physiol. Meas.* **26**, S19-S16 (2005).

Cho, S., Thielecke, H.: "Influence of the electrode position on the characterisation of artery stenotic plaques by using impedance catheter". *IEEE Trans. Biomed. Eng.* **53**, 2401-2404 (2006).

- Cho, S., Becker, S., Briesen, H., Thielecke, H.: "Impedance monitoring of herpes simplex virus-induced cytopathic effect in Vero cells," *Sensors and Actuators B: Chemical* **123**, 978-982 (2007).
- Cho, S., Thielecke, H.: "Micro hole based cell chip with impedance spectroscopy". *Biosensors and Bioelectronics* **22**, 1764-1768 (2007).
- Cho, S., Castellarnau, M., Samitier, J., Thielecke, H.: "Dependence of impedance of embedded single cells on cellular behaviour". *Sensors* **8**, 1198-1211 (2008).
- Cole, K. S.: "Membranes, ions and impulses". University of California Press, Berkeley (1972).
- Curtis, H., Barnes, N. S.: "Biology". W. H. Freeman (1990).
- de Boer R. W., van Osterom A.: "Electrical properties of platinum electrodes: impedance measurements and time-domain analysis". *Med. & Biol. Eng. & Comput.* **16**, 1-10 (1978).
- de Korte, C. L., Pasterkamp, G., van der Steen, A. F., Woutman, H. A., Bom, N.: "Characterization of plaque components with intravascular ultrasound elastography in human femoral and coronary arteries". *Circulation* **102**, 617-623 (2000).
- Debye, P.: "Polar molecules". Dover, New York (1929).
- Deligöz, H., Yalcinyuva, T., Özgümüş, S., Yildirim, S.: "Electrical properties of conventional polyimide films: Effects of chemical structure and water uptake". *Journal of Applied Polymer Science* **100**, 810-818 (2006).
- Ehret, R., Baumann, W., Brischwein, M., Schwinde, A., Stegbauer, K., Wolf, B.: "Monitoring of cellular behaviour by impedance measurements on interdigitated electrode structures". *Biosensors and Bioelectronics* **12**, 92-41 (1997).
- Einthoven, W., Fahr, G., de Waart, A.: "Über die Richtung und die manifeste Grösse der Potentialschwankungen im menschlichen Herzen und über den Einfluss der Herzlage auf die Form de Elektrokardiogramms". *Pflügers Arch. Ges. Physiol.* **150**, 275-315 (1913).
- El-Aal, A. M., Sayed, M. E., Mohammed, E., Ahmed, M., Fathy, M.: "Evaluation of herpes simplex detection in corneal scrapings by three molecular methods". *Curr. Microbiol.* **52**, 379-382 (2006).
- Elliott, D. J.: "Microlithography, process technology for IC fabrication". McGraw-Hill, New York (1986).
- Elshabini, A., Barlow, F.: "Thin film technology handbook". McGraw-Hill, New York (1998).
- English, D. A., Kovala, T., Welch, Z., Harvey, K. A., Siddiqui, R. A., Brindley, D. N., Garcia, J. G. N.: "Induction of endothelial cell chemotaxis by sphingosine 1-phosphate and stabilization of endothelial monolayer barrier function by lysophosphatidic acid, potential mediators of hematopoietic angiogenesis". *NCS Compendium* **8**, 627-634 (1999).

- Fabricant, C. G., Fabricant, J., Litrenta, M. M., Minick, C. R.: "Virus-induced atherosclerosis". *The Journal of Experimental Medicine* **148**, 335-340 (1978).
- Fazel, S., Cimini, M., Chen, L., Li, S., Angoulvant, D., Fedak, P., Verma, S., Weisel, R. D., Keating, A., Li, R.: "Cardioprotective c-kit<sup>+</sup> cells are from the bone marrow and regulate the myocardial balance of angiogenic cytokines". *The Journal of Clinical Investigation* **116**, 1865-1877 (2006).
- Foster, K. R., Schwan, H. P.: "Dielectric properties of tissue and biological materials: A critical review". *Crit. Rev. Biomed. Eng.* **17**, 25-103 (1989).
- Fuhr, G., Arnold, W. M., Hagedorn, R., Mueller, T., Benecke, W., Wagner, B., Zimmermann, U.: "Levitation, holding, and rotation of cells within traps made by high-frequency fields". *Biochimica et Biophysica Acta* **1108**, 215-223 (1992).
- Fuhr, G., Glasser, H., Mueller T., Schnelle, T.: "Cell manipulation and cultivation under a.c. electric field influence in highly conductive culture media". *Biochimica et Biophysica Acta* **1201**, 353-360 (1994).
- Fuster, V., Badimon, L., Badimon, J. J., Chesebro, J. H.: "The pathogenesis of coronary artery disease and the acute coronary syndromes". *N. Engl. J. Med.* **326**, 242-50 (1992).
- Gabriel, C., Gabriel, S., Corthout, E.: "The dielectric properties of biological tissues: I. Literature survey". *Phys. Med. Biol.* **41**, 2231-2249 (1996).
- Geselowitz, D. B.: "An application of electrocardiographic lead theory to impedance plethysmography". *IEEE Trans. Biomed. Eng.* **18**, 38-41 (1971).
- Giaever, I., Keese, C. R.: "Micromotion of mammalian cells measured electrically". *Proc. Natl. Acad. Sci. USA* **88**, 7896-7900 (1991) (correction: *Proc. Natl. Acad. Sci. USA* **90**, 1634 (1993)).
- Giaever, I., Keese, C. R.: "A morphological biosensor for mammalian cells". *Nature* **366**, 591-592 (1993).
- Giebel, K.F., Bechinger, C., Herminghaus, S., Riedel, M., Leiderer, P., Weiland, U., Bastmeyer, M.: "Imaging of cell/substrate contacts of living cells with surface plasmon resonance microscopy". *Biophysical Journal* **76**, 509-516 (1999).
- Gielen, F. L. H., Wallinga-de Jonge, W., Boon, K. L.: "Electrical conductivity of skeletal muscle tissue: Experimental results from different muscles in vivo". *Medical and Biological Engineering* **22**, 569-577 (1984).
- Grimnes, S. and Martinsen, Ø. G.: "Bioimpedance and bioelectricity basics". Academic Press, San Diego (2000).
- Hadjout, N., Laevsky, G., Knecht, D. A., Lynes, M. A.: "Automated real-time measurement of chemotactic cell motility". *Biotechniques* **31**, 1130-1138 (2001).
- Hagedorn, R., Fuhr, G., Lichtwardt-Zinke, K., Richter, E., Hornung, J., Voigt, A.: "Characterisation of cell movement by impedance measurement on fibroblasts grown on perforated Si-membranes". *Biochimica et Biophysica Acta* **1269**, 221-232 (1995).

- Harrington, R. F.: "Time-harmonic electromagnetic fields". McGraw-Hill Book Co., New York (1961).
- Hodgkin, A. L., Huxley, A. F.: "A quantitative description of membrane current and its application to conductance and excitation in nerve". *J. Physiol.* **117**, 500-544 (1952).
- Holder, D. S.: "Electrical impedance tomography: Methods, history and applications". Institute of Physics Publishing, Bristol and Philadelphia (2005).
- Hoogduijn, M. J., Rakonczay, Z., Genever, P. G.: "The effects of anticholinergic insecticides on human mesenchymal stem cells". *Toxicological Sciences* **94**, 342-350 (2006).
- Huang, X., Nguyen, D., Greve, D. W., Domach, M. M.: "Simulation of microelectrode impedance changes due to cell growth". *IEEE Sensors Journal* **4**, 576-583 (2004).
- Huang, Y., Rubinsky, B.: "Microfabricated electroporation chip for single cell membrane permeabilization". *Sensors and Actuators A* **89**, 242-249 (2001).
- Huang, Y., Sekhon, N. S., Borninski, J., Chen, N., Rubinsky, B.: "Instantaneous, quantitative single-cell viability assessment by electrical evaluation of cell membrane integrity with microfabricated devices". *Sensors and Actuators A* **105**, 31-39 (2003).
- Ivorra, A., Gomez, R., Noguera, N., Villa, R., Sola, A., Palacios, L., Hotter, G., Aguilo, J.: "Minimally invasive silicon probe for electrical impedance measurements in small animals". *Biosensors and Bioelectronics* **19**, 391-399 (2003).
- Key, N. S., Vercellotti, G. M., Winkelmann, J. C., Moldow, C. F., Goodman, J. L., Esmon, N. L., Esmon, C. T., Jacob, H. S.: "Infection of vascular endothelial cells with herpes simplex virus enhances tissue factor activity and reduces thrombomodulin expression". *Proc. Natl. Acad. Sci. USA* **87**, 7095-7099 (1990).
- Konings, M. K., Mali, W. P. Th. M., Viergever, M. A.: "Development of an Intravascular impedance catheter for detection of fatty lesions in arteries". *IEEE Trans. Med. Imag.* **16**, 439-446 (1997).
- Kovacs, G. T. A.: "Microelectrode models for neural interfaces". In *Enabling technologies for cultured neural networks* (Stenger, D.A. and McKenna, T.M., eds.), 121-165, Academic Press, New York (1994).
- Langmuir, I.: "The interaction of electron and positive ion space charges in cathode sheaths". *Physical Review*. **33**, 954-989 (1929).
- Lo, C. M., Keese, C. R., Giaever, I.: "Impedance analysis of MDCK cells measured by electric cell-substrate impedance sensing". *Biophysical Journal* **69**, 2800-2807 (1995).
- Lo, C. M., Ferrier, J.: "Impedance analysis of fibroblastic cell layers measured by electric cell-substrate impedance sensing". *Physical Review E* **57**, 6982-6987 (1998).
- Lundien, M. C., Mohammed, K. A., Nasreen, N., Tepper, R. S., Hardwick, J. A., Sanders, K. L., van Horn, R. D., Antony, V. B.: "Induction of MCP-1 expression in airway epithelial

cells: Role of CCR2 receptor in airway epithelial injury". *Journal of Clinical Immunology* **22**, 144-152 (2002).

Luong, J. H. T., Habibi-Rezaei, M., Meghrou, J., Xiao, C., Male, K. B., Kamen, A.: "Monitoring motility, spreading, and mortality of adherent insect cells using an impedance sensor". *Analytical Chemistry* **73**, 1844-1848 (2001).

Maekinen, K., Manninen, H., Hedman, M., Mussalo, H., Alhava, E., Ylae-Herttuala, S.: "Increased Vascularity Detected by Digital Subtraction Angiography after VEGF Gene Transfer to Human Lower Limb Artery: A Randomized, Placebo-Controlled, Double-Blinded Phase II Study". *Molecular Therapy* **6**, 127-133 (2002).

Malmivuo, J., Plonsey, R.: "Bioelectromagnetism: principles and application of bioelectric and biomagnetic fields". Oxford University Press, New York (1995).

Martinsen, Ø. G.: "Electrode systems and sensitivity fields". *Proc. XII ICEBI & V EIT* **2**, 737-738 (2004).

Maxwell, J. C.: "A treatise on electricity and magnetism". Clarendon Press, Oxford (1873).

Minick, C. R.: "Immunologic arterial injury in atherogenesis". *Ann. N.Y. Acad. Sci.* **275**, 210-227 (1976).

Mitra, P., Keese, C., Giaever, I.: "Electric measurement can be used to monitor the attachment and spreading of cells in tissue culture". *BioTechniques* **4**, 504-510 (1991).

Nair, A., Kuban, B. D., Tuzcu, E. M., Schoenhagen, P., Nissen, S. E. and Vince, D. G.: "Coronary plaque classification with intravascular ultrasound radiofrequency data analysis". *Circulation* **106**, 2200-2206 (2002).

Newman, J.: "Resistance for flow of current to a disk". *Journal of Electrochemical Society* **113**, 501-502 (1966).

Noiri, E., Nakao, A., Uchida, K., Tsukahara, H., Ohno, M., Fujita, T., Brodsky, S., Goligorsky, M.: "Oxidative and nitrosative stress in acute renal ischemia". *American Journal of Physiology-Renal Physiology* **281**, F948-F957 (2001).

Ochoa, L., Waypa, G., Mahoney, J. R. Jr., Rodriguez, L., Minnear, F. L.: "Contrasting effects of hypochlorous acid and hydrogen peroxide on endothelial permeability: prevention with cAMP drugs". *American Journal of Respiratory and Critical Care Medicine* **156**, 1247-1255 (1997).

Oldenburg, D., Jones, F.: "Basic concepts of resistivity and induced polarization profiling". University of British Columbia, Vancouver (1998).

Pittenger, M. F., Mackay, A. M., Beck, S. C., Jaiswal, R. K., Douglas, R., Mosca, J. D., Moorman, M. A., Simonetti, D. W., Craig, S., Marshak, D. R.: "Multilineage potential of adult human mesenchymal stem cells". *Science* **284**, 143-147 (1999).

Reininger-Mack, A., Thielecke, H., Robitzki, A.: "3D-Biohybrid System: Application in Drug Screening". *Trends in Biotechnology* **20**, 56-61 (2001).

- Ross, R., Glomset, J. A.: "The pathogenesis of atherosclerosis". *N. Engl. J. Med.* **295**, 369-377; 420-425 (1976).
- Rutten, W., Mouveroux, J., Buitenweg, J., Heida, C., Ruardij, T., Marani, E., Lakke, E.: "Neuroelectronic interfacing with cultured multielectrode arrays toward a cultured probe". *Proceedings of the IEEE* **89**, 1013-1029 (2001).
- Sawyer, D. T., Sobkowiak, A., Roberts, J. L.: "Electrochemistry for Chemists (2nd ed.)". Wiley-Interscience, New York (1995).
- Schwan, H. P.: "Electrical properties of tissue and cell suspensions". in: Lawrence JH, Tobias CA (eds) "Advances in biological and medical physics". Academic Press, New York, **V**, 147-209 (1957).
- Schwan, H. P.: "Electrical characteristics of tissues: A survey". *Biophysik* **1**, 198-208 (1963).
- Sharma, K. V., Koenigsberger, C., Brimijoin, S., Bigbee, J. W.: "Direct evidence for an adhesive function in the noncholinergic role of acetylcholinesterase in neurite outgrowth". *Journal of Neuroscience Research* **63**, 165-175 (2001).
- Slager, C. J., Phaff, A. C., Essed, C. E., Bom, N., Schuurbijs, J. Ch. H., Serruys, P. W.: "Electrical impedance of layered atherosclerotic plaques on human aortas". *IEEE Trans. Biomed. Eng.* **39**, 411-418 (1992).
- Smith, S. R., Foster, K. R.: "Dielectric properties of low-water-content tissues". *Physics in Medicine and Biology* **30**, 965-973 (1985).
- Smith, T., Wang, H. S., Hogg, M. G., Henrikson, R. C., Keese, C. R., Giaever, I.: "Prostaglandin E2 elicits a morphological change in cultured orbital fibroblasts from patients with graves ophthalmopathy". *Proceedings of the National Academy of Sciences* **91**, 5094-5098 (1994).
- South, G. P., Grant, E. H.: "The contribution of proton fluctuation to dielectric relaxation in protein solutions". *Biopolymers* **12**, 1937-1944 (1973).
- Suesserman, M. F., Spelman, F. A.: "Quantitative in vivo measurements of inner ear tissue resistivities: in vitro characterization". *IEEE Trans. Biomed. Eng.* **40**, 1032-1047 (1993).
- Sary, H. C., Chandler, A. B., Dinsmore, R. E., Fuster, V., Glagov, S., Insull, W., Rosenfeld, M. E., Schwartz, C. J., Wagner, W. D., Wissler, R. W.: "A definition of advanced types of atherosclerotic lesions and a histological classification of atherosclerosis". *Arteriosclerosis, Thrombosis, and Vascular Biology* **15**, 1512-1531 (1995).
- Stieglitz, T., Beutel, H., Meyer J. U.: "A flexible, light-weight multichannel sieve electrode with integrated cables for interfacing regenerating peripheral nerves". *Sensors and Actuators A* **60**, 240-243 (1997).
- Stieglitz, T., Meyer, J. U.: "Implantible microsystems: polyimide-based neuroprostheses for interfacing nerves". *Med. Device Technol.* **10**, 28-30 (1999).

- Stiles, D. K., Oakley, B. A.: "Simulated characterization of atherosclerotic lesions in the coronary arteries by measurement of bioimpedance". *IEEE Trans. Biomed. Eng.* **50**, 916-921 (2003).
- Süselbeck, T., Thielecke, H., Koechlin, J., Cho, S., Weinschenk, I., Metz, J., Borggrefe, M., Hasse, K. K.: "Intravascular electric impedance spectroscopy of atherosclerotic lesions using a new impedance catheter system". *Basic Research in Cardiology* **100**, 446-452 (2005).
- Srivastava, J. K., Prasad, M., Wagner, Jr. J. B.: "Electrical conductivity of silicon dioxide thermally grown on silicon". *Journal of The Electrochemical Society* **132**, 955-963 (1985).
- Takashima, S., Schwan, H. P.: "Passive electrical properties of squid axon membrane". *J. Membr. Biol.* **17**, 51-68 (1974).
- Takashima, S., Yantorno, R. E.: "Investigation of voltage dependent membrane capacity of squid giant axons". *Ann. N.Y. Acad. Sci.* **303**, 306-321 (1977).
- Thanawala, S., Palyvoda, O., Georgiev, D. G., Khan, S. P., Al-Homoudi, I. A., Newaz, G., Auner, G.: "A neural cell culture study on thin film electrode materials". *Journal of Materials Science: Materials in Medicine* **18**, 1745-1752 (2007).
- Thielecke, H., Stieglitz, T., Beutel, H., Matthies, T., Ruf, H. H., Meyer, J. U.: "Fast and precise positioning of single cells on planar electrode substrates". *IEEE Eng. Med. Biol. Mag.* **18**, 48-52 (1999).
- Thielecke, H., Mack, A., Robitzki, A.: "Biohybrid Microarrays – Impedimetric Biosensors with 3D in vitro Tissues for Toxicological and Biomedical Screening" *Fresenius' Journal of Analytical Chemistry* **369**, 23-29 (2001a).
- Thielecke, H., Mack, A., Robitzki, A.: "A multicellular spheroid-based sensor for anti-cancer therapeutics". *Biosensors and Bioelectronics* **16**, 261-269 (2001b).
- Tokuhiro, T., Menafra, L., Szmant, H. H.: "Contribution of relaxation and chemical shift results to the elucidation of the structure of the water-DMSO liquid system". *Journal of Chemical Physics* **61**, 2275-2282 (1974).
- Verheye, S., de Meyer, G. R., van Langenhove, G., Knaapen, M. W., Kockx, M. M.: "In vivo temperature heterogeneity of atherosclerotic plaques is determined by plaque composition". *Circulation* **105**, 1596-1601 (2002).
- Waller, A. D.: "A demonstration on man of electromotive changes accompanying the heart's beat". *The Journal of Physiology* **8**, 229-234 (1887).
- Wegener, J., Sieber, M., Galla, H. J.: "Impedance analysis of epithelial and endothelial cell monolayers cultured on gold surfaces". *J. Biochem. Biophys. Methods* **32**, 151-170 (1996).
- Xiao, C., Lachance, B., Sunahara, G., Luong, J.: "Assessment of cytotoxicity using electric cell-substrate impedance sensing: concentration and time response function approach". *Analytical Chemistry* **74**, 5748-5753 (2002).

Xiao, C., Luong, J.: "Assessment of cytotoxicity by emerging impedance spectroscopy". *Toxicology and Applied Pharmacology* **206**, 102-112 (2005).

Yach, D., Hawkes, C., Gould, C. L., Hofman, K. J.: "The global burden of chronic diseases - overcoming impediments to prevention and control". *JAMA* **291**, 2616-2622 (2004).

## Appendix: Programming Codes for FEM Simulation

- Used software: FlexPDE 4.2.16 (PDE Solutions, Antioch, USA)

### A. Single Cell on Micro Hole Model in 3.1.2

```

TITLE   '1 cell on hole'

SELECT      {Method controls}

           alias(r) = "R(m)"      {Distance unit: m}

           alias(z) = "Z(m)"

           errlim=1e-4           {Error limitation}

COORDINATES

           cylinder('r','z')     {Symmetrical cylinder axis}

VARIABLES   {System variables}

           V1r, V1i             {Real & imaginary of potential in lead field}

DEFINITIONS {Parameter definitions}

           f=staged(1e6,630957,398107,251187,158489,1e5,63096,39811,25119,
15849,1e4,6310,3981,2512,1585,1e3,631,398,251,159,1e2,63,40,25,16
,1e1,6.3,4,2.5,1.6,1e0)          {Frequency, Hz}

           w=2*pi*f              {Angular frequency, rad/sec}

           length=360e-6         {Radius of whole area, m}

           th_si3n4=1e-6         {Thickness of insulated membrane, m}

           r_hole=3e-6           {Radius of hole, m}

           th_mem=10e-9          {Thickness of cell membrane, m}

           hg=0.3e-6             {Cell/surface gap, m}

           hc=5e-6               {Polar radius of cell, m}

           rc=5e-6               {Equatorial radius of cell, m}

           vision=8e-6           {Zoom, m}

           I=1e-6                {Input current, A}

           A=pi*(2*length)^2     {Surface area of electrode, m^2}

```

$I_n=I/A$	{Input current density, $A/m^2$ }
$K_{buffer}=1.6$	{Conductivity of solution, $S/m$ }
$K_{mem}=1e-8$	{Conductivity of cell membrane, $S/m$ }
$K_{cell}=0.5$	{Conductivity of intra cellular space, $S/m$ }
$K_{si3n4}=1e-12$	{Conductivity of insulated layer, $S/m$ }
$K$	{Conductivity}
$\epsilon_0=8.854e-12$	{Permittivity of vacuum, $F/m$ }
$\epsilon_{buffer}=80*\epsilon_0$	{Permittivity of solution, $F/m$ }
$\epsilon_{mem}=11.3*\epsilon_0$	{Permittivity of membrane, $F/m$ }
$\epsilon_{cell}=80*\epsilon_0$	{Permittivity of intracellular space, $F/m$ }
$\epsilon_{si3n4}=5.5*\epsilon_0$	{Permittivity of insulated layer, $F/m$ }
Epsilon	{Permittivity}
$E1r=-grad(V1r)$	{Real part of electric fields, $V/m$ }
$E1i=-grad(V1i)$	{Imaginary part of electric fields, $V/m$ }
$J1r=K*E1r-w*\epsilon_0*E1i$	{Real part of current density, $A/m^2$ }
$J1i=w*\epsilon_0*E1r+K*E1i$	{Imaginary part of current density, $A/m^2$ }
$J1r_m=magnitude(J1r)$	{Magnitude of real of current density}
$J1i_m=magnitude(J1i)$	{Magnitude of imaginary of current density}
$J1m=sqrt((J1r_m^2)+(J1i_m^2))$	{Magnitude of whole current density}
{Sensitivity $S = DOT((J1r+J1i),(J2r+J2i)) / I^2$ }	
$Sr=(DOT(J1r,J1r)-DOT(J1i,J1i)) / I^2$	{Real part of sensitivity, $m^{-4}$ }
$Si=(DOT(J1i,J1r)+DOT(J1r,J1i)) / I^2$	{Imaginary part of sensitivity}
{Impedance $Z = \int (S/(K+i*w*\epsilon_0)) dv = dvZr + i dvZi$ }	
$dvZr=(K*Sr+w*\epsilon_0*Si)/(K^2 + (w*\epsilon_0)^2)$	
$dvZi=(K*Si-w*\epsilon_0*Sr)/(K^2 + (w*\epsilon_0)^2)$	
$Zr=vol\_integral(dvZr)$	{Real part of impedance }
$Zi=vol\_integral(dvZi)$	{Imaginary part of impedance}

$$Z_m = \sqrt{(Z_r^2) + (Z_i^2)} \quad \{\text{Impedance magnitude, ohms}\}$$

$$\text{Phase} = \arctan(Z_i/Z_r) * 180/\pi \quad \{\text{Phase, degree}\}$$

EQUATIONS {Laplace equation}

$$V_{1r}: \text{div}(K * \text{grad}(V_{1r}) - \text{Epsilon} * w * \text{grad}(V_{1i})) = 0$$

$$V_{1i}: \text{div}(K * \text{grad}(V_{1i}) + \text{Epsilon} * w * \text{grad}(V_{1r})) = 0$$

BOUNDARIES

region 'all' K=K\_buffer Epsilon=eps\_buffer {Whole region}

start 'outer' (0,0) Natural(V1r)=ln Natural(V1i)=0 line to (2\*length,0)  
Natural(V1r)=0 line to (2\*length,2\*length) Natural(V1r)=-ln line to  
(0,2\*length) Natural(V1r)=0 line to finish

region 'insulator' K=K\_si3n4 Epsilon=eps\_si3n4 {Insulated layer}

start 'si3n4' (r\_hole,length-th\_si3n4) line to (2\*length,length-th\_si3n4) to  
(2\*length,length) to (r\_hole,length) to finish

region 'mem' K=K\_mem Epsilon=eps\_mem {Cell membrane}

start 'membrane' (0,hg+hc+length) line to (0,hg+hc-th\_mem+length)  
arc(center=0,hg+th\_mem+length) to (rc-th\_mem,hg+th\_mem+length) line  
to (0,hg+th\_mem+length) to (0,hg+length) to (rc,hg+length)  
arc(center=0,hg+length) to finish

region 'cell' K=K\_cell Epsilon=eps\_cell {Intracellular space}

start 'incell' (0,hg+hc-th\_mem+length) line to (0,hg+th\_mem+length) to  
(rc-th\_mem,hg+th\_mem+length) arc(center=0,hg+th\_mem+length) to  
finish

feature {To make it sure to form the outline of cell membrane}

start 'membranef' (0,hg+hc+length) line to (0,hg+hc-th\_mem+length)  
arc(center=0,hg+th\_mem+length) to (rc-th\_mem,hg+th\_mem+length) line  
to (0,hg+th\_mem+length) to (0,hg+length) to (rc,hg+length)  
arc(center=0,hg+length) to finish

PLOTS

contour (J1m) painted log zoom (0,length-2\*th\_si3n4,vision,vision) as 'J1m'

{Display of the log-sclaed current density magnitude}

SUMMARY

report(Zm) as 'Zm of all of all region' {Impedance magnitude}

END

## B. Cells on Electrode Model in 4.1.2

TITLE 'cells on electrode'

SELECT { method controls }

alias(r) = "R(m)"

alias(z) = "Z(m)"

plotintegrate OFF

errlim=1e-3 {error limitation}

COORDINATES

ycylinder('r','z') {Symmetrical cylinder axis}

VARIABLES {System variables}

V1r, V1i {Potential, Potential of Cells and Proteins = 0}

DEFINITIONS {Parameter Definitions}

f=staged(1e6,630957,398107,251187,158489,1e5,63096,39811,25119,  
15849,1e4,6310,3981,2512,1585,1e3,631,398,251,159,1e2)  
{100-1MHz}

w=2\*pi\*f {Angular frequency: rad/sec}

rc=30e-6 {Radius of cell}

hg=100e-9 {cell-surface separation: 100 nm}

gc=1e-6 {Gap between cells}

re=rc+gc {Radius of electrode}

hc=5e-6 {Height of cell}

tm=10e-9 {thickness of cell membrane: 10nm}

K\_buffer=1.6 {S/m}

K\_mem=1e-8 {Conductivity of cell membrane, S/m}

K\_cell=0.5 {Conductivity of intra cellular space, S/m}

K {Conductivity}

$\epsilon_0=8.854e-12$	{F/m, in Vacuum}
$\epsilon_{\text{buffer}}=80*\epsilon_0$	{mostly by water, until 1Mhz}
$\epsilon_{\text{mem}}=11.3*\epsilon_0$	{Permittivity of membrane, F/m}
$\epsilon_{\text{cell}}=80*\epsilon_0$	{Permittivity of intracellular space, F/m}
Epsilon	{Permittivity}
$E1r=-\text{grad}(V1r)$	{Real part of electric fields, V/m}
$E1i=-\text{grad}(V1i)$	{Imaginary part of electric fields, V/m}
$J1r=K*E1r-w*\text{Epsilon}*E1i$	{Real part of current density, A/m <sup>2</sup> }
$J1i=w*\text{Epsilon}*E1r+K*E1i$	{Imaginary part of current density, A/m <sup>2</sup> }
$J1r_m=\text{magnitude}(J1r)$	{Magnitude of real of current density}
$J1i_m=\text{magnitude}(J1i)$	{Magnitude of imaginary of current density}
$J1m=\text{sqrt}((J1r_m^2)+(J1i_m^2))$	{Magnitude of whole current density}
{Sensitivity $S = \text{DOT}((J1r+J1i),(J2r+J2i)) / I^2$ }	
$Sr=(\text{DOT}(J1r,J1r)-\text{DOT}(J1i,J1i)) / I^2$	{Real part of sensitivity, m <sup>-4</sup> }
$Si=(\text{DOT}(J1i,J1r)+\text{DOT}(J1r,J1i)) / I^2$	{Imaginary part of sensitivity}
{Impedance $Z = \text{integral}(S/(K+i*w*\text{Epsilon}))$ , $Z/dv = dvZr + i dvZi$ }	
$dvZr=(K*Sr+w*\text{Epsilon}*Si)/(K^2 + (w*\text{Epsilon})^2)$	
$dvZi=(K*Si-w*\text{Epsilon}*Sr)/(K^2 + (w*\text{Epsilon})^2)$	
$Zr=\text{vol\_integral}(dvZr)$	{Real part of impedance }
$Zi=\text{vol\_integral}(dvZi)$	{Imaginary part of impedance}
$Zm=\text{sqrt}((Zr^2) + (Zi^2))$	{Impedance magnitude, ohms}
$\text{Phase}=\text{arctan}(Zi/Zr)*180/\text{pi}$	{Phase, degree}
$\text{rat}=(500e-6/\text{re})^2$	{ratio of total electrode area to the one in simulation}
$tZr=Zr/\text{rat}$	{Resistance on the electrode with radius of 500 micrometer}
$tZi=Zi/\text{rat}$	{Reactance on the electrode with radius of 500 micrometer}
$tZm=Zm/\text{rat}$	{Impedance on the electrode with radius of 500 micrometer}

EQUATIONS {Laplace equation}

$$V1r: \text{div}(K * \text{grad}(V1r) - \text{Epsilon} * w * \text{grad}(V1i)) = 0$$

$$V1i: \text{div}(K * \text{grad}(V1i) + \text{Epsilon} * w * \text{grad}(V1r)) = 0$$

#### BOUNDARIES

region K=K\_buffer Epsilon=eps\_buffer {Buffer}

start (0,0) Natural(V1r)=IN line to(re,0) Natural(V1r)=0 Natural(V1i)=0 line to(re,hc) Value(V1r)=0 Value(V1i)=0 line to(0,hc) Natural(V1r)=0 Natural(V1i)=0 line to finish

region 'mem' K=K\_mem Epsilon=eps\_mem {Cell membrane}

start 'membrane' (0,hc) line to(rc,hc) to(rc,hg) line to (0,hg) Natural(V1r)=0 Natural(V1i)=0 line to finish

region 'cell' K=K\_cell Epsilon=eps\_cell {Intra cellular space}

start 'icell' (0,hc-tm) line to(rc-tm,hc-tm) to(rc-tm,hg+tm) line to (0,hg+tm) Natural(V1r)=0 Natural(V1i)=0 line to finish

#### PLOTS

contour(V1r) painted as 'V1R'

{Display of the potential distribution}

#### SUMMARY

report(tZm) as 'tZm of all of all region'

{Total impedance magnitude on electrode with radius of 500 micro meter}

END

### C. Two-Layer Model in 5.1.3

TITLE 'four electrode array in 0.9% NaCl with different thickness'

SELECT

alias(x) = "X(mm)" {distance unit: mm}

alias(y) = "Y(mm)"

alias(z) = "Z(mm)"

plotintegrate OFF

errlim=1e-4 {error limitation}

## COORDINATES

cartesian3 {3D axis}

## VARIABLES {System variables}

V1r, V1i, V2r, V2i {Real & imaginary of potential in 1st & 2nd lead field}

## DEFINITIONS {Parameter definitions}

f=10000 {Frequency: 10 kHz}

w=2\*pi\*f {angular frequency}

all=staged(0.111,0.222,0.333,0.444,0.555,0.666,0.777,0.888,1,1.111,1.222,1.333,10) {Thickness of first layer from 111  $\mu\text{m}$  to 1 cm}

r\_all=5.5 {Diameter of dish: 5.5 cm}

dist=0.333 {Distance between electrode's centers: 333  $\mu\text{m}$ }

wid=0.1 {Width of electrode: 100  $\mu\text{m}$ }

A=wid\*wid {Surface area of electrode,  $\text{mm}^2$ }

I=1 {Input current, A}

In=I/A {Input current density,  $\text{A}/\text{mm}^2$ }

K\_NaCl= 1.6\*1E-3 {0.9% NaCl electrolyte at 25°C,  $\text{S}/\text{mm}$ }

K=K\_NaCl {Conductivity of whole area}

eps0=8.854e-12\*1E-3 {permittivity in vacuum,  $\text{F}/\text{mm}$ }

eps\_NaCl=78.5\*eps0 {permittivity of NaCl electrolyte,  $\text{F}/\text{mm}$ }

Epsilon=eps\_NaCl {Permittivity of whole area}

E1r=-grad(V1r)\*1E3 {Real part of electric fields in 1st lead field,  $\text{V}/\text{mm}$ }

E1i=-grad(V1i)\*1E3 {Imaginary part of electric fields in 1st lead field}

J1r=K\*E1r\*1E3 {Real part of current density in 1st lead field,  $\text{A}/\text{mm}^2$ }

J1i=K\*E1i\*1E3 {Imaginary part of current density in 1st lead field}

E2r=-grad(V2r)\*1E3 {Real part of electric fields in 2nd lead field,  $\text{V}/\text{mm}$ }

E2i=-grad(V2i)\*1E3 {Imaginary part of electric fields in 2nd lead field}

J2r=K\*E2r\*1E3 {Real part of current density in 2nd lead field,  $\text{A}/\text{mm}^2$ }

J2i=K\*E2i\*1E3 {Imaginary part of current density in 2nd lead field}

$Sensitivity_r = \text{DOT}(J1r, J2r) / I^2$       {Real part of sensitivity,  $\text{mm}^{-4}$ }  
 $Sensitivity_i = \text{DOT}(J1i, J2i) / I^2$       {Imaginary part of sensitivity,  $\text{mm}^{-4}$ }  
 $S_r = \ln(\text{abs}(Sensitivity_r))$       {Natural log-scaled Sensitivityr}  
 $S_i = \ln(\text{abs}(Sensitivity_i))$       {Natural log-scaled Sensitivityi}  
 {Impedance  $Z = \text{integral}(S / (K + i * w * \text{Epsilon}))$ ,  $Z / dv = dvZ_r + i dvZ_i$ }  
 $dvZ_r = (K * Sensitivity_r + w * \text{Epsilon} * Sensitivity_i) / (K^2 + (w * \text{Epsilon})^2) / 1E3$   
 $dvZ_i = (K * Sensitivity_i - w * \text{Epsilon} * Sensitivity_r) / (K^2 + (w * \text{Epsilon})^2) / 1E3$   
 $Z_r = \text{integral}(dvZ_r) * 1E-9$       {Real part of impedance }  
 $Z_i = \text{integral}(dvZ_i) * 1E-9$       {Imaginary part of impedance}  
 $Z_m = \text{sqrt}((Z_r^2) + (Z_i^2))$       {Impedance magnitude, ohms}  
 $\text{Phase} = \arctan(Z_i / Z_r) * 180 / \pi$       {Phase, degree}

EQUATIONS    {Laplace equation with lead field theory}

$V1r: \text{div}(K * \text{grad}(V1r) - \text{Epsilon} * w * \text{grad}(V1i)) = 0$     {Potential in 1st lead field}  
 $V1i: \text{div}(K * \text{grad}(V1i) + \text{Epsilon} * w * \text{grad}(V1r)) = 0$   
 $V2r: \text{div}(K * \text{grad}(V2r) - \text{Epsilon} * w * \text{grad}(V2i)) = 0$     {Potential in 2nd lead field}  
 $V2i: \text{div}(K * \text{grad}(V2i) + \text{Epsilon} * w * \text{grad}(V2r)) = 0$

EXTRUSION

Surface 'bottom'  $Z=0$       {Electrode array at bottom}  
 Layer 'buffer'              {NaCl electrolyte}  
 Surface 'top'  $Z=\text{all}$       {Level of electrolyte}

BOUNDARIES

surface 'bottom'     $\text{Natural}(V1r)=0$      $\text{Natural}(V1i)=0$      $\text{Natural}(V2r)=0$   
 $\text{Natural}(V2i)=0$   
 surface 'top'     $\text{Natural}(V1r)=0$      $\text{Natural}(V1i)=0$      $\text{Natural}(V2r)=0$      $\text{Natural}(V2i)=0$   
 region 'outer'      {Boundary of dish}  
 start 'whole' (r\_all,0)     $\text{Natural}(V1r)=0$      $\text{Natural}(V1i)=0$      $\text{Natural}(V2r)=0$   
 $\text{Natural}(V2i)=0$  arc (center=0,0) angle=360 finish  
 region 'I1 electrode' {boundary of current output electrode}

```

surface 'bottom' Natural(V1r)=In Natural(V1i)=0

layer 'buffer' K=K_NaCl Epsilon=eps_NaCl

start 'I1' (-3*dist/2-wid/2,-wid/2) line to (-3*dist/2+wid/2,-wid/2) to
(-3*dist/2+wid/2,wid/2) to (-3*dist/2-wid/2,wid/2) to finish

region 'I2 electrode' {boundary of current input electrode}

surface 'bottom' Natural(V1r)=-In Natural(V1i)=0

layer 'buffer' K=K_NaCl Epsilon=eps_NaCl

start 'I2' (3*dist/2-wid/2,-wid/2) line to (3*dist/2+wid/2,-wid/2) to
(3*dist/2+wid/2,wid/2) to (3*dist/2-wid/2,wid/2) to finish

region 'V1 electrode' {boundary of voltage measurement electrode 1}

surface 'bottom' Natural(V2r)=In Natural(V2i)=0

layer 'buffer' K=K_NaCl Epsilon=eps_NaCl

start 'V1' (-dist/2-wid/2,-wid/2) line to (-dist/2+wid/2,-wid/2) to
(-dist/2+wid/2,wid/2) to (-dist/2-wid/2,wid/2) to finish

region 'V2 electrode' {boundary of voltage measurement 2 electrode}

surface 'bottom' Natural(V2r)=-In Natural(V2i)=0

layer 'buffer' K=K_NaCl Epsilon=eps_NaCl

start 'V2' (dist/2-wid/2,-wid/2) line to (dist/2+wid/2,-wid/2) to
(dist/2+wid/2,wid/2) to (dist/2-wid/2,wid/2) to finish

```

#### PLOTS

```

contour(Sr) painted on surface Y=0.0 zoom (-2*dist,0,4*dist,4*dist) as
'Sensitivity at Y=0'

contour(Sr) on surface X=0.0 zoom (-2*dist,0,4*dist,4*dist) as 'Sensitivityr
at X=0'

```

SUMMARY {Calculation of resistance by sensitivity equation}

```

report(Zm) as 'Zm in all of all region' {Impedance magnitude, ohms}

```

END

### D. Atheromatous Vessel with BIC Model in 5.1.4

TITLE 'Atheromatous artery with BIC'

```

SELECT          {Method controls}

    NOMINMAX ON

    alias(x) = "X(m)"    {Distance unit: m}

    alias(y) = "Y(m)"

    alias(z) = "Z(m)"

    plotintegrate OFF

    errlim=1e-4        {Error limitation}

    STAGEGRID ON

    GRIDLIMIT 24

COORDINATES

    cartesian3        {3D axis}

VARIABLES          {System variables}

    V1r, V1i, V2r, V2i  {Real & imaginary of potential in 1st & 2nd lead field}

DEFINITIONS        {Parameter definitions}

    f=10000           {Frequency, Hz}

    w=2*pi*f          {Angular frequency, rad/sec}

    theta=45          {Distributed angle of lipid}

    eth=staged(0,pi/36,pi/18,pi/12,pi/9,pi/7.2,pi/6,pi/5.143,pi/4.5,pi/4,pi/3.6,pi/3.273,pi/3,pi/2.769,pi/2.571,pi/2.4,pi/2.25,pi/2.118,pi/2,pi/1.8,pi/1.636,pi/1.5,pi/1.385,pi/1.286,pi/1.2,pi/1.125,pi/1.059,pi)

    {Angular position of electrode array, rad}

    l_catheter=0.006    {Length of catheter on z axis, m}

    l_lipid=0.0012      {Length of lipid: m}

    d_all=0.006         {Radius of whole region, m}

    d_eccentricity=0.0001 {Eccentricity degree of aorta}

    d_artery=0.004      {Radius of artery, m}

    d_inner=0.0024      {Depth of lipid from endothelium on x axis, m}

    t_lipid=0.0006      {Thickness of lipid, m}

```

$d_{\text{electrode}}=0.000333$	{Separation between the electrodes, m}
$w_{\text{electrode}}=0.0001$	{Width of electrode, m}
$d_{\text{catheter}}=0.0025$	{Diameter of ballooned catheter, m}
$mov=0.0005$	{For the center position of balloon catheter}
$rad_{\text{electrode}}=w_{\text{electrode}}/d_{\text{catheter}}$	
	{Curved electrode attached on the surface of balloon catheter}
$A=w_{\text{electrode}}*w_{\text{electrode}}$	{Surface area of electrode, m <sup>2</sup> }
$I=1e-6$	{Input current, A}
$I_n=I/A$	{Input current density, A/m <sup>2</sup> }
$K_{\text{blood}}=0.68$	{Conductivity of blood, S/m}
$k_{\text{artery}}=0.43$	{Conductivity of artery, S/m}
$K_{\text{lipid}}=0.034$	{Conductivity of lipid, S/m}
$K=K_{\text{blood}}$	{Initial conductivity}
$\epsilon_0=8.854e-12$	{Permittivity of vacuum, F/m}
$\epsilon_{\text{blood}}=3e3*\epsilon_0$	{Permittivity of blood, F/m}
$\epsilon_{\text{artery}}=1e5*\epsilon_0$	{Permittivity of artery, F/m}
$\epsilon_{\text{lipid}}=500*\epsilon_0$	{Permittivity of lipid, F/m}
$\text{Epsilon}=\epsilon_{\text{blood}}$	{Initial permittivity}
	{For 1st lead field}
$E_{1r}=-\text{grad}(V_{1r})$	{Real part of electric fields, V/m}
$E_{1i}=-\text{grad}(V_{1i})$	{Imaginary part of electric fields, V/m}
$J_{1r}=K*E_{1r}-w*\text{Epsilon}*E_{1i}$	{Real part of current density, A/m <sup>2</sup> }
$J_{1i}=w*\text{Epsilon}*E_{1r}+K*E_{1i}$	{Imaginary part of current density, A/m <sup>2</sup> }
$J_{1rm}=\text{magnitude}(J_{1r})$	{Magnitude of real of current density}
$J_{1im}=\text{magnitude}(J_{1i})$	{Magnitude of imaginary of current density}
$J_{1m}=\text{sqrt}((J_{1rm}^2)+(J_{1im}^2))$	{Magnitude of whole current density}
	{For 2nd lead field}

$E2r = -\text{grad}(V2r)$  {Real part of electric fields, V/m}  
 $E2i = -\text{grad}(V2i)$  {Imaginary part of electric fields, V/m}  
 $J2r = K * E2r - w * \text{Epsilon} * E2i$  {Real part of current density, A/m<sup>2</sup>}  
 $J2i = w * \text{Epsilon} * E2r + K * E2i$  {Imaginary part of current density, A/m<sup>2</sup>}  
 $J2rm = \text{magnitude}(J2r)$  {Magnitude of real of current density}  
 $J2im = \text{magnitude}(J2i)$  {Magnitude of imaginary of current density}  
 $J2m = \text{sqrt}((J2rm^2) + (J2im^2))$  {Magnitude of whole current density}  
 {Sensitivity  $S = \text{DOT}((J1r + J1i), (J2r + J2i)) / I^2$ }  
 $Sr = (\text{DOT}(J1r, J2r) - \text{DOT}(J1i, J2i)) / I^2$  {Real part of sensitivity, m<sup>-4</sup>}  
 $Si = (\text{DOT}(J1i, J2r) + \text{DOT}(J1r, J2i)) / I^2$  {Imaginary part of sensitivity}  
 {Impedance  $Z = \text{integral}(S / (K + i * w * \text{Epsilon}))$ ,  $Z / dv = dvZr + i dvZi$ }  
 $dvZr = (K * Sr + w * \text{Epsilon} * Si) / (K^2 + (w * \text{Epsilon})^2)$   
 $dvZi = (K * Si - w * \text{Epsilon} * Sr) / (K^2 + (w * \text{Epsilon})^2)$   
 $Zr = \text{integral}(dvZr)$  {Real part of impedance }  
 $Zi = \text{integral}(dvZi)$  {Imaginary part of impedance}  
 $Zm = \text{sqrt}((Zr^2) + (Zi^2))$  {Impedance magnitude, ohms}  
 $\text{Phase} = \text{arctan}(Zi/Zr) * 180/\pi$  {Phase, degree}

EQUATIONS {Laplace equation with lead field theory}

V1r:  $\text{div}(K * \text{grad}(V1r) - \text{Epsilon} * w * \text{grad}(V1i)) = 0$

V1i:  $\text{div}(K * \text{grad}(V1i) + \text{Epsilon} * w * \text{grad}(V1r)) = 0$

V2r:  $\text{div}(K * \text{grad}(V2r) - \text{Epsilon} * w * \text{grad}(V2i)) = 0$

V2i:  $\text{div}(K * \text{grad}(V2i) + \text{Epsilon} * w * \text{grad}(V2r)) = 0$

EXTRUSION

Surface 'CatheterL'  $Z = -l_{\text{catheter}}$

Layer 'CatheterL' {Bottom of catheter}

Surface 'LipidL'  $Z = -l_{\text{lipid}}$

Layer 'LipidL' {Bottom of lipid}

Surface 'S\_electrodeLbottom'  $Z=-(3*d\_electrode/2 + w\_electrode/2)$   
 Layer 'S\_electrodeL' {Electrode 1 for current input}  
 Surface 'S\_electrodeLtop'  $Z=-(3*d\_electrode/2 - w\_electrode/2)$   
 Layer 'Tissue1'  
 Surface 'M\_electrode1bottom'  $Z=-(d\_electrode/2 + w\_electrode/2)$   
 Layer 'M\_electrode1' {Electrode 1 for voltage measurement}  
 Surface 'M\_electrode1top'  $Z=-(d\_electrode/2 - w\_electrode/2)$   
 Layer 'Tissue2'  
 Surface 'M\_electrode2bottom'  $Z=d\_electrode/2 - w\_electrode/2$   
 Layer 'M\_electrode2' {Electrode 2 for voltage measurement}  
 Surface 'M\_electrode2top'  $Z=d\_electrode/2 + w\_electrode/2$   
 Layer 'Tissue3'  
 Surface 'S\_electrodeRbottom'  $Z=3*d\_electrode/2 - w\_electrode/2$   
 Layer 'S\_electrodeR' {Electrode 2 for current input}  
 Surface 'S\_electrodeRtop'  $Z=3*d\_electrode/2 + w\_electrode/2$   
 Layer 'LipidR' {Top of lipid}  
 Surface 'LipidR'  $Z=l\_lipid$   
 Layer 'CatheterR' {Top of catheter}  
 Surface 'CatheterR'  $Z=l\_catheter$

#### BOUNDARIES

region 'outer' {Outside of artery: blood}  
 start 'outerf' (d\_all,0) arc(center=0,0) angle=360 finish  
 region 'artery' {Region of artery}  
 Layer 'CatheterL'  $K=k\_artery$  Epsilon=eps\_artery  
 Layer 'LipidL'  $K=k\_artery$  Epsilon=eps\_artery  
 Layer 'S\_electrodeL'  $K=k\_artery$  Epsilon=eps\_artery  
 Layer 'Tissue1'  $K=k\_artery$  Epsilon=eps\_artery

```

Layer 'M_electrode1' K=k_artery Epsilon=eps_artery
Layer 'Tissue2' K=k_artery Epsilon=eps_artery
Layer 'M_electrode2' K=k_artery Epsilon=eps_artery
Layer 'Tissue3' K=k_artery Epsilon=eps_artery
Layer 'S_electrodeR' K=k_artery Epsilon=eps_artery
Layer 'LipidR' K=k_artery Epsilon=eps_artery
Layer 'CatheterR' K=k_artery Epsilon=eps_artery

start 'arteryf' (d_artery+d_eccentricity,0) arc(center=0,0) to (0,d_artery)
arc(center=0,0) to (-(d_artery+d_eccentricity),0) arc(center=0,0) to
(0,-d_artery) finish

limited region 'lipid'      {Region of lipid}

Layer 'LipidL' K=k_lipid Epsilon=eps_lipid
Layer 'S_electrodeL' K=k_lipid Epsilon=eps_lipid
Layer 'Tissue1' K=k_lipid Epsilon=eps_lipid
Layer 'M_electrode1' K=k_lipid Epsilon=eps_lipid
Layer 'Tissue2' K=k_lipid Epsilon=eps_lipid
Layer 'M_electrode2' K=k_lipid Epsilon=eps_lipid
Layer 'Tissue3' K=k_lipid Epsilon=eps_lipid
Layer 'S_electrodeR' K=k_lipid Epsilon=eps_lipid
Layer 'LipidR' K=k_lipid Epsilon=eps_lipid

start 'lipidf' ((d_inner+t_lipid/2)*cos(theta*pi/180),-(d_inner+t_lipid/2)*
sin(theta*pi/180)) arc(center=-mov,0) to (d_inner,0) to ((d_inner+t_lipid/2)*
cos(theta*pi/180),(d_inner+t_lipid/2)*sin(theta*pi/180)) to (d_inner+t_lipid,
0) to finish

limited region 'catheter'  {Region of catheter}

Layer 'CatheterL' void

Layer 'LipidL' void

Layer 'S_electrodeL' void

Layer 'Tissue1' void

Layer 'M_electrode1' void

```

Layer 'Tissue2' void

Layer 'M\_electrode2' void

Layer 'Tissue3' void

Layer 'S\_electrodeR' void

Layer 'LipidR' void

Layer 'CatheterR' void

start 'catheterf' (d\_catheter\*cos(eth + rad\_electrode/2) - mov,d\_catheter\*  
sin(eth + rad\_electrode/2)) arc(center=-mov,0) to (-mov,d\_catheter) to  
(-d\_catheter-mov,0) to (-mov,-d\_catheter) to (d\_catheter\*cos(eth -  
rad\_electrode/2) - mov,d\_catheter\*sin(eth - rad\_electrode/2))

Layer 'S\_electrodeL' Natural(V1r)=In Natural(V1i)=0

Layer 'M\_electrode1' Natural(V2r)=In Natural(V2i)=0

Layer 'M\_electrode2' Natural(V2r)=-In Natural(V2i)=0

Layer 'S\_electrodeR' Natural(V1r)=-In Natural(V1i)=0

arc(center=-mov,0) to (d\_catheter\*cos(eth + rad\_electrode/2) -  
mov,d\_catheter\*sin(eth + rad\_electrode/2))

#### PLOTS

{Display of current density on longitudinal section}

contour(J1m) painted on surface Y=tan(eth)\*X zoom(1e-3,-2e-3,4e-3,4e-3)  
log fixed range (0.002,200) as 'log Jm Y=tan(eth)\*X zoom'

{Display of current density on angular section}

contour(J1m) painted on surface Z=0.0 log fixed range (3e-5,2) as 'log Jm  
Z=0'

#### SUMMARY

report(Zm) as 'Zm in all of all region' {Impedance magnitude, ohms}

report(Phase) as 'Phase' {Phase, degree}

END